THE UNIVERSITY *of* EDINBURGH

This thesis has been submitted in fulfilment of the requirements for a postgraduate degree (e.g. PhD, MPhil, DClinPsychol) at the University of Edinburgh. Please note the following terms and conditions of use:

This work is protected by copyright and other intellectual property rights, which are retained by the thesis author, unless otherwise stated.

A copy can be downloaded for personal non-commercial research or study, without prior permission or charge.

This thesis cannot be reproduced or quoted extensively from without first obtaining permission in writing from the author.

The content must not be changed in any way or sold commercially in any format or medium without the formal permission of the author.

When referring to this work, full bibliographic details including the author, title, awarding institution and date of the thesis must be given.

An Advanced Digital Electrical Impedance Tomography System for Biomedical Imaging

Yunjie Yang

A thesis submitted for the degree of Doctor of Philosophy.
The University of Edinburgh.
October 2017

Declaration

I hereby declare that the work presented in this thesis is my own unless otherwise acknowledged. This thesis has not been submitted for any other degree or professional qualification except to The University of Edinburgh for the degree of Doctor of Philosophy.

Yunjie Yang

Date: 17/01/2018

Table of Contents

Acknowledgements

Frist of all, I would like to express my greatest gratitude to my principle supervisor Dr. Jiabin Jia, for his insightful guidance and strong support throughout my PhD research. In the past three and half years, Dr. Jia has been my mentor, friend, and listener, all of these and more. His passion and pursuit for research, as well as his dedication to academic career, have swayed my life deeply. All of my achievements would not have been possible without his patience, assistance and suggestion. His personality and academic charm have made our collaboration during the challenging doctoral period a very pleasant experience.

I also want to thank my assistant supervisor who is also the leader of the Agile Tomography Group, Dr. Nick Polydorides, for all of his valuable suggestion and continuous help on my PhD project. I have found a lot can be learned from his profound knowledge of electrical tomography. Meanwhile, I would like to thank Prof. Hugh McCann for his kind guidance and support in my career and research development.

Additionally, I appreciate current or past colleagues in the Agile Tomography Group a lot for their kind assistance both in academic and daily life. They are Andrea Chighine, Hancong Wu, Yong Bao, Hao Wu, Dimitris Kamilis, Dr. Shengheng Liu, Dr. Alex Tsekenis, Dr. Edward Fisher and Dr. Taweechai Ouypornkochagorn. I have always enjoyed collaborating with the members in the group and benefited a lot from the aspiring academic environment built and maintained by all of these people.

Furthermore, the School of Engineering is gratefully acknowledged for offering my PhD studentship. Meanwhile, the 2015 IEEE I&M Society Graduate Fellowship Award is thanked for supporting part of the research work in this thesis.

Lastly but most importantly, I would like to say thank you to my family. It is difficult to express in word how fortunate I am to have my family together with me in the beautiful city of Edinburgh. It is their selfless love and support that enable me to go through hard times, focus on my research, pursue my dreams, and find my self-worth. Finally…

…to my wife Hui Ai and my son Jason S. Yang…

Lay Summary

Electrical Impedance Tomography (EIT) is an imaging technique to visualise rapidly the conductivity distribution inside a vessel. Compared with other imaging techniques, it has the advantage of fast, non-intrusive, low cost, portable and easy to deploy. Therefore, it has been widely applied in biomedical imaging, such as brain function imaging and lung ventilation imaging, and industrial process imaging, including multi-phase flow imaging and chemical reaction imaging.

This thesis aims to verify the feasibility of EIT in 3D cell culture imaging. Cell culture refers to a bioprocess by which cells are grown under controlled conditions, generally outside of their natural environment. Among common cell culture formats, 3D cell culture is particularly prevailing in tissue engineering, cancer research and pharmaceutical industry. One of the key challenges of 3D cell culture sensing is the lack of non-destructive, real-time and continuous imaging technique to examine the physiological status of the cells. Focusing on this problem, the thesis demonstrates symmetrically a novel methodology to image 3D cell culture systems by using EIT, from the perspectives of system development, high-resolution image reconstruction algorithms, sensor design and experimental validation.

Abstract

Electrical Impedance Tomography (EIT) images the spatial conductivity distribution in an electrode-bounded sensing domain by non-intrusively generating an electric field and measuring the induced boundary voltage. Since its emergence, it has attracted ample interest in the field of biomedical imaging owing to its fast, cost efficient, label-free and non-intrusive sensing ability. Well-investigated biomedical applications of the EIT include lung ventilation monitoring, breast cancer imaging, and brain function imaging. This thesis probes an emerging biomedical application of EIT in three dimensional (3D) cell culture imaging to study non-destructively the biological behaviour of a 3D cell culture system, on which occasion real-time qualitative and quantitative imaging are becoming increasingly desirable. Focused on this topic, the contribution of the thesis can be summarised from the perspectives of biomedical-designed EIT system, fast and effective image reconstruction algorithms, miniature EIT sensors and experimental studies on cell imaging and cell-drug response monitoring, as follows.

First of all, in order to facilitate fast, broadband and real-time 3D conductivity imaging for biomedical applications, the design and evaluation of a novel multi-frequency EIT (mfEIT) system was presented. The system integrated 32 electrode interfaces and its working frequency ranged from 10 kHz to 1 MHz. Novel features of the system included: a) a fully adjustable multi-frequency current source with current monitoring function was designed; b) a flexible switching scheme together with a semi-parallel data acquisition architecture was developed for high-frame-rate data acquisition; c) multi-frequency simultaneous digital quadrature demodulation was accomplished, and d) a 3D imaging software, i.e. *Visual Tomography*, was developed to perform real-time two dimensional (2D) and 3D image reconstruction, visualisation and analysis. The mfEIT system was systematically tested and evaluated on the basis of the Signal to Noise Ratio (SNR), frame rate, and 2D and 3D multi-frequency phantom imaging. The highest SNR achieved by the system was 82.82 dB on a 16-electrode EIT sensor. The frame rate was up to 546 frames per second (fps) at serial mode and 1014 fps at semi-parallel

mode. The evaluation results indicate that the presented mfEIT system is a powerful tool for real-time 2D and 3D biomedical imaging.

The quality of tomographic images is of great significance for performing qualitative or quantitative analysis in biomedical applications. To realise high quality conductivity imaging, two novel image reconstruction algorithms using adaptive group sparsity constraint were proposed. The proposed algorithms considered both the underlying structure of the conductivity distribution and sparsity priors in order to reduce the degree of freedom and pursue solutions with the group sparsity structure. The global characteristic of inclusion boundaries was studied as well by imposing the total variation constraint on the whole image. In addition, two adaptive pixel grouping methods were also presented to extract the structure information without requiring any *a priori* knowledge. The proposed algorithms were evaluated comparatively through numerical simulation and phantom experiments. Compared with the state-of-the-art algorithms such as l_1 regularisation, the proposed algorithms demonstrated superior spatial resolution and preferable noise reduction performance in the reconstructed images. These features were demanded urgently in biomedical imaging.

Further, a planar miniature EIT sensor amenable to the standard 3D cell culture format was designed and a 3D forward model was developed for 3D imaging. A novel 3D-Laplacian and sparsity joint regularisation algorithm was proposed for enhanced 3D image reconstruction. Simulated phantoms with spheres located at different vertical and horizontal positions were imaged for 3D imaging performance evaluation. Image reconstructions of MCF-7 human breast cancer cell spheroids and triangular breast cancer cell pellets were carried out for experimental verification. The results confirmed that robust impedance measurement on the highly conductive cell culture medium was feasible and, greatly improved image quality was obtained by using the proposed regularisation method.

Finally, a series of cancer cell spheroid imaging tests and real-time cell-drug response monitoring experiments by using the developed mfEIT system (Chapter 3), the designed miniature EIT sensors (Chapter 6) and the proposed image

reconstruction algorithms (Chapter 4, 5 and 6) were carried out followed by comparative analysis. The stability of long-term impedance measurement on the highly conductive cell culture medium was verified firstly. Subsequently, by using the proposed algorithms in Chapter 4 and Chapter 5, high quality cancer cell spheroid imaging on a miniature sensor with 2D electrode configuration was achieved. Further, preliminary experiments on real-time monitoring of human breast cancer cell and anti-cancer drug response were performed and analysed. Promising results were obtained from these experiments.

In summary, the work demonstrated in this thesis validated the feasibility of using the developed mfEIT system, the proposed image reconstruction algorithms, as well as the designed miniature EIT sensors to visualise 3D cell culture systems such as cell spheroids or artificial tissues and organs. The established work would expedite the real-time qualitative and quantitative imaging of 3D cell culture systems for the rapid assessment of cellular dynamics.

Publication List

Journal Papers

1. **Yang, Y.** and Jia, J., 2017. An Image Reconstruction Algorithm for Electrical Impedance Tomography Using Adaptive Group Sparsity Constraint. *IEEE Transactions on Instrumentation and Measurement*, *66*(9), pp. 2295-2305.
2. **Yang, Y.**, Wu, H. and Jia, J., 2017. Image Reconstruction for Electrical Impedance Tomography Using Enhanced Adaptive Group Sparsity with Total Variation. *IEEE Sensors Journal*, *17*(17), pp. 5589-5598.
3. **Yang, Y.**, Jia, J., Smith, S., Jamil, N., Gamal, W. and Bagnaninchi, P.O., 2017. A Miniature Electrical impedance Tomography Sensor and 3-D Image Reconstruction for Cell Imaging. *IEEE Sensors Journal*, *17*(2), pp. 514-523.
4. **Yang, Y.** and Jia, J., 2017. A Multi-frequency Electrical Impedance Tomography System for Real-time 2D and 3D Imaging. *Review of Scientific Instruments*, *88*, 085110.
5. **Yang, Y.**, Peng, L., & Jia, J., 2017. A Novel Multi-electrode Sensing Strategy for Electrical Capacitance Tomography with Ultra-low Dynamic Range. *Flow Measurement and Instrumentation*, *53*, pp. 67-79.

Conference Papers

6. **Yang, Y.**, Wu, H. and Jia, J., 2017, October. Simulation Study of Scaffold 3D Cell Culture Imaging Using a Miniature Planar EIT Sensor. *2017 IEEE International Conference on Imaging Systems and Techniques (IST)*, Beijing, China.
7. Yin, X., **Yang, Y.** and Jia, J., 2017, October. 3D Image Reconstruction on a Miniature Planar EIT Sensor Using Sparsity with Median Filter. *IEEE SENSORS 2017*, Glasgow, Scotland, UK.
8. Liu, S., Jia, J. and **Yang, Y.**, 2017, October. Image Reconstruction Algorithm for Electrical Impedance Tomography Based on Block Sparse Bayesian

Learning. *2017 IEEE International Conference on Imaging Systems and Techniques (IST)*, Beijing, China.

9. **Yang, Y.**, Wu, H. and Jia, J., 2017, June. Optimal Design of a Planar Miniature EIT Sensor for 3D Cell Imaging. *18th International Conference on Biomedical Applications of Electrical Impedance Tomography*, Hanover, New Hampshire, USA.
10. **Yang, Y.**, Wu, H. and Jia, J., 2017, June. Total Variation and l_1 Joint Regularisation for High Quality Cell Spheroid Imaging Using EIT. *18th International Conference on Biomedical Applications of Electrical Impedance Tomography*, Hanover, New Hampshire, USA.
11. **Yang, Y.** and Jia, J., 2016, October. Image Reconstruction Algorithm for Electrical Impedance Tomography Using Group Sparsity. *8th World Congress on Process Tomography*, Iguassu Falls, Brazil.
12. **Yang, Y.**, Jia, J., Polydorides, N. and McCann, H., 2014, October. Effect of Structured Packing on EIT Image Reconstruction. *2014 IEEE International Conference on Imaging Systems and Techniques (IST),* pp. 53-58, Santorini, Greece.

Abbreviations

2D, 3D	2 Dimensional, 3 Dimensional
3D-TV	3 Dimensional Total Variation
3D-Lap-l_1	3D-Laplacian and Sparsity Joint Regularisation
A, mA, μA, nA	Ampere, milli-Ampere, micro-Ampere, nano-Ampere
A-ADMM	Accelerated Alternating Direction Method of Multipliers
AC	Alternating Current
ADC	Analogue-to-Digital Converter
ADMM	Alternating Direction Method of Multipliers
AGS	Adaptive Group Sparsity Constrained Algorithm
AMFCS	Adjustable Multi-frequency Current Source
ANNs	Artificial Neural Networks
BEM	Boundary Element Method
CC	Correlation Coefficient
CEM	Complete Electrode Model
CV	Coefficient of Variation
DAC	Digital-to-Analog Converter
dB	Decibel
DC	Direct Current
DDS	Direct Digital Synthesis
DSP	Digital Signal Processor
DC	Direct Current
EAGS-TV	Enhanced Adaptive Group Sparsity with Total Variation
EIDORS	Electrical Impedance and Diffuse Optical Tomography

	Reconstruction Software
EIS	Electrical Impedance Spectroscopy
EIT	Electrical Impedance Tomography
FD	Frequency Difference
FEM	Finite Element Method
FPGA	Field Programmable Gate Array
FPS	Frames Per Second
IE	Image Error
I/O	Input to Output
IP	Intellectual Property
LDO	Low-Dropout
LPF	Low Pass Filter
MAC	Multiply-Accumulator
mfEIT	Multi-frequency Electrical Impedance Tomography
NCO	Numerically Controlled Oscillator
PBS	Phosphate Buffer Solution
PGA	Programmable Gain Amplifier
SNR	Signal to Noise Ratio
TD	Time Difference
TV	Total Variation
TwIST	Two-step Iterative Shrinkage/Thresholding Algorithm
UART	Universal Asynchronous Receiver/Transmitter
USB	Universal Serial Bus
VCCS	Voltage Controlled Current Source

Chapter 1 Introduction

1.1 Background and Motivation

Emerging in the early 1980's (Barber and Brown, 1984), Electrical Impedance Tomography (EIT) is one of the electrical tomographic imaging modalities to visualise non-intrusively the absolute value or variation of electrical conductivity within a region of interest (Lionheart, 2004, Wang et al., 2005, Bayford, 2006, Aristovich et al., 2016). The basic working principle of EIT is to apply successively an electrical current on the selected electrodes and measure the induced voltages on the other electrode pairs. Current excitation and voltage acquisition are repeated continuously and rapidly until all the non-redundant electrode combinations are deployed. A completed set of data can then produce one frame of a sliced 2D or a 3D image based on certain *a priori* knowledge to estimate the spatial distribution of conductivity.

Attributing to the high-speed, non-radiation, and non-intrusive sensing ability of EIT, in recent years it has been exploited extensively in industrial process imaging, in order to either estimate key process parameters or capture fast-change phenomena. Relevant cases include the use of EIT for real-time multiphase flow characterisation (Heikkinen et al., 2006, Wang et al., 2016), sedimentation monitoring (Tossavainen et al., 2007), liquid mixing dynamics investigation (Carletti et al., 2016), spatial damage in concrete imaging (Hallaji et al., 2014), and pressure-sensitive artificial skin of robotics (Silvera-Tawil et al., 2015). In addition to its high maturity practice in industrial process measurement, EIT has also gained a great deal of interest in biomedical or biological process imaging, which is targeted at monitoring and assessing biological dynamics for the study of biological behaviour or control of the chemical environment of the bioprocess. Reported research on biomedical or biological process imaging based on EIT includes brain function imaging (Yerworth et al., 2003, Bagshaw et al., 2003, Aristovich et al., 2016), breast cancer imaging (Halter et al., 2008, Murphy et al., 2017), lung ventilation imaging (Frerichs, 2000, Luepschen et al., 2007, Vogt et al., 2012), cell sedimentation

imaging in a microchannel (Yao et al., 2016), and cell culture imaging (Yang et al., 2017a).

Although the evolvement of EIT to date are inspiring, the following challenges still exist before its practical applications can be achieved particularly in biomedical scenarios: a) compared with other tomography modalities, e.g. Computed Tomography (CT), the application scope of EIT has been promoted by its high temporal resolution, e.g. ~1000 frames per second (Wang et al., 2005), but limited by its relatively low spatial resolution, e.g. ~10% of the sensor diameter (Metherall et al., 1996); b) in order to maximise sensing performance and conform to the medical instrument standard, a higher level of hardware and software development are desired; c) furthermore, to produce informative tomographic images in real time, high resolution, fast image reconstruction algorithms are demanded; d) moreover, aiming at specific applications, it is imperative to investigate optimised sensor structures and electrode configurations so as to enhance significantly the spatial sensing ability and lastly, (e) intensive experimental examination and cross validation of EIT's feasibility in biomedical scenarios remains a gap.

This thesis mainly focuses on exploiting the EIT technique for biomedical applications, in particular the imaging of 3D cell culture systems, from the perspectives of instrumentation, image reconstruction algorithms, biosensor design and experimental analysis. Cell culture, particularly 3D cell culture, is indispensable for various biological applications, such as tissue engineering, pharmaceutical industry and cancer research (Ravi et al., 2015). Compared with conventional 2D cell culture (Breslin and O'Driscoll, 2013), which cultivates monolayer cells on flat and rigid substrates, cell culture using a 3D model facilitates the behaviour which is closer to the real complex *in vivo* conditions as well as the delivery of research outcomes to *in vivo* applications (Vinci et al., 2012). The typical formats of 2D and 3D cell culture systems are comparatively illustrated in Figure 1-1.

In various 3D cell culturing processes, non-intrusive online sensing technique with high temporal resolution is desperately desirable for the study of biological behaviour and long-term monitoring of fast cellular dynamics, such as cell-drug

response, bone tissue regeneration, etc. However, few techniques possessing such capabilities have been comprehensively investigated and maturely applied. To bridge this gap, the thesis aims to demonstrate proof-of-principle that EIT is well suited for multicellular spheroids imaging, which represents a non-destructive cell viability assay based on membrane integrity. Taken together with EIT spatial resolution, the innovative approaches developed in the thesis will enable non-destructive, real-time monitoring of the cellular dynamics within a 3D cell culture system, e.g. cell-drug response across all layers of cell spheroids. This is deemed a critical challenge and cannot be realised by other imaging modalities to the date.

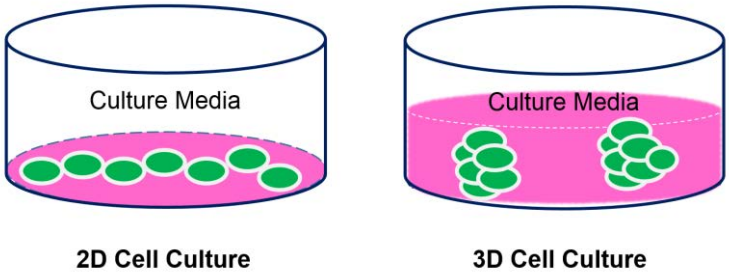

Figure 1-1 Schematic illustration of typical 2D and 3D cell culture formats.

1.2 Aims and Objectives

Aiming at exploring EIT in biomedical applications, with particular emphasis on 3D cell culture imaging, the primary target of this thesis is to develop a digital technique based, fast, flexibly configurable, multi-frequency EIT (mfEIT) platform and further, improve the spatial resolution of reconstructed images while maintaining their temporal resolution by proposing innovative 2D and 3D image reconstruction algorithms. Thereafter, the advanced mfEIT system together with the proposed image reconstruction algorithms will be employed for 3D cell culture imaging and real-time cell-drug response monitoring. To accomplish these targets, the following objectives are established:

1) Advanced EIT platform implementation, with configurable electrodes, controllable stimulus patterns, high SNR (> 70dB) and fast frame rate

(up to 1000 fps) to capture cellular dynamics at multiple frequencies in real time, stably and accurately; in addition, the development of adjunctive user interface integrated with real-time 2D/3D imaging and data/image analysis functions.

2) Novel 2D/3D image reconstruction algorithms investigation based on either mono-frequency or multi-frequency measured data for effective reconstruction of weak and small dimension conductivity variations, which are the primary reconstruction objectives encountered in 3D cell culture systems.

3) Numerical and experimental study of innovative biosensors that are compatible with the 3D cell culture system, from the perspectives of sensor structure, electrode placement, forward modelling and image reconstruction.

4) Experimental evaluation of the developed mfEIT platform, biosensors and image reconstruction algorithms on 3D cultivated cell spheroids, making connection between signal/image and cellular dynamics obtained from established theory or other sensing modalities.

1.3 Main Contribution

The main contributions of this thesis are summarised as follows:

1) A biomedical-designed mfEIT system with broad bandwidth (10 kHz to 1 MHz), high temporal resolution (up to 1014 fps), high SNR (82.82 dB) and real-time 2D/3D impedance spectroscopic imaging capabilities, was designed, developed from scratch, and thoroughly evaluated via phantom experiments.

2) Two novel image reconstruction algorithms based on adaptive group sparsity and TV constraints were proposed to generate tomographic images with superior image quality, lower computational cost and

significantly improved spatial resolution. The algorithms were verified to be effective for reconstructing in particular weak and small dimension conductivity variations through phantom and cell imaging experiments.

3) A planar miniature EIT sensor amenable to the standard 3D cell culture format was designed and, the characterisation and 3D image reconstruction of the sensor were studied based on 3D modelling and a 3D Laplacian and l_1 joint regularisation algorithm. The sensor's performance was assessed by conducting MCF-7 breast cancer cell pellet imaging experiments.

4) Extensive experimental studies including the visualisation of MCF-7 breast cancer cell spheroids/pellets and real-time cell-drug response monitoring, by utilising the developed mfEIT platform, the proposed image reconstruction algorithms and the designed miniature EIT sensors, were performed. The results verified the feasibility of applying EIT in imaging cell spheroids and cellular dynamics within 3D cell culture systems.

All of these works have made a step progress in promoting EIT as an effective real-time imaging modality for 3D cell culture systems and have been published in or submitted to renowned journals and international conferences as indicated in the publication list.

1.4 Overview of the Thesis

The thesis is composed of eight chapters and the remaining part is structured as follows. Following the introductory part in this chapter, Chapter 2 provides a brief review of the fundamental theory of EIT, the existing EIT systems for biomedical imaging, the state-of-the-art EIT image reconstruction algorithms, and the emerging applications of EIT in cellular Imaging.

Chapter 3 presents the design and evaluation of a configurable, fast mfEIT system for real-time 2D and 3D biomedical and bioprocess imaging. The novel features of the mfEIT system are demonstrated and the evaluation results suggest that the presented mfEIT system is a powerful tool for real-time 2D and 3D spectral impedance imaging.

Chapter 4 proposes a novel image reconstruction algorithm for EIT using adaptive group sparsity constraint to obtain enhanced image quality. The proposed algorithm takes into account the underlying structure characteristics and sparsity prior of the conductivity distribution. Simulation and experiment results validate the superior noise reduction performance and improved spatial resolution of the proposed algorithm, which lays a solid foundation for high quality cell culture imaging.

Chapter 5 develops another image reconstruction algorithm for EIT using enhanced adaptive group sparsity with TV constraint. This algorithm simultaneously utilises the *a priori* knowledge of regional structure feature, and the global characteristic of the conductivity distribution. Superior spatial resolution and noise reduction performance have been obtained in both simulation and experiments. Combining the TV constraint, distinct boundary of inclusions has been promoted.

Chapter 6 investigates the feasibility of static imaging of 3D cell culture systems via the miniature EIT sensor. A planar miniature EIT sensor amenable to standard cell culture format is designed and a 3D forward model for the sensor is developed for 3D imaging. Furthermore, a novel 3D-Laplacian and sparsity joint regularisation algorithm is proposed for enhanced 3D image reconstruction.

Chapter 7 provides a series of experimental studies of 3D cell culture imaging and cell-drug response monitoring based on the developed techniques presented in the former chapters. Promising experiment results have been obtained, which justify the feasibility and potential of applying EIT in real-time, continuous 3D cell culture imaging.

Finally, Chapter 8 summarises the scientific contribution of this thesis and discusses the potential work in the future with emphasis on the further advancement of cellular dynamics imaging and long-term cell culture monitoring on the basis of the developed mfEIT system and image reconstruction algorithms.

Chapter 2 Review of Electrical Impedance Tomography

2.1 Introduction

Following the background introduction, this chapter reviews succinctly the foundation of EIT, including the principle of mono-frequency and multi-frequency EIT. On that basis, the state-of-the-art biomedical EIT systems are comprehensively discussed and their specifications are thoroughly compared. Furthermore, recent advances of EIT image reconstruction algorithms are briefly summarised. Finally, EIT's emerging application in cell imaging, which is one of the kernel contents of this thesis, are reviewed.

2.2 Foundation of EIT

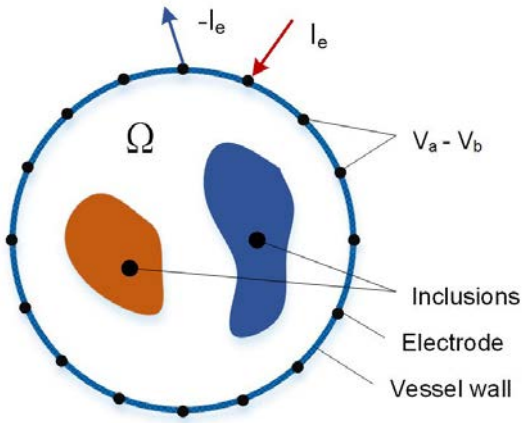

Figure 2-1 Schematic illustration of EIT's sensing principle.

As illustrated in Figure 2-1, given a bounded, simple connected domain Ω and its boundary ∂Ω, the objective of EIT is to estimate the conductivity (variation) distribution inside Ω by successively injecting a pair of complementary alternating current, i.e. $[I_e, -I_e]$, into selected boundary electrodes and measuring the induced voltage, i.e. $[V_a, V_b]$, across another electrode pairs on the boundary ∂Ω. The electromagnetic field inside Ω, induced by the injected current, is governed by Maxwell's equations. By assuming low frequencies and small field strengths, an approximated conductivity equation can be obtained (Bayford, 2006), i.e.

$$\nabla \cdot (\sigma(x,y)\nabla u(x,y)) = 0, \quad (x,y) \in \Omega \tag{2.1}$$

where σ denotes the conductivity inside Ω, and u is the electric potential inside Ω.

The Neumann boundary condition, i.e. the injected currents, and the Dirichlet boundary condition, i.e. the voltages on the boundary $\partial\Omega$, based on the Complete Electrode Model (CEM) (Vauhkonen et al., 1999, Cheng et al., 1989) are commonly applied associated with (2.1), in order to deliver a unique solution. CEM is the most accurate electrode model for EIT, which can be realised physically. In addition to (2.1), the other equations of CEM are given by:

$$u + z_l \sigma \frac{\partial u}{\partial n} = U_l \qquad \text{(on the electrode } e_l, \, l = 1, 2, \ldots, L) \tag{2.2a}$$

$$\int_{e_l} \sigma \frac{\partial u}{\partial n} dS = I_l \qquad \text{(on the electrode } e_l, \, l = 1, 2, \ldots, L) \tag{2.2b}$$

$$\sigma \frac{\partial u}{\partial n} = 0 \qquad \text{(between electrodes)} \tag{2.2c}$$

where L is the total number of electrodes and e_l denotes the l^{th} electrode. z_l denotes the contact impedance of the l^{th} electrode; n is the outward unit norm of $\partial\Omega$; U_l and I_l represent respectively the electrical potential and injected current on the l^{th} electrode.

The existence and uniqueness of the solution u are further ensured by the conservation of charges imposed by (2.3a) and the choice of ground voltage in order to have (2.3b) (Somersalo et al., 1992).

$$\sum_{l=1}^{L} I_l = 0 \tag{2.3a}$$

$$\sum_{l=1}^{L} U_l = 0 \tag{2.3b}$$

The relation between the conductivity inside Ω and the boundary voltages on electrodes can be further described by the nonlinear deterministic observation model as:

$$\mathbf{V}=\mathrm{F}(\boldsymbol{\sigma})+\mathbf{e} \tag{2.4}$$

where **V** is the measured electrode potentials; F represents the nonlinear forward operator and **e** denotes the additive noise and measurement error. In the context of difference EIT imaging, (2.4) can be linearized condition on a small conductivity perturbation $\Delta\boldsymbol{\sigma}$, and the resulting analytical relation between $\Delta\boldsymbol{\sigma}$ and the change of boundary voltage $\Delta\mathbf{V}$ can be stated as:

$$\Delta\mathbf{V} \approx \mathbf{J}\Delta\boldsymbol{\sigma} \tag{2.5}$$

where **J** is the Jacobian matrix (or denoted as sensitivity matrix) calculated by:

$$\mathbf{J}_{cm}(x,y)=\frac{\partial V_{cm}}{\partial \sigma_k}=-\int_{\text{pixel } k}\nabla\mathbf{u}\left(I^c\right)\cdot\nabla\mathbf{u}\left(I^m\right)dV \tag{2.6}$$

where $\mathbf{J}_{cm}(x, y)$ is the sensitivity value at pixel (x, y) when electrode pairs c and m are selected as current injection and measurement electrodes respectively; $\mathbf{u}(I^c)$ and $\mathbf{u}(I^m)$ denote the electrical potential distribution in Ω when the c^{th} and m^{th} electrode pairs are selected as current injection electrodes, respectively.

In consideration of real-time performance, the linearized model depicted in (2.5) is employed for image reconstruction in this thesis. Regarding difference EIT imaging, one commonly applied method is the mono-frequency time-difference (TD) imaging. Here a pair of complementary currents with a single frequency component are injected into the sensing domain. A measurement at time point t_0 is first performed as a reference point, then the voltage difference at time point t_1 with respect to the reference is employed for image reconstruction, which is stated as:

$$\Delta\mathbf{V}_{\text{TD}}=\mathbf{V}_{t_1}-\mathbf{V}_{t_0} \tag{2.7}$$

Alternatively, a more attractive method in biomedical applications is the frequency-difference (FD) imaging, in which case a pair of complementary currents composed of two (or multiple) different frequency components, i.e., f_0 and f_1, are injected into the sensing domain. The voltage difference between the two frequency components is then acquired for image reconstruction. This is expressed as:

$$\Delta \mathbf{V}_{\mathrm{FD}} = \mathbf{V}_{f_1} - \mathbf{V}_{f_0} \tag{2.8}$$

As the bioimpedance of tissue varies with respect to the frequency of injected current, using multi-frequency current excitation can present more information in both time and frequency domains. In addition, under many circumstances image reconstruction based on frequency difference data is more feasible than using time difference data. It is particularly the case as in practical situations, it is difficult to obtain a proper baseline $\mathbf{V}_{t_0}$ in advance in time difference imaging.

After acquiring the voltage difference vector according to (2.7) or (2.8), the procedure of EIT image reconstruction is to estimate the conductivity based on the voltage difference vector, the Jacobian matrix and *a priori* knowledge. This constitutes a typical inverse problem. A succinct review of the state-of-the-art image reconstruction algorithms will be presented in Section 2.4.

2.3 EIT System

2.3.1 System Architecture and Function

An EIT system implements the sensing principle demonstrated in the last section. Figure 2-2 illustrates the simplified block diagram of a typical EIT system. A completed EIT system is generally composed of three sub-systems, i.e., an EIT sensor containing an electrode array as shown on the left of the figure, the EIT instrumentation and measurement hardware made up of current excitation and data acquisition units as presented in the middle, and an EIT imaging software as illustrated on the right. The EIT sensor makes direct contact with an electrolyte. It has been investigated intensively with the objective to provide maximum sensitivity, small dynamic range of measurement and low contact impedance, especially for

complicated 3D sensor structures. The EIT measurement hardware performs control and multiplexing of current injection, signal conditioning, signal conversion, demodulation and data transmission. It is thus a core prerequisite design task in this work. The EIT imaging software installed on peripheral equipment, e.g. PC or smart phone, realises the flexible control of the EIT hardware, image reconstruction, visualisation and data analysis functions. In this thesis, the novel development of each of these sub-systems will be demonstrated in Chapter 3.

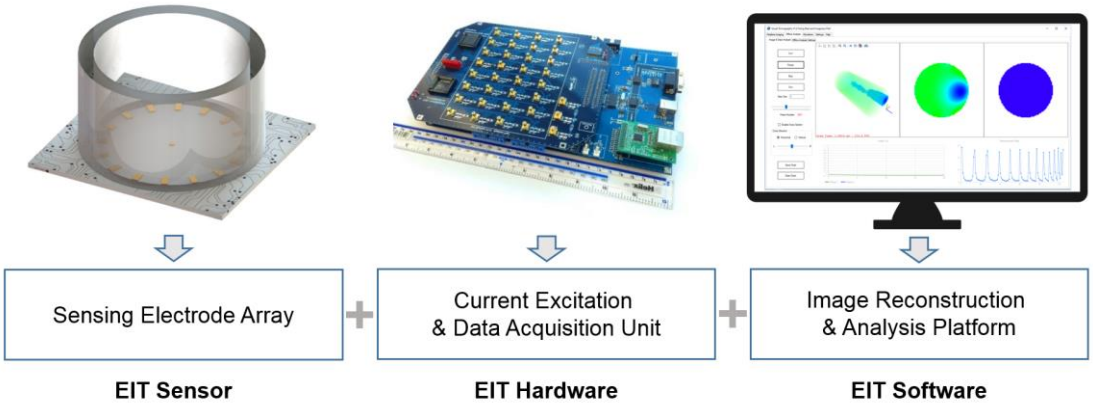

Figure 2-2 Simplified block diagram of a typical EIT system.

2.3.2 Existing EIT Systems for Biomedical Imaging

In the past decades, EIT has been continuously gaining interest in biomedical research and applications such as breast imaging (Saulnier et al., 2007) and brain function imaging (Aristovich et al., 2016). Biomedical application of EIT places substantial requirements on EIT instrumentation. The signal bandwidth, imaging temporal resolution, accuracy, stability and safety of the EIT system play a pivotal role in both 1) acquiring high quality imaging performance and 2) conducting robust quantitative analysis.

The first EIT system designed for biomedical research and diagnostic imaging is the Sheffield Mk1 (Barber and Brown, 1984). Since then, substantial efforts have been made by research groups in the field to further improve EIT systems towards the target of its practical application in the biomedical sciences.

Among them, remarkable work includes the Sheffield EIT systems such as Sheffield Mk3a (Brown and Seagar, 1987, Brown et al., 1994) and Mk3.5 (Wilson et al., 2001) EIT systems, the Oxford Brookes University EIT systems including OXBACT-3 (Zhu et al., 1994) and OXBACT-5 (Yue and McLeod, 2008), the UCL EIT systems such as UCLH Mk 1b (Yerworth et al., 2002) and UCLH Mk 2.5 (McEwan et al., 2006), the KHU EIT systems such as KHU Mark1 (Oh et al., 2007) and its successor KHU Mark2 (Oh et al., 2011) and KHU Mark2.5 (Wi et al., 2014), the Rensselaer's ACT 4 EIT system (Saulnier et al., 2007), the Dartmouth EIT system (Halter et al., 2008), and the Manchester fEITER system (Davidson et al., 2010).

Table 2-1 provides a comprehensive comparison of the abovementioned EIT systems in terms of targeted applications, number of channels, current frequency range, frame rate, signal processing technique, SNR, sensing protocol, data link and real-time imaging ability. As demonstrated in the Table, the primary applications of these biomedical EIT systems can be divided into three categories: 1) lung ventilation imaging, which is regarded as the most successful biomedical application thus far, by using the Sheffield systems; 2) breast imaging, for the purpose of cancer detection, by using the OXBACT systems, the ACT system, the KHU systems and the Dartmouth systems; and 3) brain function imaging, which is also the most challenging and complicated application due to the difficulties of cross validation, by using the UCLH systems, the KHU systems and the fEITER system.

In terms of system specifications, most of the recent designs were constructed based on the digital techniques, i.e. digital signal processing based on Field Programmable Gate Array (FPGA) or Digital Signal Processor (DSP), which reduced the complexity of the hardware while increasing its flexibility and reliability. The most common number of channels was designed as 32 or 64, which was suitable for majority of applications. The excitation current frequency ranged from 10 Hz up to 12.5 MHz. The maximum frame rate of these systems was 100 fps achieved by the fEITER, KHU Mark2 and KHU Mark2.5 systems. The SNR of the most recent systems since 2007 was higher than 80 dB. Moreover, the KHU systems and ACT 4 system also came with an imaging software with real-time 2D image reconstruction ability whilst the others were not reported.

Table 2-1 Performance comparison of some recent EIT systems for biomedical imaging.

EIT System	Date	Institute	Target	Channels	Current Frequency	Technology	Frame Rate	SNR	Sensing Protocol	Data Link	Real-time Imaging Software
Sheffield Mk3a	1994	Royal Hallamshire Hospital	Regional ventilation monitoring	16	9.6 kHz – 1.2 MHz	Analogue	33 fps	25 dB	Interleaved drive/receive	NA	No
Sheffield Mk3.5	2001			8	2 kHz – 1.6 MHz	Digital (DSP)	25 fps	40 dB	Adjacent drive/receive	Isolated RS485	No
OXBACT-3	1994	Oxford Brookes University	Thoracic imaging	32	10 kHz – 160 kHz	Digital (DSP)	25 fps	NA	NA	Fibre Optic	No
OXBACT-5	2008			32	26 kHz – 56 kHz	Digital (FPGA)	25 fps	NA	NA	Wireless LAN	No
UCLH Mk 1b	2002	University College London	Brain function imaging	64	225 Hz – 77 kHz	NA	3 fps	50 dB	Flexible	RS232	No
UCLH Mk 2.5	2006			64	20 Hz – 1 MHz	NA	0.12 fps	40 dB	Flexible	Isolated USB	No
KHU Mark1	2007	Kyung Hee University	Brain function imaging	16/32	10 Hz – 500 kHz	Digital (DSP)	1 fps	100 dB	Adjacent receive	Isolated USB	2D
KHU Mark2	2011		Brain, breast imaging	8 – 64	10 Hz – 500 kHz	Digital (DSP+FPGA)	100 fps	84 dB	Flexible	Isolated USB	2D
KHU Mark2.5	2014			64	10 Hz – 500 kHz	Digital (DSP+FPGA)	100 fps	80 dB	Flexible	Isolated USB	2D
ACT 4	2007	Rensselaer Polytechnic Institute	Breast cancer detection	72	3.33 kHz – 1 MHz	Digital (FPGA)	2.6 fps	90 dB	NA	PCI	2D
Dartmouth	2008	Dartmouth College	Breast imaging	64	10 kHz – 12.5 MHz	Digital (DSP+FPGA)	30 fps	94 dB	Flexible	RS232	No
fEITER	2010	University of Manchester	Brain function imaging	32	10 kHz	Digital (FPGA)	100 fps	80 dB	Adjacent receive	USB	No

Judging from the evolution of biomedical EIT systems, there is an explicit trend to incorporate the features of broad current frequency range, high frame rate, high SNR, digital signal processing technique, flexible sensing protocol and real-time imaging ability, in order to fulfil the complicated requirements of biomedical imaging. Meanwhile, proper circuit design and isolation according to medical instrument design standards are also becoming a matter of concern, especially for human medical diagnostic instrumentation.

2.4 The State-of-the-art EIT Image Reconstruction Algorithms

Aside from the focus of advanced instrumentation, exploitation of image reconstruction algorithms generating high quality tomographic images has also been deemed a critical challenge. The image reconstruction of EIT is a typical inverse, ill-conditioned and ill-posed problem. In recent years, extensive investigation on EIT image reconstruction problems have been reported with respect to the improvement of image quality. Some of the most popular EIT image reconstruction algorithms have been well summarised in recent literature reviews (Yang and Peng, 2003, Lionheart, 2004, Bayford, 2006). Below, a brief review of the state-of-the-art EIT image reconstruction algorithms is provided. This is taken from the perspectives of common regularisation techniques, direct reconstruction methods, statistical framework based reconstruction methods, and other emerging methods. A widely used open-source Matlab toolkit for EIT image reconstruction is also introduced.

2.4.1 Regularisation based Methods

The predominant way of solving the ill-posed EIT image reconstruction problem is to use the regularisation technique (Bertero and Boccacci, 1998, Peng et al., 2000). This technique identifies and incorporates *a priori* knowledge of the conductivity as additional constraints in hope of achieving an approximated solution with smaller image error and better spatial resolution. Based on the approximated linearized EIT model depicted in (2.5), the conductivity variation $\Delta\boldsymbol{\sigma}$ can be

estimated by solving the constrained optimisation problem stated by (2.9) or the equivalent unconstrained optimisation problem stated by (2.10), as follows:

$$\begin{cases} \min\limits_{\Delta\boldsymbol{\sigma}} & \mathrm{R}(\Delta\boldsymbol{\sigma}) \\ s.t. & \mathbf{J}\Delta\boldsymbol{\sigma}=\Delta\mathbf{V} \end{cases} \tag{2.9}$$

$$\Delta\boldsymbol{\sigma}_{reg} = \arg\min_{\Delta\boldsymbol{\sigma}} \left\{ \frac{1}{2}\left\|\mathbf{J}\Delta\boldsymbol{\sigma}-\Delta\mathbf{V}\right\|_2^2 + \lambda \mathrm{R}(\Delta\boldsymbol{\sigma}) \right\} \tag{2.10}$$

where R is the regularisation function incorporating *a priori* knowledge; λ is the regularisation parameter.

Typical choices of the regularisation function R include quadratic penalties, i.e. the l_2 norm, for the promotion of smoothness and, monadic penalties, i.e. the l_1 norm, for the tendency of sparsity or discontinuity in the selected domain. Using the first case as an example, this can be solved exactly through a single step calculation, which includes the well-known Tikhonov regularisation (Vauhkonen et al., 1998), where

$$\mathrm{R}(\Delta\boldsymbol{\sigma})=\left\|\Delta\boldsymbol{\sigma}\right\|_2^2 \tag{2.11}$$

which can be explicitly calculated as:

$$\Delta\boldsymbol{\sigma}_{reg} = \left(\mathbf{J}^{\mathrm{T}}\mathbf{J}+\lambda\mathbf{I}\right)^{-1}\mathbf{J}^{\mathrm{T}}\Delta\mathbf{V} \tag{2.12}$$

where **I** denotes the identity matrix.

Another quadratic penalty form widely employed is Laplacian regularisation (Yang et al., 2014), where

$$\mathrm{R}(\Delta\boldsymbol{\sigma})=\left\|\mathbf{L}\Delta\boldsymbol{\sigma}\right\|_2^2 \tag{2.13}$$

which can be explicitly calculated as:

$$\Delta\boldsymbol{\sigma}_{reg} = \left(\mathbf{J}^{\mathrm{T}}\mathbf{J} + \lambda\mathbf{L}^{\mathrm{T}}\mathbf{L}\right)^{-1}\mathbf{J}^{\mathrm{T}}\Delta\mathbf{V} \tag{2.14}$$

where **L** represents the four-connected region second-order Laplacian operator matrix (Yang et al., 2014). An intuitive illustration of the Laplacian operator exerted on a certain pixel is shown in Figure 2-3.

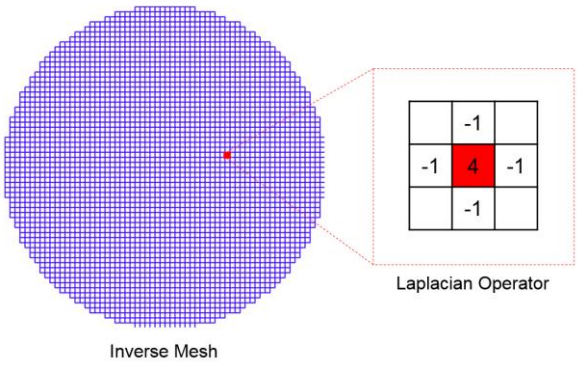

Figure 2-3 Schematic illustration of the Laplacian operator on a pixel.

Another typical regularisation method in EIT utilises the NOSER type prior (Cheney et al., 1990), which is formulated as:

$$\Delta\boldsymbol{\sigma}_{reg} = \left(\mathbf{J}^{\mathrm{T}}\mathbf{J} + \lambda\mathbf{R}_{\mathbf{NR}}\right)^{-1}\mathbf{J}^{\mathrm{T}}\Delta\mathbf{V} \tag{2.15}$$

where $\mathbf{R_{NR}}$ is a diagonal matrix and each diagonal element $[\mathbf{R_{NR}}]_{i,i} = [\mathbf{J}^{\mathrm{T}}\mathbf{J}]_{i,i}^{\,p}$. The determination of exponent p is a heuristic compromise between enforcing noise to the boundary (if $p = 0$) or to the centre (if $p = 1$) (Adler et al., 2007).

The three one-step methods are advantageous in terms of computation cost thus are employed popularly for real-time conductivity imaging and, also, qualitative evaluation due to their relatively low image quality in comparison with the iterative algorithms that will be discussed below. In addition, the one-step methods can also be applied to provide an initial guess for the iterative algorithms or offer *a priori* knowledge of the conductivity distribution.

Examples of the second case, which make use of monadic penalties, are usually solved iteratively, such as the prevailing l_1 regularisation (or sparsity regularisation) (Jin et al., 2012) and TV regularisation (Osher et al., 2005). Sparsity constraints have been investigated thoroughly in the field of signal and image processing, and promising results have been demonstrated when the signal is sparse, that is, most of the elements are zero, in the spatial or frequency domains, or under a certain basis (Baraniuk, 2007, Grasmair et al., 2008). Under some circumstances, conductivity distributions inside the sensing domain are naturally sparse, or, sparse under a certain basis. This feature can be utilised as *a priori* knowledge to promote nonzero coefficients and suppress the noise close to zeroes in the estimated results. Recently, l_1 regularisation has been investigated extensively within the field of EIT (Jin et al., 2012, Ye et al., 2015, Gehre et al., 2012). This method can be stated by a general format as:

$$\Delta\boldsymbol{\sigma}_{reg} = \arg\min_{\Delta\boldsymbol{\sigma}} \left\{ \frac{1}{2} \left\| \mathbf{J}\Delta\boldsymbol{\sigma} - \Delta\mathbf{V} \right\|_2^2 + \lambda \left\| \boldsymbol{\Phi}^{\mathrm{T}} \Delta\boldsymbol{\sigma} \right\|_1 \right\} \tag{2.16}$$

where $\Delta\boldsymbol{\sigma}=\boldsymbol{\Phi}\mathbf{a}$ and $\mathbf{a}=\boldsymbol{\Phi}^{-1}\Delta\boldsymbol{\sigma}=\boldsymbol{\Phi}^{\mathrm{T}}\Delta\boldsymbol{\sigma}$, given $\boldsymbol{\Phi}$ is an orthogonal matrix; $\mathbf{a}$ is the sparse coefficient vector of the conductivity distribution under a certain basis $\boldsymbol{\Phi}$, for instance, a wavelet basis (Anselmi et al., 2015) or a learned dictionary (Wang et al., 2015). Specifically, if $\boldsymbol{\Phi}$ is equal to the identity matrix, it indicates the conductivity distribution is naturally sparse and, in this case, $\Delta\boldsymbol{\sigma}=\mathbf{a}$. The l_1 norm of the coefficient vector, i.e. $\|\mathbf{a}\|_1$, is then minimised for sparse recovery. The l_1 regularisation facilitates the recovery of a high dimensional signal with a much smaller number of measurements. Equation (2.16) can be solved efficiently based on a number of well-investigated methods, such as the basis pursuit methods (van den Berg and Friedlander, 2008), etc.

TV regularisation is another widely studied regularisation method for EIT image reconstruction (Wang et al., 2007, Zhou et al., 2015, Gonzalez et al., 2017, Gonzalez et al., 2016). It is particularly effective for estimating the conductivity variation distribution with a sharp boundary. This method can be formulated as:

$$\Delta\boldsymbol{\sigma}_{reg} = \arg\min_{\Delta\boldsymbol{\sigma}} \left\{ \frac{1}{2} \left\| \mathbf{J}\Delta\boldsymbol{\sigma} - \Delta\mathbf{V} \right\|_2^2 + \lambda \left\| \Delta\boldsymbol{\sigma} \right\|_{\mathrm{TV}} \right\} \tag{2.17}$$

where $\|\Delta\boldsymbol{\sigma}\|_{\mathrm{TV}}$ is the TV norm of the conductivity variation distribution. It is equivalent to the l_1 norm of the gradient of the conductivity variation distribution, as defined by:

$$\begin{aligned} \left\| \Delta\boldsymbol{\sigma} \right\|_{\mathrm{TV}} &= \sum_{x,y} \sqrt{(\mathrm{D}_{x,y}^{v}(\Delta\boldsymbol{\sigma}))^2 + (\mathrm{D}_{x,y}^{h}(\Delta\boldsymbol{\sigma}))^2} \\ &= \sum_{x,y} \left| \nabla_{x,y} (\Delta\boldsymbol{\sigma}) \right| \\ &= \left\| \nabla (\Delta\boldsymbol{\sigma}) \right\|_1 \end{aligned} \tag{2.18}$$

where (x, y) denotes the coordinate of a pixel inside Ω. $\mathrm{D}_{x,y}^{v}(\Delta\boldsymbol{\sigma})$ and $\mathrm{D}_{x,y}^{h}(\Delta\boldsymbol{\sigma})$ are the derivatives of $\Delta\boldsymbol{\sigma}$ along the vertical and horizontal directions respectively. These can be expressed as:

$$D_{x,y}^{h}(\Delta\boldsymbol{\sigma}) = \begin{cases} \Delta\boldsymbol{\sigma}_{x,y} - \Delta\boldsymbol{\sigma}_{x+1,y} & 1 \le x < P \\ 0 & x = P \end{cases} \tag{2.19}$$

$$D_{x,y}^{v}(\Delta\boldsymbol{\sigma}) = \begin{cases} \Delta\boldsymbol{\sigma}_{x,y} - \Delta\boldsymbol{\sigma}_{x,y+1} & 1 \le y < P \\ 0 & y = P \end{cases} \tag{2.20}$$

where, P is the number of pixels in each direction. As indicated by (2.18), TV regularisation can be regarded as a particular form of sparsity regularisation, which promotes a solution with sparse image gradient. An explicit way to solve TV regularisation is to employ the gradient-based recovery method (Beck and Teboulle, 2009, Yang and Peng, 2013).

In addition to the regularisation approaches with a single penalty term, joint regularisation methods simultaneously considering multiple *a priori* knowledge have also been proposed for EIT image reconstruction. Compared with the single regularisation approaches, these methods are effective for the cases that multiple *a priori* knowledge are available and the results are expected to demonstrate all the

features considered. For example, the combined TV and Tikhonov regularisation method (Liu et al., 2013) and, the joint l_1 and TV regularisation method (Hao and Xu, 2016) have been reported. This category can be generally formulated as:

$$\Delta\boldsymbol{\sigma}_{reg} = \arg\min_{\Delta\boldsymbol{\sigma}} \left\{ \frac{1}{2} \left\| \mathbf{J}\Delta\boldsymbol{\sigma} - \Delta\mathbf{V} \right\|_2^2 + \sum_{i=1}^{n} \lambda_i \, \mathrm{R}_i \left(\Delta\boldsymbol{\sigma} \right) \right\} \tag{2.21}$$

where λ_i and R_i denote the i^{th} regularisation parameter and regularisation function respectively.

Compared with the one-step algorithms, the iterative methods, including (2.16) and (2.17), can provide much better image qualities at the expense of greatly increased computational complexity. As a result, such methods are usually time-consuming thus are employed primarily for off-line analysis.

2.4.2 Direct Reconstruction Methods

Another emerging approach is the direct reconstruction methods on the basis of a mathematical proof by A. Nachman (Nachman, 1996). These departs from the regularisation based algorithms previously discussed, in that these methods can obtain the gray-scale values of the reconstructed images non-iteratively and independently. The foundation of the method is to transform the nonlinear conductivity equation to the Schrödinger equation and use the method of inverse scattering to solve the resulting inverse problem (Mueller et al., 2002). The main steps of performing EIT image reconstruction based on the direct methods are as follows:

1) Using the Dirichlet-to-Neumann map to calculate the scattering transform **t** which is stated by:

$$\mathbf{t}(k) = \int_{\partial\Omega} e^{i\bar{k}\bar{z}} (\Lambda_\sigma - \Lambda_1) \varphi(z,k) d\sigma(z) \tag{2.22}$$

where Λ_σ and Λ_1 denote the voltage to current map when the conductivity distribution in Ω is $\sigma(z)$ and one, respectively; $k=k_1+ik_2$ is a complex parameter

rather than zero; $z=x+iy$ represents a point (x, y) in Ω and $\varphi(z, k)$ is a unique solution of the Schrödinger equation.

2) Using the $\bar{\partial}$ method to reconstruct σ, which is stated by:

$$\frac{\partial}{\partial \bar{k}} \mu(z,k) = \frac{1}{4\pi\bar{k}} \mathbf{t}(k) e^{i(kz+\bar{k}\bar{z})} \overline{\varphi(z,k)} \tag{2.23}$$

$$\sigma(z) = \left\{ \lim_{k \to 0} \mu(z,k) \right\}^2 \tag{2.24}$$

Direct-reconstruction based EIT imaging has been investigated thoroughly utilising various algorithms, for instance, the dbar method (Mueller et al., 2002, Hamilton and Mueller, 2013, Cao et al., 2010), the Calderon's method (Cao et al., 2009), the enclosure method (Cao and Xu, 2011) and the factorization method (Cao et al., 2011), etc. The direct methods provide an easily implemented way to solve the complicated nonlinear problem. However, the image quality of such methods has not been evaluated and compared systematically with the regularisation based methods.

2.4.3 Statistical Methods

Statistical solutions to inverse problems have been continuously studied since decades ago (Mosegaard and Rygaard-Hjalsted, 1999, Stuart, 2010). The statistical methods consider the EIT problem in the framework of Bayesian statistics by recasting the inverse problem into a form of statistical inference (Kaipio et al., 2000, Watzenig and Fox, 2009). In contrast to the regularisation based methods, the Bayesian statistical framework estimates the posterior distribution of the unknown parameters on the premise of the measured data. On the basis of the posterior density, estimation of the conductivity distribution as well as *a posteriori* uncertainties can be calculated.

Given that the case of additive noise **e** in (2.4) has the probability density function $\pi_e(e)$, which is usually a multivariate Gaussian distribution (Kaipio and Somersalo, 2006), as expressed by:

$$\pi_e(\mathbf{e}) \propto \exp\left[-\frac{1}{2}(\mathbf{e}-\boldsymbol{\gamma})^t \boldsymbol{\Sigma}^{-1}(\mathbf{e}-\boldsymbol{\gamma})\right] \tag{2.25}$$

where $\boldsymbol{\gamma}$ is the mean vector and $\boldsymbol{\Sigma}$ is the covariance matrix. Following from (2.25), the likelihood function is expressed as:

$$l(\mathbf{V} \mid \boldsymbol{\sigma}) = \pi_e(\mathbf{V} - \mathrm{F}(\boldsymbol{\sigma})) \tag{2.26}$$

The interference of the conductivity distribution $\boldsymbol{\sigma}$ is then based on the posterior density, which is formulated as:

$$\pi(\boldsymbol{\sigma} \mid \mathbf{V}) = \frac{l(\mathbf{V} \mid \boldsymbol{\sigma})\pi(\boldsymbol{\sigma})}{\pi(\mathbf{V})} \tag{2.27}$$

Finally, the solution to the inverse problem is formulated as the expectations over the posterior, which is stated by:

$$E(f(\bullet)) = \int_{\Theta} f(\boldsymbol{\gamma})\pi(\boldsymbol{\gamma} \mid \mathbf{V}) d\boldsymbol{\gamma} \tag{2.28}$$

where Θ denotes the parameter space. Monte Carlo approximations can be employed in the case that (2.28) cannot be solved analytically.

Since the *a priori* knowledge of the measurement noise is considered under the framework of Bayesian statistics, statistical methods exhibit stronger capabilities with respect to noise tolerance in comparison with the deterministic reconstruction methods. However, the computation cost of these methods is usually high.

2.4.4 Other Emerging Methods

Aside from the well-investigated image reconstruction algorithms presented above, a series of novel methods have emerged for the purposes of various applications, such as the reconstruction of phase boundaries in multiphase flow measurement (Ren et al., 2014), etc. Representative examples include the shape-based algorithm for inclusion shapes reconstruction using Boundary Element Method

(BEM) rather than the traditional Finite Element Method (FEM) (Ren et al., 2014, Babaeizadeh and Brooks, 2007), the algorithm using impedance spectral constraints for direct and simultaneous use of multifrequency data (Malone et al., 2014), the Artificial Neural Networks (ANNs) based algorithms with fast convergence rates (Martin and Choi, 2016), and the machine learning based reconstruction and classification algorithms (Malone et al., 2015), etc. These emerging algorithms usually make use of specific characteristics associated with a particular application therefore exhibit poor universality.

2.4.5 EIDORS: Electrical Impedance Tomography and Diffuse Optical Tomography Reconstruction Software

With respect to EIT image reconstruction algorithms, it is also worth mentioning a Matlab toolkit named EIDORS (Electrical Impedance and Diffuse Optical Tomography Reconstruction Software), which was initially developed by the University of Kuopio. EIDORS is an open-source software extensively used by EIT researchers for forward modelling and image reconstruction (Vauhkonen et al., 2001, Polydorides and Lionheart, 2002, Adler and Lionheart, 2006). Since its emergence in 2001 (Vauhkonen et al., 2001), it has evolved from dealing with 2D problems to 3D models. Common regularisation based EIT image reconstruction algorithms have been included in EIDORS, such as the Tikhonov regularisation, the one-step Gauss-Newton regularisation with smoothness prior, the TV regularisation approach, and the one-step Gauss-Newton regularisation with NOSER prior, etc. Apart from the basic image reconstruction approaches, EIDORS also investigates mesh generation, electrode modelling, visualisation and electrode error detection. Some typical biomedical application cases such as imaging of neonates' lungs (Heinrich et al., 2006) and changes in ventilation after lung injury (Frerichs et al., 1998) are also introduced.

2.5 Applications of EIT in Cellular Imaging

As mentioned before, this thesis focuses on advancing EIT instrumentation and image reconstruction algorithms for biomedical imaging, with particular

emphasis on 3D cell culture imaging. In this section, the current status of EIT's application in cell imaging is briefly reviewed.

Cell culture is extensively undertaken in the biotechnology industry, pharmaceutical industry, as well as research laboratories. For numerous investigative purposes during bioprocesses, cells can be passaged, cultivated, transformed, and/or transplanted (Peterson et al., 1979). In each of these operations, it is necessary to understand the status of the cells *in vitro*. Beyond that, improvement of product quality in highly sophisticated cell-based production processes requires sensing of key process variables in real time and imposing corrective actions when necessary (Zhao et al., 2015). Compared to the conventional 2D cell culture (Cukierman et al., 2001), 3D cell cultures can provide more realistic environments for *in vitro* cells to better approximate *in vivo* conditions (Breslin and O'Driscoll, 2013). In particular, cell spheroids are regarded as a step-change in drug discovery. As a result, real-time quantitative imaging of 3D cell cultures are becoming highly desirable for the study of biological behaviour and control of chemical environments; for example, for the visualisation of cell adhesion, spreading, proliferation and detachment in cell cycle processes, cellular morphology and cell-drug interaction, etc. (Rahman et al., 2008). Various sensing or imaging techniques for cell culture imaging/monitoring have been proposed and investigated in the past few decades. Such techniques include electrical-based methods, i.e., impedance spectroscopy (K'Owino and Sadik, 2005, Rahman et al., 2008, Bagnaninchi and Drummond, 2011, Holmes et al., 2014, Canali et al., 2015), and optics based methods such as Raman spectroscopy (Abu-Absi et al., 2011, Mouras et al., 2013) and microscopic imaging (Guez et al., 2004). Compared with most optics based methods and typical electroanalytical techniques, impedance spectroscopy can provide a better characterisation of cellular properties (K'Owino and Sadik, 2005). However, commonly used impedance spectroscopic methods utilise two electrode systems and consequently lack spatial resolution.

EIT can offer non-destructive, real-time, continuous, label-free, qualitative and under certain circumstances, quantitative visualisation, with spatial-temporal resolution. Such features make EIT a promising technique for cellular imaging and bioprocess monitoring, and some pioneering work from both theoretical and practical

aspects have been reported recently. For example, the effect of cell membranes on tissue admittance was investigated and a mathematical framework regarding this issue was derived (Ammari et al., 2016a). A mathematical framework for determining the microscopic properties of the cell culture from spectral measurements has also been proposed (Ammari et al., 2016b), while multi-frequency measurements were demonstrated to be effective for improving stability and resolution of EIT (Alberti et al., 2016). Additionally, EIT has also been explored towards on-chip cellular imaging (Sun et al., 2010), single cell freezing monitoring (Hiraga et al., 2013) and single cell electroporation imaging (Meir and Rubinsky, 2014, Ammari et al., 2017).

The abovementioned work highlights the potential of EIT for cell substrate sensing and cellular imaging. However, a great deal of challenges still remain unsolved before EIT can be recognised as a practical technique for cellular imaging. These challenges include: a) miniature biosensor design for optimal 2D/3D imaging performance; b) high spatial resolution image reconstruction for weak and small dimension conductivity variation and c) long-term real-time monitoring of cellular dynamics, cross validation and interpretation of the results.

2.6 Summary

This chapter briefly reviewed the EIT technique from the perspectives of fundamental theory, typical composition of an EIT system, existing biomedical EIT systems, the cutting edge EIT image reconstruction algorithms and the recent advances of EIT in cellular imaging. The purpose of the chapter was to help understand the state-of-the-art EIT techniques, its future development trends, and the emerging or potential applications with maximum utilization of the many merits of EIT. The innovative work and scientific contribution of the thesis from these perspectives will be demonstrated subsequently in the following chapters.

Chapter 3 A Multi-frequency EIT System for Real-time 2D/3D Biomedical Imaging

3.1 Introduction

One of the primary targets of applying EIT in biomedical applications is to monitor and assess the biological dynamics for the study of biological behaviour or control of chemical environment of the bioprocess. As the bioimpedance varies over a wide range of frequencies, spectral electrical properties of biological tissues may provide a wealth of information for bioprocess evaluation, physiological status analysis and pathological diagnosis. Therefore, compared with the mono-frequency EIT, which is normally employed in industrial process applications, multi-frequency EIT (mfEIT), which injects simultaneously a current with multiple frequency components, tends to be more attractive in biomedical imaging.

In this chapter, the development and evaluation of a novel mfEIT system with advanced features are presented for biomedical imaging. The mfEIT system supports up to 32 electrodes and its working frequency ranges from 10 kHz to 1 MHz. Novel features of the presented mfEIT system include: a) a fully adjustable multi-frequency current source with real-time current monitoring and emergency switch-off functions are proposed for sensing flexibility and safety concerns; b) a flexible switching scheme is developed to enable arbitrary sensing strategy; c) a semi-parallel data acquisition scheme is deployed for enhanced frame rate; additionally, a parallel digital signal processing technique, i.e. simultaneous multi-frequency digital quadrature demodulation, is performed in a high-capacity FPGA for enhanced real-time performance; d) a real-time 3D imaging software, namely *Visual Tomography*, is developed for rapid online 2D and 3D image reconstruction, visualisation, data analysis and parameters configuration. These novel features promotes the real-time 2D and 3D imaging ability, sensing flexibility and high frame rate, which are demanded desperately towards the practical applications of EIT in biomedical imaging. The performance of the mfEIT system is evaluated systematically from the

aspects of the resistance load capacity, SNR, frame rate, 2D and 3D multi-frequency image reconstructions.

3.2 System Design

3.2.1 System Architecture

Figure 3-1 shows the picture of the developed mfEIT system where each function module is annotated. Figure 3-2 illustrates the block diagram of the system architecture. The system mainly comprises three parts, i.e., the mains part, the applied part and the peripheral equipment. The mains part is packed in the power box together with an external AC/DC power supply to provide multiple isolated power tracks. Most of the applied part is included in the main box, which contains a fully adjustable multi-frequency current source, a dual-channel real-time current monitoring module, an arbitrarily configurable multiplexer array, a semi-parallel differential voltage measurement, signal conditioning and data acquisition module, a high-capacity FPGA for digital signal processing and control tasks, an isolated USB 2.0 interface, a wireless Bluetooth interface and an Ethernet data link to the computer. The external laptop is installed with the developed real-time 3D imaging software, *Visual Tomography*. It integrates the real-time 2D and 3D image reconstruction, visualisation, data analysis, sensing parameters configuration and system control functions.

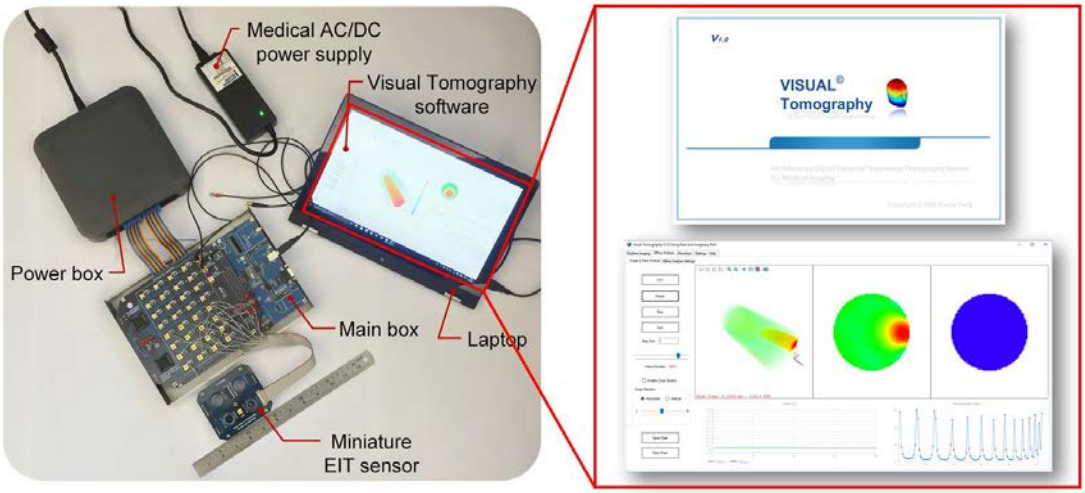

Figure 3-1 Picture of the developed mfEIT system.

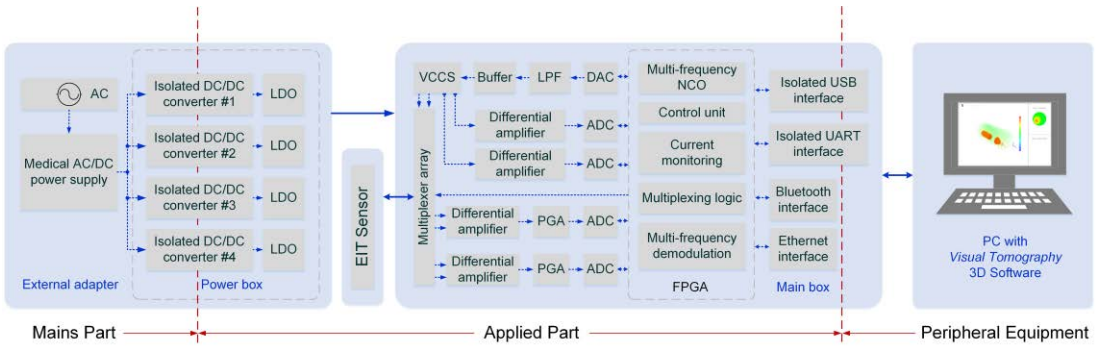

Figure 3-2 Block diagram of system architecture.

3.2.2 Adjustable Multi-frequency Current Source

A fully adjustable multi-frequency current source (AMFCS) with real-time current monitoring and emergency switch-off functions were designed. Figure 3-3 shows the block diagram of the proposed AMFCS. The AMFCS was implemented based on the Direct Digital Synthesis (DDS) technology (Hickman, 1992). Two commercially available Numerically Controlled Oscillator (NCO) Intellectual Property (IP) cores were utilised to generate two discrete sinusoidal waveforms with different frequencies. The frequency and phase of each sinusoidal waveform could be configured digitally via *Visual Tomography* in real time by adjusting corresponding control words. The two-frequency discrete waveforms were then added up to generate a single superimposed waveform. Two examples are illustrated in Figure 3-4. Figure 3-4(a) shows a superimposed waveform, which is composed of 50 kHz and 100 kHz frequency components. Figure 3-4(b) presents another waveform, which is a superposition of 50 kHz and 200 kHz frequency components. In time-difference (TD) imaging mode, the second NCO can be disabled by *Visual Tomography* in order to generate adjustable mono-frequency currents.

A 14-bit, 210 MSPS Digital-to-Analog Converter (DAC) was utilised to generate a stepwise, continuous sinusoidal waveform. The DAC's external reference voltage was controlled digitally by an 8-bit DAC, leading to a current output whose amplitude was 256-level adjustable. A 5^{th} order elliptic Low Pass Filter (LPF) was adopted as the reconstruction filter. Its cut-off frequency can be manually selected as 500 kHz or 1 MHz, according to the current frequencies applied. The voltage

controlled current source (VCCS) was built based on the principle of enhanced Howland current source (Rafiei-Naeini and McCann, 2008). The maximum amplitude of output current was 10 mA peak to peak due to the limitation of the amplifiers' power supply.

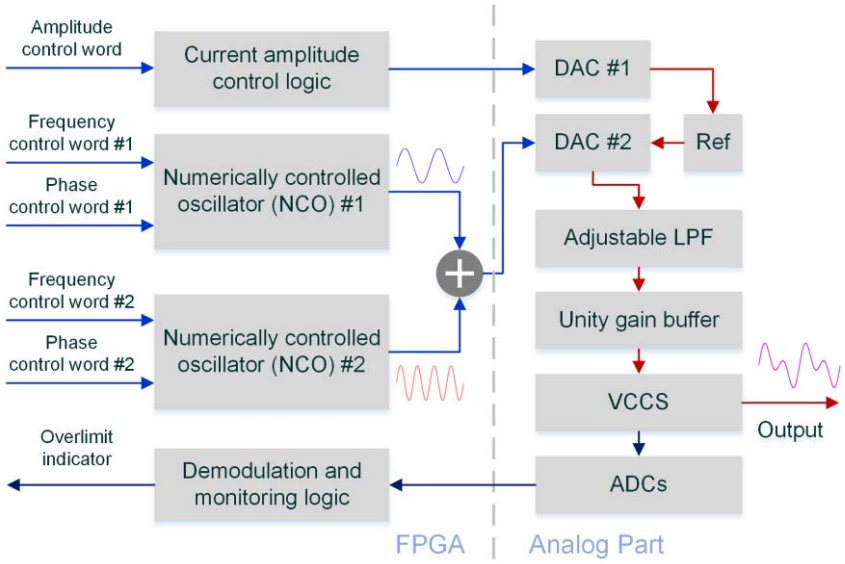

Figure 3-3 Block diagram of the adjustable multi-frequency current source with real-time current monitoring function.

(a) (b)

Figure 3-4 Example of superimposed waveforms. (a) 50 kHz and 100 kHz superimposed waveform (yellow) and its frequency spectrum (purple). (b) 50 kHz and 200 kHz superimposed waveform (yellow) and its frequency spectrum (purple).

Figure 3-5 illustrates the load capacity testing result by using resistive loads ranging from 19.9 ohm to 815.9 ohm when the current excitation frequencies are set as 20 kHz, 500 kHz and 1 MHz respectively. The results demonstrate strong linear

relationships of the induced voltages with the increase of resistance under three different frequencies.

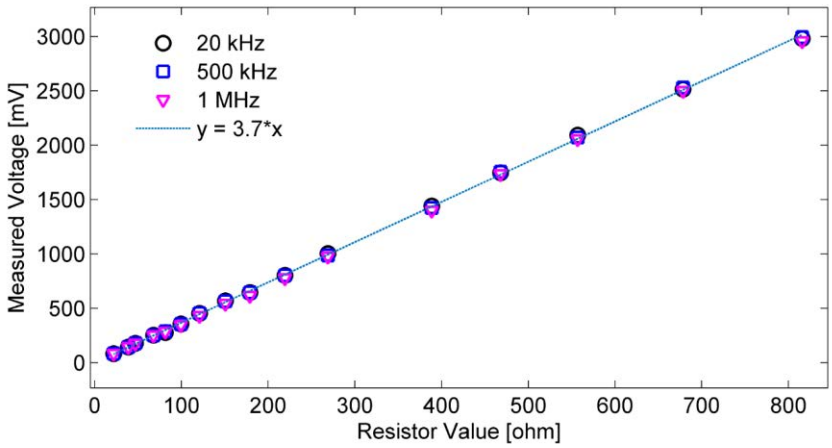

Figure 3-5 Resistive load testing curve of 20 kHz, 500 kHz and 1 MHz current injection.

In order to monitor the current amplitude, a high-precision 100 ohm resistor with ±0.1% tolerance was also inserted in series with each current output end and the voltage drops on the resistors were sampled in real time. Under the circumstances of component failure or electromagnetic interference, if the amplitude of the current exceeds the designed limit, both NCOs will be disabled and all switches will be disconnected with a response time of 100 us level. This function is realised in order to guarantee that the amplitudes of injected currents conform to the safety standards of medical equipment, e.g. IEC60601-1 (Sidebottom et al., 2006), when the system is applied for biomedical applications.

3.2.3 Configurable Multiplexer Array

The designed mfEIT system supports up to 32 electrodes and, it can be cascaded to work on sensors with a larger number of electrodes. In order to obtain the optimal sensing performance, a fixed sensing strategy, for example the prevailing adjacent drive and receive strategy (Brown and Seagar, 1987), might not be ideal for all the cases. Therefore, the support of user-defined sensing strategies is preferable in an EIT system (Yang et al., 2017b). In order to be compatible with flexible sensing

strategies, an arbitrarily configurable switching scheme was designed in this mfEIT system.

Figure 3-6 illustrates the proposed switching scheme for an individual electrode. In the switch array board, there are 32 dual single pole single throw switches for current injection switching and two cascaded 8×16 cross point switch arrays are used for selecting induced voltage measurement channels. By using the configurable switching scheme, each electrode can be connected to either the complementary current injections or any voltage measurement channels. Moreover, the real-time rewrite of sensing protocol can be realised in the PC software, *Visual Tomography*.

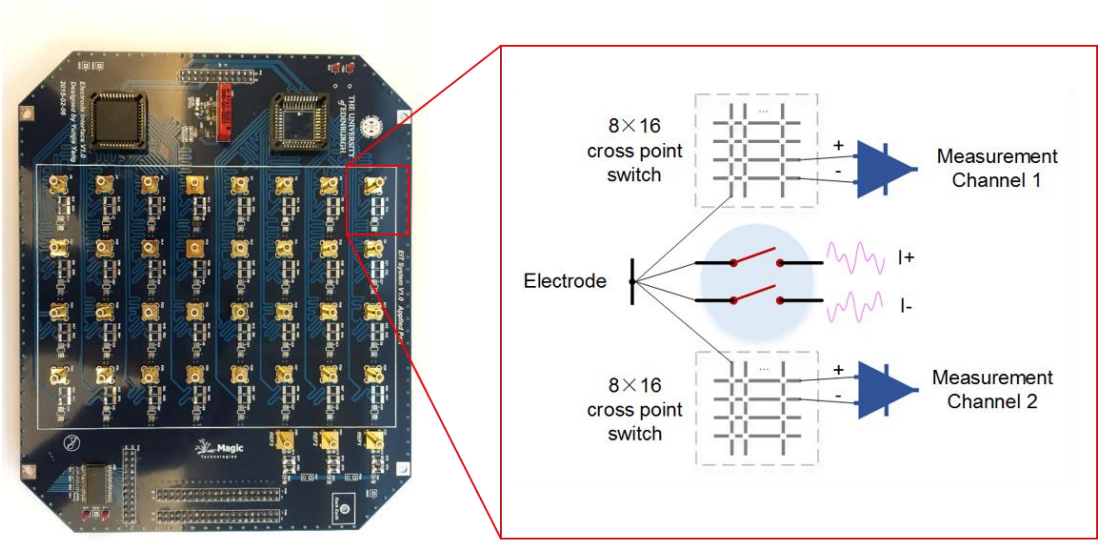

Figure 3-6 Switching scheme for an individual electrode.

3.2.4 Semi-parallel Data Acquisition Scheme

As shown in the applied part of Figure 3-1, in order to increase the frame rate of the system while reducing the complexity of the circuits, a semi-parallel data acquisition scheme was designed. Two differential voltage measurement, signal conditioning and data acquisition channels were implemented. The two channels could work in either semi-parallel mode or serial mode according to the setup in the *Visual Tomography* software. In the serial mode, only one selected channel

performed data acquisition, while the other channel remained in an idle state. Alternatively, in the semi-parallel mode, two Analog-to-Digital Converter (ADC) performed data acquisition simultaneously. In this case, the total data acquisition time for one completed scan (e.g., there are 104 data of a 16-electrode sensor using the adjacent strategy) could be reduced to nearly the half. In each measurement channel, a Programmable Gain Amplifier (PGA) was cascaded with the front-end instrument preamplifier. The combination could provide a digitally adjustable gain from 0.56 to 70. A 16-bit, 10 MSPS, low noise ADC was adopted for high speed and high performance signal acquisition. The SNR of the ADC was 91.5 dB with 16-bit no missing codes.

Figure 3-7 presents the diagram of the sampling timing. The number of sampling points for a demodulation was set to be 200 (note that for 625 kHz, the number of points was 160 rather than 200), but adjustable via the PC software. A fixed ADC sampling frequency was not optimal for all frequencies within the wide system bandwidth, because the number of sampling points could vary significantly. Therefore, the ADC sampling frequency of the designed mfEIT system was changed adaptively in order to pursue a minimum number of demodulation periods, when the total accumulation number for a demodulation was fixed. As indicated in the figure, a measurement time slot was composed of a period for switching and settling, then several periods for a demodulation. Accordingly, the frame rate *fps* could be calculated by:

$$fps = \frac{f_{sg}}{\left(\frac{P}{f_{sp}} f_{sg} + 1\right) N} \tag{3.1}$$

where f_{sg} and f_{sp} denote the signal frequency and sampling frequency respectively; P is the total number of points for a demodulation process; N is the total measurement number of a completed data frame. Under the semi-parallel mode, N could be reduced approximately to the half of that under the serial mode; therefore, the frame rate can nearly be doubled.

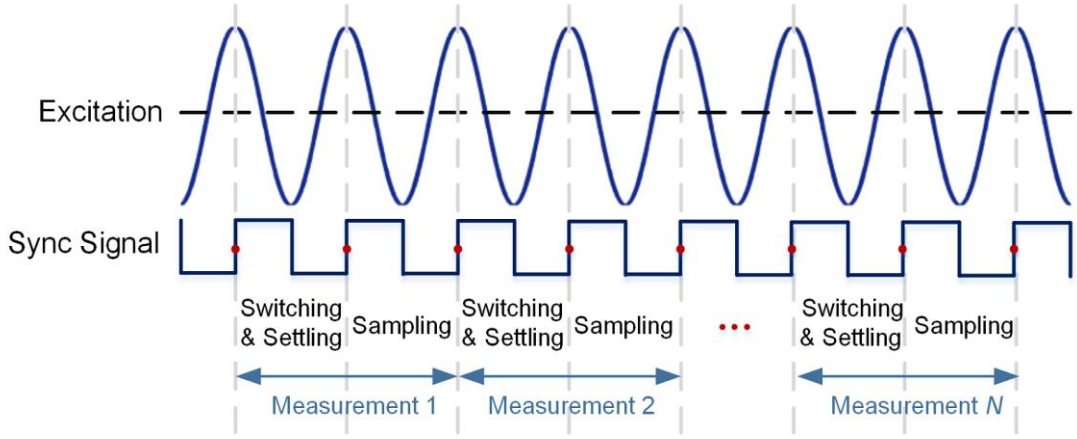

Figure 3-7 Diagram of signal sampling timing sequence.

Table 4-1 demonstrates the frame rates achieved by the mfEIT system under different working frequencies and sensing modes. The frame rates were obtained based on a 16-electrode EIT sensor for the 2D cases (there were 104 independent measurements in a full scan) and a 32-electrode EIT sensor for the 3D cases (there were 208 independent measurements in a full scan). As indicated by Table 4-1, the maximum frame rate achieved by the serial mode was 546 fps at 625 kHz; and up to 1014 fps imaging could be supported by using the semi-parallel mode.

Table 4-1. Frame rates [fps] under different frequencies and working modes.

Sensing mode	**10 kHz**	**20 kHz**	**40 kHz**	**50 kHz**	**100 kHz**	**200 kHz**	**400 kHz**	**500 kHz**	**625 kHz**	**1 MHz**
2D serial	48	96	192	240	320	384	427	437	546	457
2D semi-parallel	89	178	356	445	595	714	793	811	1014	850
3D serial	24	48	96	120	160	192	213	218	273	228
3D semi-parallel	44	89	178	222	297	357	396	405	507	425

3.2.5 Simultaneous Multi-frequency Demodulation

The simultaneous multi-frequency digital quadrature demodulation was designed and implemented in a high capacity FPGA in this work, in order to acquire simultaneously the real and imaginary parts of both frequency components. The superimposed signal with two frequency components was sampled by the high-speed ADC, which can be expressed as:

$$s(n)=\sum_{i=1}^{2} A_i \sin\left(\frac{2\pi}{N_i}n+\theta_i\right) \tag{3.2}$$

where A_i denotes the amplitude of the i^{th} frequency component; θ_i is the phase angle of the i^{th} frequency component; N_i is the sampling number in one period of the i^{th} frequency component. In this work, $N_1>N_2$ and N_1 is required to be the multiple of N_2, i.e., $N_1=qN_2$, $q>1$, $q\in Z$.

Further, the principle of multi-frequency digital quadrature demodulation can be formulated as

$$\begin{cases} I_i=\dfrac{2}{N_1}\displaystyle\sum_{n=0}^{N_1-1}\sin\left(\frac{2\pi}{N_i}n\right)s(n)=A_i\cos(\theta_i) \\ Q_i=\dfrac{2}{N_1}\displaystyle\sum_{n=0}^{N_1-1}\cos\left(\frac{2\pi}{N_i}n\right)s(n)=A_i\sin(\theta_i) \\ i=1,2 \end{cases} \tag{3.3}$$

where I_i and Q_i are the real and imaginary parts of the i^{th} frequency component of the sampled signal $s(n)$, respectively. On the basis of (3.3), the amplitude and phase angle of each frequency component can be derived, as expressed by using the following equation:

$$\begin{cases} A_i=\sqrt{I_i^2+Q_i^2} \\ \theta_i=\tan^{-1}\dfrac{Q_i}{I_i} \\ i=1,2 \end{cases} \tag{3.4}$$

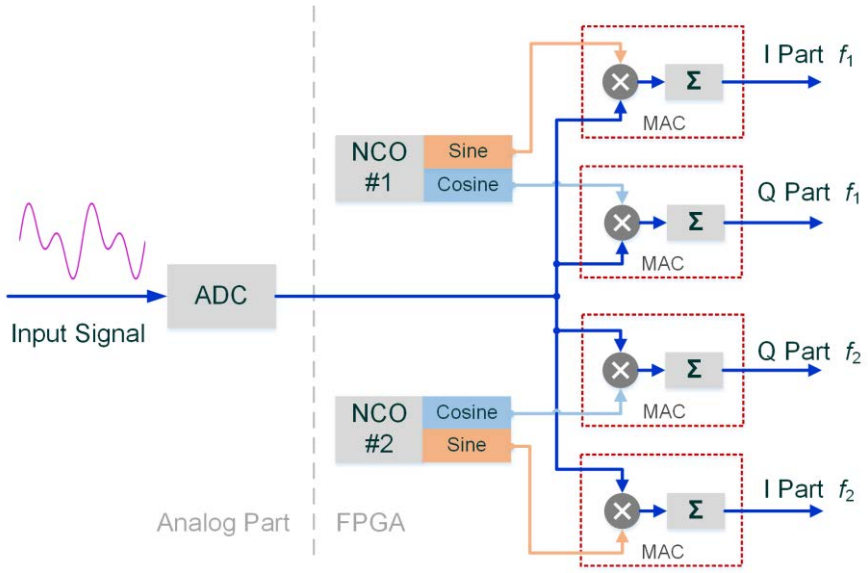

Figure 3-8 Block diagram of multi-frequency digital quadrature demodulation.

As shown in Figure 3-8, the multi-frequency digital quadrature demodulation was implemented in the FPGA by using a parallel architecture in order to achieve simultaneous demodulation of the real parts, i.e. I parts in (3.3), and imaginary parts i.e. Q parts in (3.3), of the two frequency components. Four Multiply-Accumulator (MAC) IP cores were utilised in each measurement channel to realise the function. Based on (3.3) and (3.4), the *Visual Tomography* software could provide the reconstructed images either based on the real and imaginary part data or the amplitude and phase angle data.

3.2.6 Adjustable Isolated Power Supply

In order to comply with the IEC 60601-1 medical equipment standard (Sidebottom et al., 2006) and meanwhile provide high efficiency, ultra-low noise, and flexible power supplies, an adjustable isolated power supply scheme, as shown in the mains part in Figure 3-1, was proposed. A medical AC/DC power supply with 4000 VAC input to output (I/O), 2 × MOPP isolation was firstly used to provide a 12 V DC output with a maximum output current of 7.08 A. Four high efficiency DC/DC converters with 3000 VAC I/O, 2 × MOPP isolation were then employed to provide separate base voltages for the analog part (+12V, –12V), the digital part (5V), the ADCs (12V) and DACs (5V) respectively. Finally, the adjustable, ultralow noise

low-dropout (LDO) regulators with analogue filters were adopted to generate exactly the required power tracks for each part. The power supplies were adjustable through the jumpers on the board within the range of 1.4~20.5 V in order to meet various power supply requirements. The DC/DC converter plus ultralow noise LDO architecture was able to provide isolated, efficient, low noise and flexible power supplies.

3.2.7 Isolated Data Link

To ensure safe operation in biomedical equipment for advanced diagnostics, measurement and long-term monitoring, isolation of data link is also necessary. For this goal, in the designed mfEIT system, a 5 kV Universal Serial Bus (USB) digital isolator compatible with the full/low speed USB peripheral, was applied together with a USB 2.0 microcontroller, in order to provide an isolated full speed (12 Mbps) USB 2.0 data link. For debugging purpose, a serial Universal Asynchronous Receiver/Transmitter (UART) interface was also implemented and isolated by using a dual-channel, 2.5 kV isolator. Additionally, the mfEIT system provided extension ability to interface with a plug-in Ethernet module for the purpose of remote upgrade, data collection and fault diagnosis purpose and a wireless Bluetooth module for image monitoring on mobile devices.

3.2.8 Real-time 3D Imaging Software: *Visual Tomography*

The open-source Matlab toolbox, i.e. EIDORS, was developed a decade ago to provide commonly used algorithms for 3D forward modelling and inverse problems (Polydorides and Lionheart, 2002). However, the real-time 3D imaging ability that can cooperate directly with an EIT system still remains a gap. In this work, another novel feature integrated is the online and offline 2D/3D imaging ability and flexible control of sensing parameters. These functions were realised by a newly developed 3D imaging software, i.e. *Visual Tomography*. As shown in Figure 3-9, the software was mainly composed of five function units, including: (1) the settings unit for sensing mode and sensing parameters selection; (2) the waveform unit for single-channel signal sampling and instant display; (3) the real-time imaging

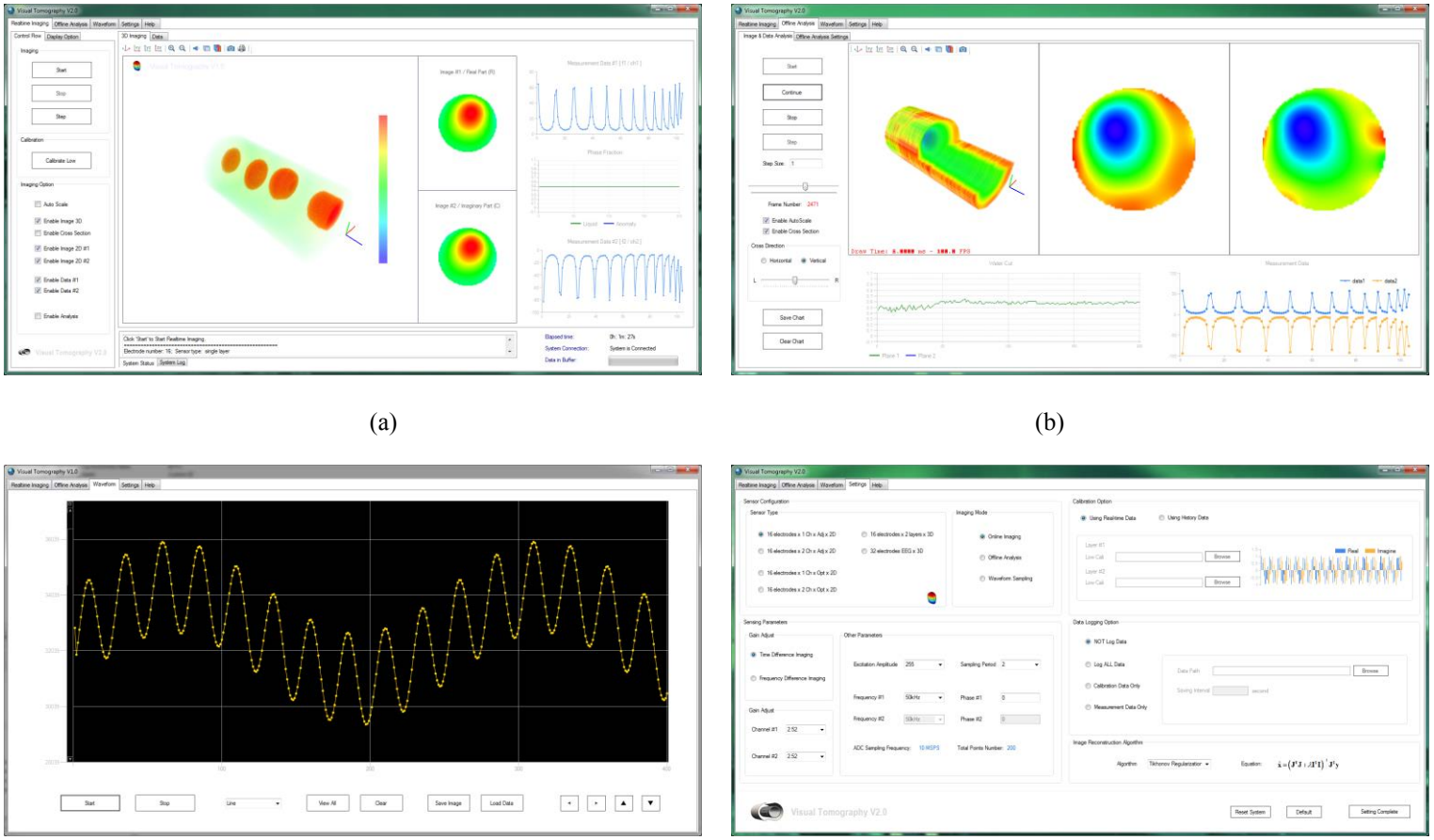

(a) (b)

(c) (d)

Figure 3-9 3D imaging software, *Visual Tomography*. (a) Real-time imaging unit. (b). Offline analysis unit. (c) Waveform sampling unit. (d) Settings unit.

unit for online 2D and 3D image and data visualisation; (4) the offline analysis unit for data replay and complex process parameters calculation, for instance, phase concentration in a multiphase mixture and (5) the help unit for guidance and supplementary information with respect to the use of the software.

The software provides access to the majority of sensing parameters. These parameters include the sensor type, imaging mode, gain adjustment of each measurement channel, current amplitude, sampling periods, current frequency, current phase angle, sampling frequency, total number of data points for a demodulation, and image reconstruction algorithms. The modification of parameters are accomplished by changing the setting of the software. This feature enables highly flexible sensing ability without modifying the hardware circuitry and the FPGA firmware.

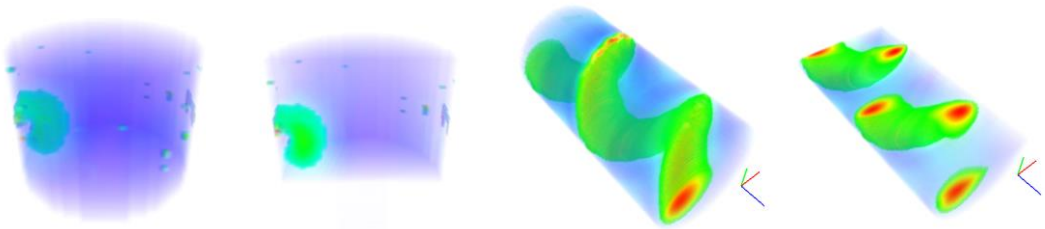

(a) (b) (c) (d)

Figure 3-10 Real-time 3D imaging examples. (a) Online spatial 3D imaging of a potato. (b) Vertical sectional view of (a). (c) Online time-stacked 3D imaging of a rotating rod. (d) Horizontal sectional view of (c).

Real-time 2D and 3D imaging functions were realised by using the multithreading technique and OpenGL library (Lalonde and Pugh, 1995, Yin et al., 2001). The software supported not only real-time time-stacked 3D imaging for revealing the dynamic behaviour of the measurement object in the time domain, but also real-time true spatial 3D imaging for the rapid indication of conductivity distribution in a 3D spatial domain. Figure 3-10 illustrates four real-time 3D imaging examples, i.e. true 3D spatial images in Figure 3-10(a) and Figure 3-10(b) and time-stacked 3D images in Figure 3-10(c) and Figure 3-10(d). By default, Tikhonov regularisation method (Vauhkonen et al., 1998) was adopted for real-time image reconstruction due to its low computational cost. The frame rate of 3D displaying

was approximately 100 fps. The 3D imaging area also supported basic user interaction functions, for example, object rotation, drag and drop, zoom in/out, and cross sectional display. The real-time 3D imaging ability could help understand in depth the temporal and spatial characteristics of the conductivity variation associated with the physiological dynamics in biomedical applications.

3.3 System Evaluation

3.3.1 Signal to Noise Ratio (SNR)

In this subsection, the SNR of the designed mfEIT system under a range of working frequencies was evaluated. Raw measured data after three times' average were used to calculate the SNR. The measurements were continuously performed on a 16-electrode EIT sensor. The inner diameter of the sensor was 94 mm. Saline with a conductivity of 0.07 $S \cdot m^{-1}$ was selected as the measuring object. The adjacent current injection and measurement strategy was adopted. It generated 104 independent measurements in a full scan for reconstructing one frame of image.

The SNR of each sensing channel was calculated by:

$$\mathrm{SNR} = 10 \log \frac{\sum_{n=1}^{N} \left[y(n) \right]^2}{\sum_{n=1}^{N} \left[y(n) - y_m \right]^2} \tag{3.5}$$

where N denotes the number of measurements and N=1000 in this work; $y(n)$ and y_m are the n^{th} measured voltage data and the average of N frames of voltage data, respectively.

Figure 3-11 shows the SNR of 104 measurement channels when the current frequency was set as 10 kHz, 20 kHz, 40 kHz, 50 kHz, 100 kHz, 200 kHz, 400 kHz, 500 kHz, and 625 kHz respectively. By observing the results, it is found that the SNR curves have the similar trend with the measured voltage data. That is, the higher SNR is obtained by the adjacent electrode measurements, which have a larger transimpedance, and in contrast, the lower SNR is obtained by the opposite-electrode measurements, which have a smaller transimpedance.

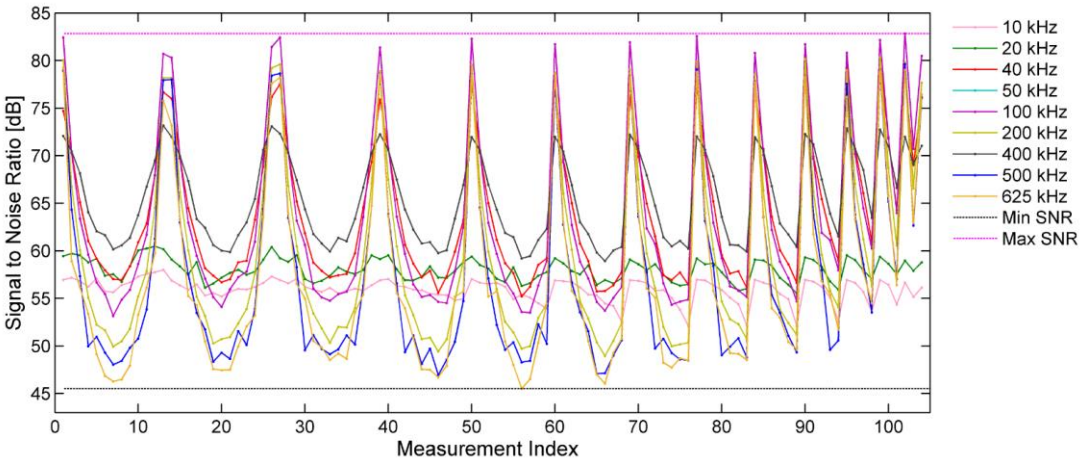

Figure 3-11 SNR of different current frequencies on the test EIT sensor.

As indicated by Figure 3-11, the highest SNR under the testing conditions is 82.82 dB and the lowest SNR is 45.51 dB. The results suggest that the lower frequencies have a relatively lower measurement uncertainties when compared with the higher ones, but overall, the measurements obtained from all frequencies are stable enough for performing robust image reconstruction. If needed, the SNR can be further improved by either increasing the number of accumulation points in (3.3) during the digital demodulation procedure or averaging a larger number of a single measurements, at the expense of reduced frame rate.

3.3.2 2D Time-Difference (TD) and Frequency-Difference (FD) Imaging Results

A number of 2D multi-frequency TD and FD imaging experiments were carried out and the results were presented and discussed in this subsection. The TD and FD imaging methods can be referred to (2.7) and (2.8) in Chapter 2. These experiments were performed on the same sensor as used in the evaluation of SNR, which is shown in Figure 3-12(a). The background substance in this test was saline with a conductivity value of 0.07 $S \cdot m^{-1}$. Multi-frequency image reconstructions of two test phantoms, i.e. a single sweet potato cylinder and a potato cylinder with a metal cylinder, were performed. Figure 3-12(b) to (e) illustrate the phantom pictures and corresponding geometric distributions of the objects respectively. The diameters

of the sweet potato cylinder, potato cylinder and metal rod are 20 mm, 20 mm and 25 mm, respectively.

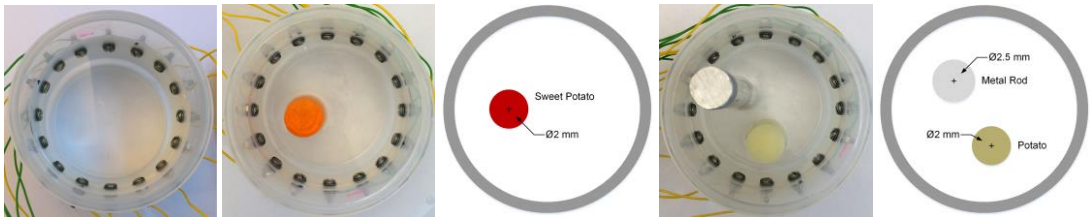

(a) (b) (c) (d) (e)

Figure 3-12 Experiment test phantoms using a 16-electrode EIT sensor. (a) The sensor. (b) Phantom 1: sweet potato rod. (c) Geometric distribution of phantom 1. (d) Phantom 2: potato rod and metal rod. (e) Geometric distribution of phantom 2.

The one-step Gauss-Newton solver with Laplacian regularisation (Yang et al., 2014) as stated by (2.14) in Chapter 2 was utilised for image reconstruction. In order to compare quantitatively the quality of the reconstructed images, the Correlation Coefficient (CC) of each image was calculated, which is defined by:

$$\mathrm{CC} = \frac{\sum_{i=1}^{p}\left(\Delta\boldsymbol{\sigma}_{i,est} - \Delta\boldsymbol{\sigma}_{m,est}\right)\left(\Delta\boldsymbol{\sigma}_{i} - \Delta\boldsymbol{\sigma}_{m}\right)}{\sqrt{\sum_{i=1}^{p}\left(\Delta\boldsymbol{\sigma}_{i,est} - \Delta\boldsymbol{\sigma}_{m,est}\right)^{2}\sum_{i=1}^{p}\left(\Delta\boldsymbol{\sigma}_{i} - \Delta\boldsymbol{\sigma}_{m}\right)^{2}}} \tag{3.6}$$

where p denotes the number of pixels and p=3228 in the 2D cases; and $\Delta\boldsymbol{\sigma}_{i,est}$ and $\Delta\boldsymbol{\sigma}_{m,est}$ are the i^{th} element and mean of the reconstructed conductivity distribution, respectively; $\Delta\boldsymbol{\sigma}_{i}$ and $\Delta\boldsymbol{\sigma}_{m}$ denote respectively the i^{th} element and mean of the true conductivity distribution, which is set as one in this work.

Figure 3-13 and Figure 3-14 illustrate the TD and FD image reconstruction results of phantom 1 and phantom 2 at 10 kHz, 20 kHz, 40 kHz, 100 kHz, 200 kHz, 500 kHz and 1 MHz, by using amplitude and phase data, respectively. In FD image reconstruction procedure, 10 kHz was selected as the reference frequency, i.e., f_0 in (2.8). The voltage differences between all the test frequencies and the reference frequency were utilised to perform image reconstruction. In contrast, during the TD image reconstruction procedure, the voltage differences of each test frequency were calculated with respect to their corresponding time-referenced data, i.e., $\mathbf{V}_{t_0}$ in (2.7).

It is worth mentioning that the same colour bar was applied for all the reconstructed images in order to illustrate explicitly the effect of current frequency on the conductivity variation of a biological tissue.

In Figure 3-13 and Figure 3-14, CC is labelled for each TD amplitude image, which was calculated based on the individual colour bar of each image. CC is independent of the conductivity value and only related to its spatial distribution. Quantitative evaluation of the multi-frequency imaging of biological objects is challenging, because their conductivities are changing with frequency thus the ground truth is not known. It is even more difficult when the FD imaging method is applied. In this case, different images can be obtained when using different frequency intervals. Therefore, only the reconstruction results based on the TD imaging method were evaluated.

Figure 3-15 shows the Electrical Impedance Spectroscopy (EIS) results of the sweet potato rod and the potato rod in order to verify the multi-frequency image reconstruction results. EIS is widely used to reveal the frequency responses of bioelectrical impedance and further understand the structure, composition, physiological status or other internal properties of the biological material (Bera et al., 2016). EIS and mfEIT are based on the similar principle. However, EIS can only provide the lumped parameter such as the magnitude of bioimpedance but EIT offers spatial resolution by generating cross-sectional images of conductivity distribution. Therefore, mfEIT is more advantageous for applications requiring visualisation of the conductivity distribution.

With respect to phantom 1, the EIS result, illustrated in Figure 3-15, indicates that the conductivity of sweet potato becomes larger with the increase of frequency. The TD imaging results, shown in Figure 3-13, indicate that the inclusion area in the images becomes more evident with the increase of frequency. This is in accordance with the trend of conductivity change with respect to frequency. In addition, the transition of phase over frequency is also demonstrated in the images. The FD imaging results, shown in Figure 3-13, suggest that more explicit inclusion images can be obtained with the increase of frequency. These results are also consistent with

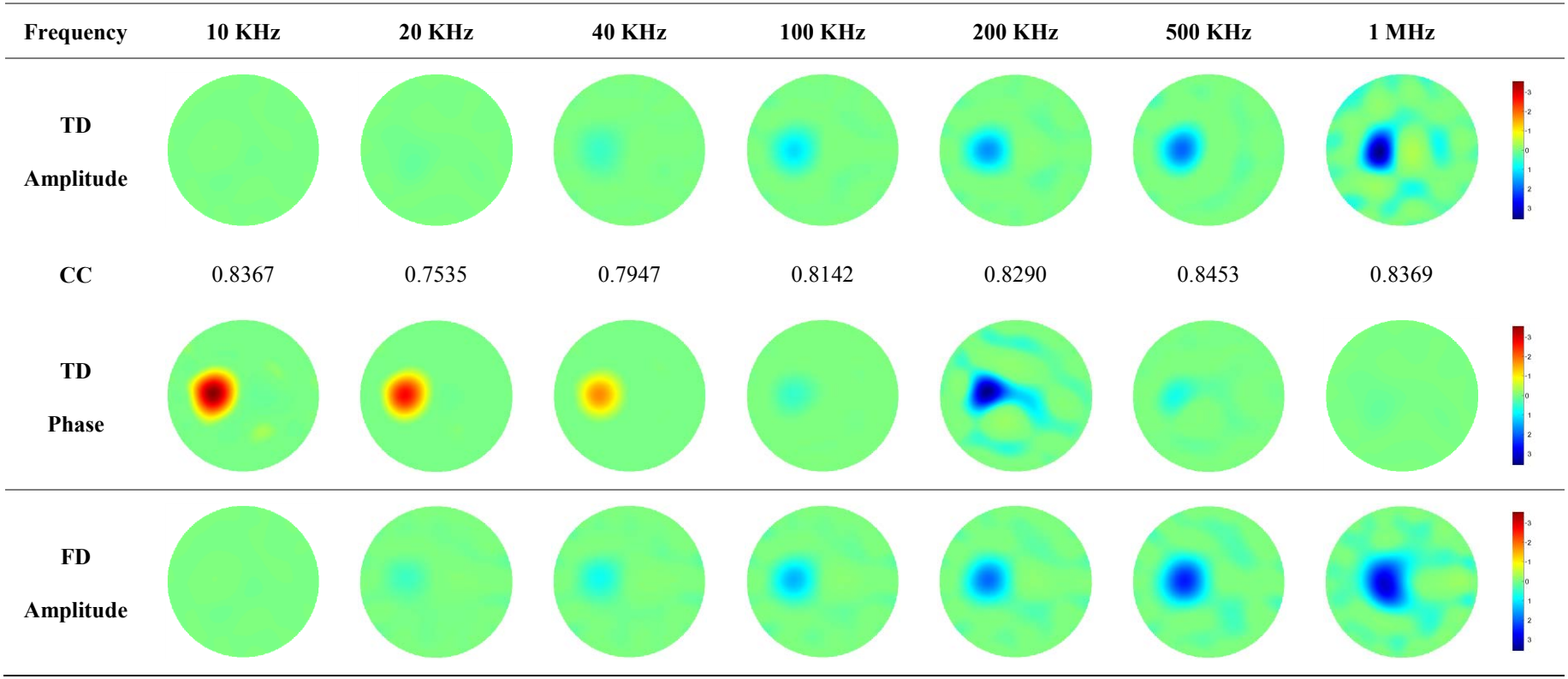

Figure 3-13 Time-difference (TD) and frequency-difference (FD) image reconstruction results of phantom 1. The first two rows show time-difference results and the third row illustrates frequency-difference results. The reference frequency of frequency-difference imaging is 10 kHz.

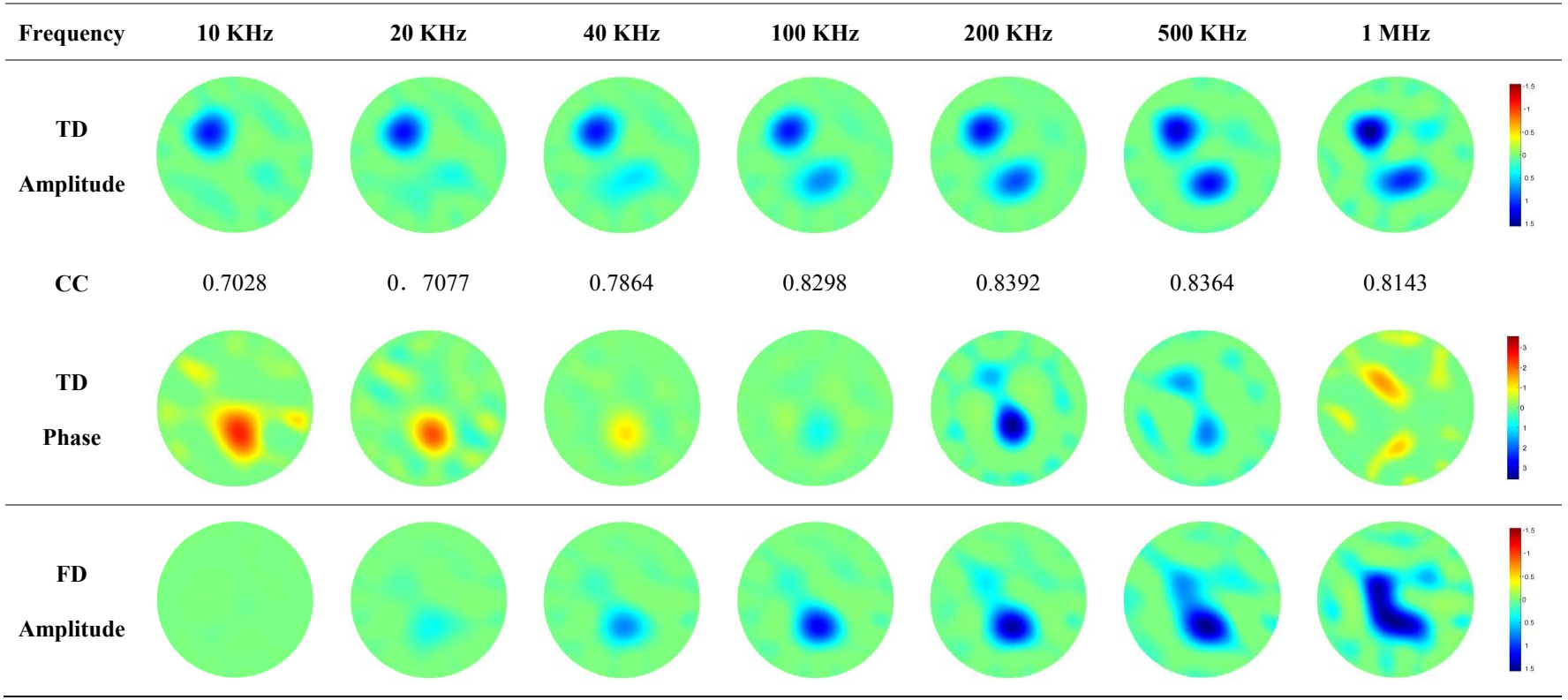

Figure 3-14 Time-difference (TD) and frequency-difference (FD) image reconstruction results of phantom 2. The first two rows show time-difference results and the third row illustrates frequency-difference results. The reference frequency of frequency-difference imaging is 10 kHz.

the fact that for sweet potato, the difference of conductivity value between the target frequency, i.e. 10 kHz, 20 kHz, …, 1 MHz, and the reference frequency, i.e. 10 kHz, increases over frequency.

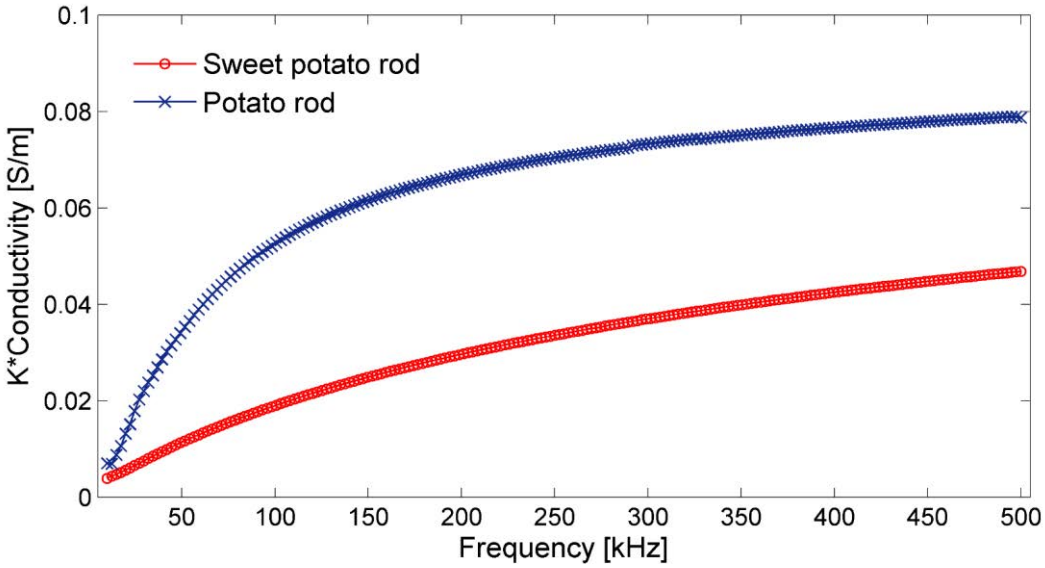

Figure 3-15 Electrical Impedance Spectroscopic (EIS) (magnitude) result of sweet potato and potato using impedance analyser (Keysight E4990A).

Figure 3-14 shows the TD and FD image reconstruction results of phantom 2, at 10 kHz, 20 kHz, 40 kHz, 100 kHz, 200 kHz, 500 kHz and 1 MHz, based on amplitude and phase data respectively. The conductivity of the metal rod does not change significantly with frequency. However, as suggested by Figure 3-15, the conductivity of the potato varies significantly with frequency. From the TD imaging results based on amplitude data, it is shown that the metal rod can been seen at all frequencies, but there is an obvious transition of the potato cylinder from weak to strong with the increase of frequency. The transition of phase with respect to frequency is also shown. Moreover, the FD results of phantom 2 show that the potato rod tends to appear from lower frequency, e.g. 20 kHz, and in contrast, the metal rod is eliminated by frequency subtraction and only tends to appear when the difference between the measurement and reference frequencies is large enough, e.g. 200 kHz. The results are also consistent with the EIS result of the potato rod.

The 2D imaging results demonstrated that the developed mfEIT system could deliver high quality 2D images within the testing frequency range, by using both TD and FD imaging methods.

3.3.3 3D TD and FD Imaging Results

A series of static 3D TD and FD imaging experiments were conducted to assess the 3D imaging ability of the mfEIT system. Figure 3-16 shows the EIT sensor employed for 3D imaging, its exact geometry model and the mesh created in COMSOL Multiphysics for forward problem calculation. The inner diameter of the sensor was 287 mm and the height of saline during the 3D experiments was 206 mm. The conductivity of the saline was 0.07 $S \cdot m^{-1}$. The 3D EIT sensor consisted of three layers of electrodes and each layer had 16 electrodes. Only the two lower layers were utilised in the following 3D experiments.

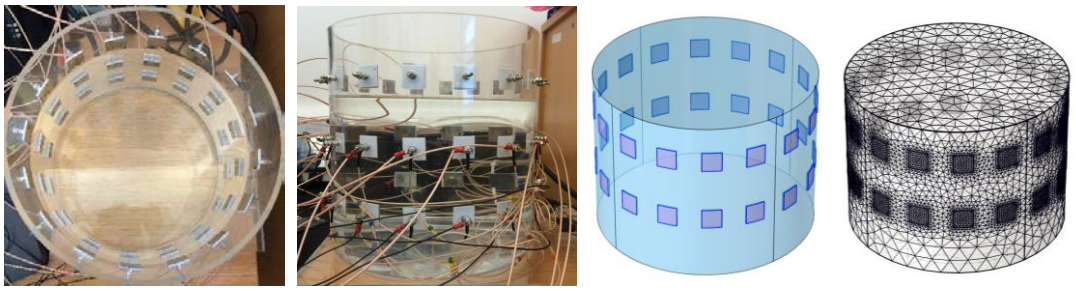

(a) (b) (c) (d)

Figure 3-16 3D EIT sensor and simulation modelling. (a) Top view. (b) Side view. (c) The 1:1 geometry model in COMSOL. (d) Mesh for forward problem calculation.

The 3D Jacobian matrix was calculated by using the combination of COMSOL Multiphysics and Matlab based on the created 1:1 sensor model as shown in Figure 3-16(c). The sensing domain was discretised into 32×32×40 voxels (32480 voxels in total within the cylindrical area). Two layers of electrodes were excited and measured separately by using the adjacent sensing strategy (Brown and Seagar, 1987). Therefore, there were 208 independent measurements in a full scan to reconstruct a frame of image.

The 3D imaging experiments of two test phantoms, i.e. a single potato and an apple with a glass cuboid, were performed. The one step Gauss-Newton solver with 3D Laplacian regularisation (Yang et al., 2014) was adopted for real-time 3D image reconstruction. In order to highlight the target objects, the conductivity values less than 50% of the maximum value (or larger than 50% of the minimum value for the negative cases) were set to be transparent. Meanwhile, scattered interpolations were applied to the original 3D images for enhanced 3D visual effect.

Figure 3-17 illustrates the single potato phantom and corresponding 3D TD image reconstruction results based on the amplitude data at 20 kHz, 40 kHz and 80 kHz. This figure also shows the 3D FD image reconstruction results by using the voltage difference data between 80 kHz and 20 kHz, and 40 kHz and 20 kHz. The potato was located near the upper layer electrodes. Both TD and FD reconstruction results were able to present the correct shape and position of the potato. As for the FD image reconstruction, 20 kHz was selected as the reference frequency and FD imaging based on frequency subtractions between 80 kHz, 40 kHz and the reference frequency also preserved the correct shape and location information of the potato.

Figure 3-18 illustrates the second test phantom, i.e. a glass cuboid and an apple with peel, and its corresponding 3D TD and FD image reconstruction results at 20 kHz, 40 kHz and 80 kHz respectively. The volume ratio of the apple and the 3D sensor was around 6.7%. By observing the TD results, it is found that the position and shape of the glass cuboid (the red and orange colour in the 3D images) could be estimated correctly. However, due to the existence of the glass cuboid, the apple (the green colour in the images) could hardly be seen, because it caused a much smaller conductivity variation in comparison with the glass cuboid. As for the FD imaging results, the glass cuboid was eliminated and only the apple was shown in the reconstructed images. This is because only the conductivity of apple changes with frequency, whilst that of the glass cuboid does not. The imaging results are consistent with the spectral bioimpedance properties of the materials.

Phantoms	Time Difference Imaging			Frequency Difference Imaging	
	20 kHz	40 kHz	80 KHz	40 kHz–20 kHz	80 kHz–20 kHz
	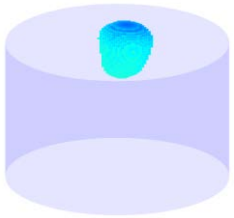 View 1	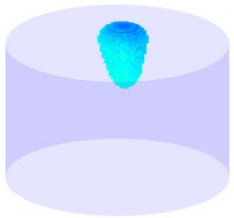 View 1	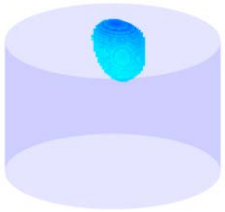 View 1	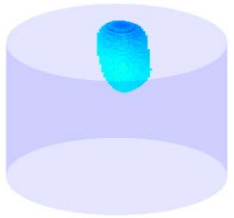 View 1	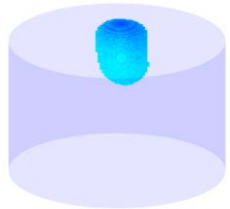 View 1
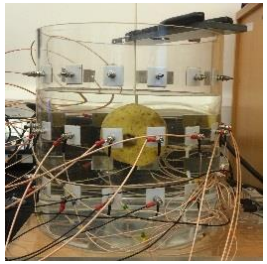	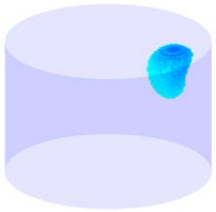 View 2	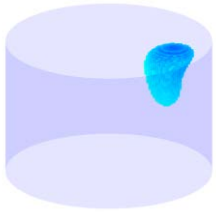 View 2	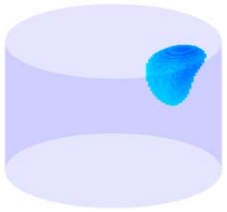 View 2	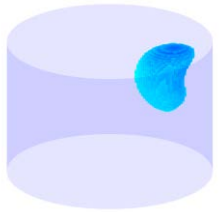 View 2	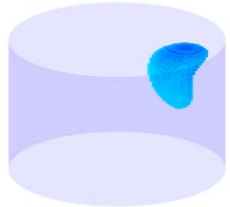 View 2
Colour bar		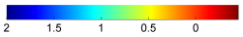	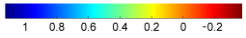		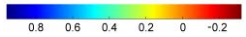

Figure 3-17 3D TD and FD image reconstruction results of a potato using amplitude data.

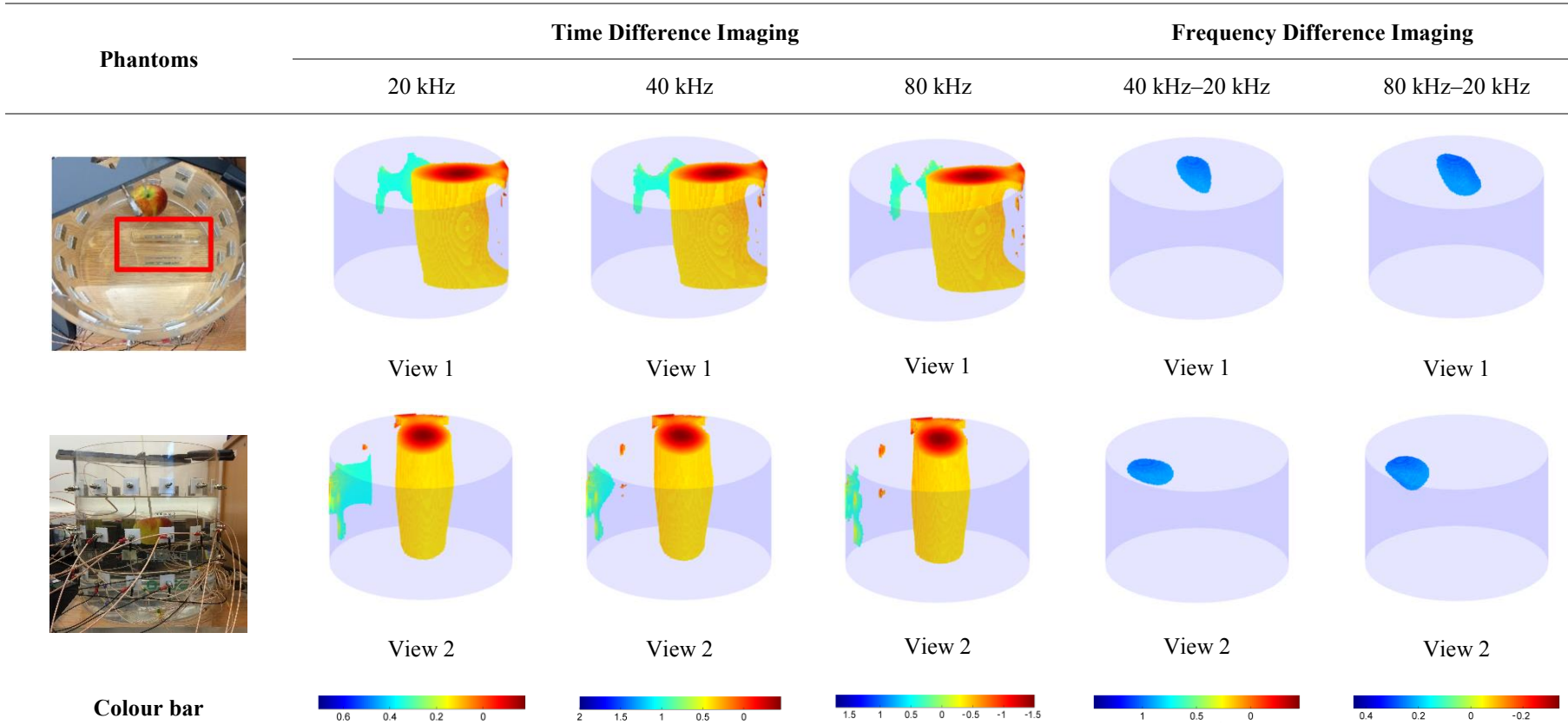

Figure 3-18 3D TD and FD image reconstruction results of a glass cuboid and an apple using amplitude data.

Supported by the 3D TD and FD imaging results in this subsection, it is confirmed that the developed mfEIT system has excellent 3D multi-frequency imaging performance.

3.4 Summary

In this chapter, a novel mfEIT system aimed for real-time 2D and 3D impedance spectroscopic imaging was developed and thoroughly evaluated in terms of resistive load capacity, frame rate, SNR, 2D and 3D multi-frequency image reconstructions. The system design was presented from the perspectives of system architecture and pivotal function modules. Compared with existing biomedical EIT systems, novel features of the proposed mfEIT system included real-time 2D and 3D multi-frequency imaging ability, flexible sensing capabilities, high SNR and high frame rate. The working frequency of the system ranged from 10 kHz to 1 MHz. The evaluation results showed that the highest SNR of the system was 82.82 dB, and the frame rate was up to 546 fps in serial mode and 1014 fps in semi-parallel mode. The developed 3D imaging software, *Visual Tomography*, could support up to 120 fps time-stacked and spatial 3D imaging in real time. In summary, the developed mfEIT system demonstrated excellent specifications and could provide advanced spectral impedance imaging for biomedical applications.

In the following chapters, practical applications of the developed mfEIT system for phantom experiments and biomedical imaging, i.e. 3D cell culture imaging and 3D cell-drug response imaging, will be presented.

Chapter 4 EIT Image Reconstruction Using Adaptive Group Sparsity Constraint

4.1 Introduction

Compared with typical industrial process applications, biomedical imaging with EIT demands a much better image quality due to the imperceptible conductivity changes in either amplitude or dimension. To deal with this challenge, a novel EIT image reconstruction algorithm using adaptive group sparsity constraint was developed to achieve high-quality conductivity imaging.

The concept of sparsity has gained popularity since the last decade with the maturity of compressive sensing theory (Baraniuk, 2007, Candes and Romberg, 2007, Candes and Wakin, 2008), which has been extensively investigated in signal processing (Berger et al., 2010), image processing (Li et al., 2011), and inverse problems including the image reconstruction problems of electrical tomography (Jin et al., 2012, Ye et al., 2015). In many biomedical applications, (absolute or difference) conductivity distribution of the sensing object is spatially sparse or sparse under certain basis, which can be regarded as *a priori* knowledge and further exploited to promote nonzero coefficients while suppressing the noise close to zeroes. In addition, adaptive mesh-grouping scheme was also proposed to enhance the spatial resolution of the electrical impedance imaging by utilising structural information (Kim et al., 2004, Lee et al., 2014, Kim et al., 2014). In this chapter, considering the combination of sparsity and underlying structural information, the idea of group sparsity (Huang and Zhang, 2010) was investigated for high-quality EIT imaging. To implement the concept, an adaptive pixel grouping method was proposed for efficient and dynamic pixel grouping for the case that the structure of conductivity distribution was not fixed or the *a priori* knowledge of the structure was unavailable. On this basis, an adaptive group sparsity constrained algorithm named AGS was further developed. Compared with the reported algorithms (Yang and Peng, 2003, Wang et al., 2004, Lionheart, 2004, Wang et al., 2007, Jin et al., 2012, Yang et al., 2014, Ye et al., 2015), the novelty of AGS includes: 1) adaptively

encoding of the structure characteristics of conductivity variation as *a priori* information and 2) integration of sparsity constraint on the group structures for superior noise reduction performance. The presented AGS method was verified by numerical simulation and phantom experiments, meanwhile its performance was compared with commonly used iterative image reconstruction algorithms.

4.2 Adaptive Group Sparsity (AGS) Constrained Method

4.2.1 Conventional Landweber Iteration, l_1 Regularisation, and Total Variation Regularisation Methods

This subsection briefly reviews prevailing iterative EIT image reconstruction algorithms, which will be used as benchmark algorithms in the following context. The first method is Landweber iteration (Yang et al., 1999), a variation of the steepest gradient descent method in optimisation theory. The updating form of Landweber iteration for EIT image reconstruction is expressed as:

$$\Delta\boldsymbol{\sigma}^{i+1} = \Delta\boldsymbol{\sigma}^{i} - \alpha\mathbf{J}^{\mathrm{T}}(\mathbf{J}\Delta\boldsymbol{\sigma}^{i} - \Delta\mathbf{V}) \tag{4.1}$$

where α is the step factor of each iteration, which is a positive scaler.

The second method is l_1 regularisation whose detail can be referred to (2.16) (see Chapter 2). In this chapter, l_1 regularisation is solved based on the basis pursuit method (van den Berg and Friedlander, 2008).

Another iterative algorithm is TV regularisation, which is described from (2.17) to (2.20) (see Chapter 2). In this context, TV regularisation is solved by the gradient-based recovery method, whose iteration form is given by:

$$\Delta\boldsymbol{\sigma}_{x,y}^{i+1} = \Delta\boldsymbol{\sigma}_{x,y}^{i} - \alpha\left\{\nabla_{x,y}\left(\frac{1}{2}\left\|\Delta\mathbf{V} - \mathbf{J}\Delta\boldsymbol{\sigma}^{i}\right\|_2^2\right) + \nabla_{x,y}\left(\left\|\Delta\boldsymbol{\sigma}^{i}\right\|_{\mathrm{TV}}\right)\right\} \tag{4.2}$$

where α denotes the step factor of each iteration. As expressed by (4.3), the gradient of TV norm is calculated based on a smooth approximation strategy to avoid a zero denominator.

$$\nabla_{x,y}(\|\Delta\boldsymbol{\sigma}\|_{\mathrm{TV}}) = \frac{D^{h}_{x,y}(\Delta\boldsymbol{\sigma}) + D^{v}_{x,y}(\Delta\boldsymbol{\sigma})}{\sqrt{(\mathrm{D}^{v}_{x,y}(\Delta\boldsymbol{\sigma}))^2 + (\mathrm{D}^{h}_{x,y}(\Delta\boldsymbol{\sigma}))^2 + \varepsilon}} - \frac{D^{h}_{x-1,y}(\Delta\boldsymbol{\sigma})}{\sqrt{(\mathrm{D}^{v}_{x-1,y}(\Delta\boldsymbol{\sigma}))^2 + (\mathrm{D}^{h}_{x-1,y}(\Delta\boldsymbol{\sigma}))^2 + \varepsilon}} - \frac{D^{v}_{x,y-1}(\Delta\boldsymbol{\sigma})}{\sqrt{(\mathrm{D}^{v}_{x,y-1}(\Delta\boldsymbol{\sigma}))^2 + (\mathrm{D}^{h}_{x,y-1}(\Delta\boldsymbol{\sigma}))^2 + \varepsilon}} \tag{4.3}$$

where ε is a relaxation parameter. Note that ε was empirically selected as 1e-7 in this work according to a series of practice. If the relaxation parameter is too large, the approximation will incur significant errors. The chosen value was small enough to ensure approximation accuracy, and meanwhile, guarantee the denominator was not zero under any circumstance.

4.2.2 The Proposed AGS Algorithm

Conventional l_1 regularisation described by (2.16) (see Chapter 2) only makes use of the sparsity of conductivity as *a priori* knowledge (Grasmair et al., 2008), i.e., either the conductivity itself, or its transform under certain basis, or its gradient, is sparse. This work further incorporates the underlying structure of conductivity variation as additional information, which extends the scope of sparsity. The conductivity variation of most EIT applications contains group sparsity structure, since it more likely groups together rather than individually distributes with respect to the homogenous background. On this occasion, the combined sparsity and structure characteristics can be applied to reduce the degree of freedom of the EIT image reconstruction problem and consequently improve recoverability.

Figure 4-1(a) illustrates the quadrate pixel mesh to solve the EIT image reconstruction problem. The sensing domain (red colour area) is discretised by 64×64 pixels and 3228 pixels are enclosed in the circular area. To implement combined constraint of sparsity and structure prior, discretised pixels within the sensing domain should be grouped together according to the characteristics of conductivity variation. An intuitive pixel-grouping method is to group the pixels

using a moving window with regular geometrical shapes, such as the quadrate shape. Figure 4-1(b) shows an example based on this idea with a total group number N=16. Apparently, such grouping methods are not optimal in practical cases, as the conductivity variation is more complicated and unpredictable.

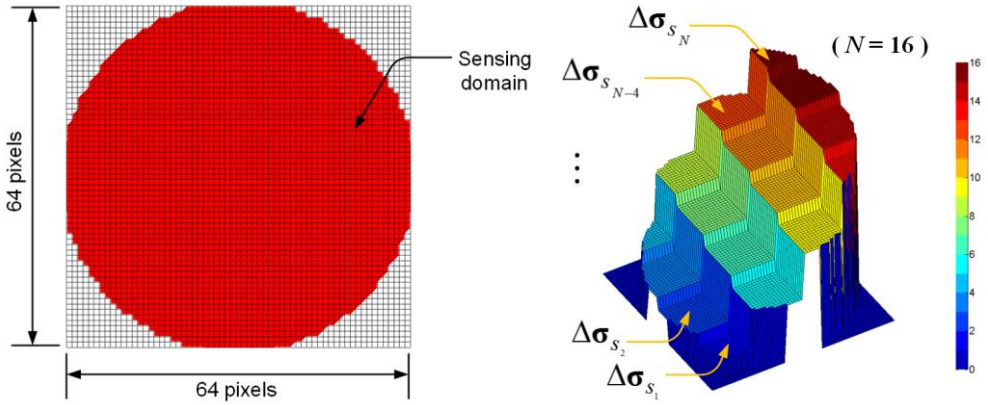

(a) (b)

Figure 4-1 Schematic illustration of pixel grouping. (a) The mesh for image reconstruction. (b) A grouping example with 16 quadrate shape groups.

Given that the conductivity variation vector $\Delta\boldsymbol{\sigma}$ can be divided into N disjoint groups according to some criteria, i.e.:

$$\Delta\boldsymbol{\sigma} = \{\Delta\boldsymbol{\sigma}_{\mathbf{s}_1}, \Delta\boldsymbol{\sigma}_{\mathbf{s}_2}, ..., \Delta\boldsymbol{\sigma}_{\mathbf{s}_N}\} \tag{4.4}$$

and meanwhile

$$\mathrm{U}_{i=1}^{N}\Delta\boldsymbol{\sigma}_{\mathbf{s}_i} = \Delta\boldsymbol{\sigma} \tag{4.5}$$

where $\mathbf{S}_i$ is the group index vector of the i^{th} group. Equation (4.5) guarantees the complete cover. To incorporate the group sparsity prior, EIT image reconstruction problem depicted by (2.9) (see Chapter 2) can be formulated using the weighted group sparse basis pursuit model with non-negative constraint as stated by:

$$\begin{cases} \min\limits_{\Delta\boldsymbol{\sigma}} & \|\Delta\boldsymbol{\sigma}\|_{w,2,1} := \sum\limits_{i=1}^{N} w_i \left\|\Delta\boldsymbol{\sigma}_{\mathbf{s}_i}\right\|_2 \\ s.t. & \mathbf{J}\Delta\boldsymbol{\sigma}=\Delta\mathbf{V}, \\ & g(\Delta\boldsymbol{\sigma})\cdot\Delta\boldsymbol{\sigma} \geq 0 \end{cases} \tag{4.6}$$

where $\|\Delta\boldsymbol{\sigma}\|_{w,2,1}$ is the weighted $l_{2,1}$ norm, which has been proven to promote group sparsity and generate a convex problem (Huang and Zhang, 2010); w_i denotes the weight for the i^{th} group. To further improve the noise reduction performance, a non-negative constraint is applied on each element of the dot multiplication $g(\Delta\boldsymbol{\sigma})\cdot\Delta\boldsymbol{\sigma}$, where the operator g is defined by:

$$g(\Delta\boldsymbol{\sigma}) = [sign(sum(\Delta\boldsymbol{\sigma}_{\mathbf{s}_1}))\cdot\mathbf{H}_{\mathbf{s}_1}, \ldots sign(sum(\Delta\boldsymbol{\sigma}_{\mathbf{s}_i}))\cdot\mathbf{H}_{\mathbf{s}_i}, \ldots]^{\mathrm{T}} \tag{4.7}$$

where *sign* denotes the sign function; *sum* denotes the summation of a vector; $\mathbf{H}_{\mathbf{s}_i}$=[1, 1, …, 1] is the all one vector which dimension equals to the pixel numbers enclosed in the i^{th} group $\mathbf{S}_i$.

A key challenge of solving the optimisation problem depicted in (4.6) is prompt and reasonable grouping of conductivity variation based on the measured data, especially when there is no *a priori* information available to predict the underlying structure of the conductivity variation. For this goal, an adaptive pixel grouping approach incorporating with (4.6) was proposed to tackle this problem. The basic idea is to group together the pixels which present similar conductivity variation amplitude and meanwhile locate within a reasonable neighbourhood of each inclusion.

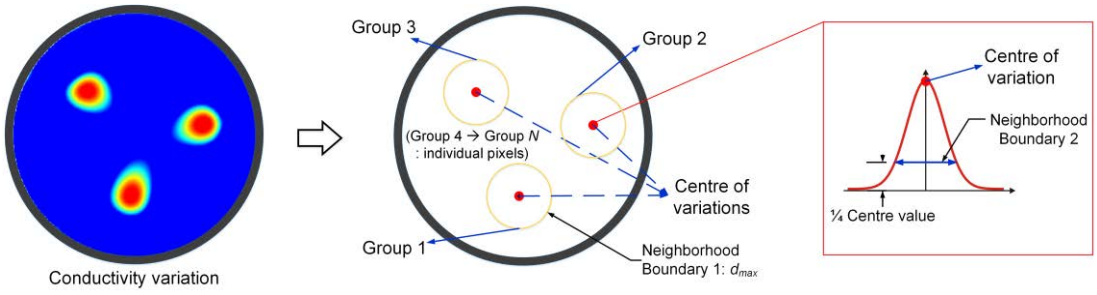

Figure 4-2 Schematic illustration of the adaptive pixel grouping idea.

Figure 4-2 shows the schematic illustration of the proposed adaptive pixel grouping method. First of all, the conductivity variation is estimated by the one-step Gauss-Newton solver with Laplacian regularisation (Yang et al., 2014), which is described by (2.13) and (2.14) in Chapter 2. There are two reasons to adopt this

method in this work: 1) the estimation of conductivity variation generated from this method is good enough for pixel grouping; 2) the computation cost of this method is relatively low which facilitates its real-time implementation.

After obtaining the estimation of conductivity variation, the geometric centre of individual inclusions can be identified by calculating local maximum points of the estimation, as indicated by the red points shown in the middle of Figure 4-2. Then a number of large pixel groups around each geometric centre can be formed while the remaining pixels are regarded as a number of small groups per individual pixel. Consequently, this idea will generate a number of large groups according to the number of inclusions, whilst the other individual pixels will not be grouped but counted as small groups per pixel.

Regarding the large pixel groups, two criteria are applied to determine the boundary of each group, which are demonstrated as follows:

Criterion 1: The first criterion empirically illustrates the boundary of the neighbourhood of each inclusion, i.e., boundary 1 as shown in the middle of Figure 4-2. It determines the outermost border of each large pixel group, in order to include the pixels within a reasonable geometrical region. The objective is to avoid the unreasonable situation that two pixels with a large distance are grouped together. Boundary 1 is determined by the geometric centre and the maximum diameter d_{max} as the yellow circles shown in the middle part of Figure 4-2.

Criterion 2: The second criterion provides a finer boundary of each group inside the outermost border defined by the first criterion, i.e., boundary 2 as shown in the right part of Figure 4-2. Boundary 2 is determined by the pixels having a conductivity variation which is a quarter of the conductivity variation at the centre of each inclusion, as shown in the red box on the right of Figure 4-2. That is, the pixels having conductivity variations larger than a quarter of the maximum value at the centre of each inclusion are regarded to be within boundary 2.

The final pixel grouping set is then calculated as the intersection of the two regions defined by boundary 1 and boundary 2 respectively. It is worth mentioning

that the value of $d_{\max}$ is not critical and it can be determined empirically according to specific applications. Basically, there are two methods to find an appropriate value for $d_{\max}$. The first is that if the *a priori* information of the rough geometry dimension is accessible, the value of $d_{\max}$ can be set accordingly. Second, in case the *a priori* information of the geometry dimension of the inclusions is unknown, the one step image reconstruction algorithm described by (2.14) (see Chapter 2) can be applied first and an appropriate value of $d_{\max}$ can be determined thereafter. The function of $d_{\max}$ is to avoid any misclassification of two pixels which satisfy ***Criterion 2*** but are geometrically far away from each other. In this context, d_{max} is fixed as 20 pixels to deal with conductivity variation in a small dimension.

As the pixel grouping result is calculated based on the one-step estimation, it may change slightly when the SNR of voltage measurement decreases. However, AGS does not necessarily need a precise estimation of the inclusion boundary. Instead, it only requires the inclusion is completely contained in the group. As a result, with a reasonable SNR such as 50 dB or higher (which can be achieved by most of the reported EIT systems (see Table 2-1, Chapter 2)), ***Criterion 2*** can generate a stable enough group boundary. By this means, pixel groups closely associated with the underlying structure of conductivity variation can be adaptively calculated and the group sparsity prior can be effectively integrated by using (4.6). Finally, the EIT image reconstruction problem can be solved by using the modified group-sparse basis pursuit model illustrated in (4.6). The algorithm is named as adaptive group sparsity (AGS) constrained algorithm. The detailed implementation of AGS is illustrated in Table 4-1.

In Table 4-1, adaptive pixel grouping result is firstly calculated through Step 1 to Step 5. The grouping result is denoted by a group index vector **G** whose length is the same as the total number of pixels. In Step 2, the absolute value of the estimated conductivity variation from Step 1 is adopted in order to deal with the situation either with positive or negative or bi-direction conductivity variations. Then in Step 3, the absolute conductivity variation is filtered using a threshold defined by the summary of its mean and standard deviation. The filter is applied to eliminate the noise that may affect the calculation of local maximum points in Step 4. Furthermore,

Table 4-1 Adaptive Group Sparsity Constrained Algorithm.

Algorithm 4-1: Adaptive group sparsity (AGS) constrained algorithm

Input: Measured voltage vector $\Delta\mathbf{V}$, maximum group diameter d_{max}, and weighting vector $\mathbf{w}$.

Step 1: Estimate the conductivity variation by the one-step Gauss-Newton solver with Laplacian regularization as formulated by (2.14).

Step 2: Calculate the mean $|\Delta\hat{\boldsymbol{\sigma}}|_{mean}$ and standard deviation $|\Delta\hat{\boldsymbol{\sigma}}|_{std}$ of the absolute value of the estimated conductivity variation $\Delta\hat{\boldsymbol{\sigma}}$ from step 1.

Step 3: Apply the filter defined as following:

$$\begin{cases} |\Delta\hat{\boldsymbol{\sigma}}|_i = |\Delta\hat{\boldsymbol{\sigma}}|_i, & if\ |\Delta\hat{\boldsymbol{\sigma}}|_i > |\Delta\hat{\boldsymbol{\sigma}}|_{mean} + |\Delta\hat{\boldsymbol{\sigma}}|_{std} \\ |\Delta\hat{\boldsymbol{\sigma}}|_i = 0, & if\ |\Delta\hat{\boldsymbol{\sigma}}|_i \le |\Delta\hat{\boldsymbol{\sigma}}|_{mean} + |\Delta\hat{\boldsymbol{\sigma}}|_{std} \end{cases}, i = 1,...,3228$$

Step 4: Calculate the index vector **D** of all local maximum points of the output from step 3.

Step 5: Calculate the group index vector **G**:

for i=1: *number of local maximum points* **do**

  for j=1:*total pixel number* **do**

    if $|\Delta\hat{\boldsymbol{\sigma}}|_j > \frac{1}{4}|\Delta\hat{\boldsymbol{\sigma}}|_{\mathbf{D}(i)}$ and $\|\mathbf{C}_j - \mathbf{C}_{\mathbf{D}(i)}\|^2 < (\frac{d_{\max}}{2})^2$

      G(j)=i

(**C** is the coordinate vector of pixels)

k=1

for $t \in$ all other elements in **G** **do**

  G($t(k)$)= *number of local maximum points*+k

  k=k+1

Step 6: Solve the group-sparse basis pursuit model illustrated in (4.6).

Output: The estimated conductivity variation.

all of the local maximum points, which denote the centres of large groups, are identified, while in Step 5, pixels belong to the same large group are classified by the aforementioned two criteria and given the same group index value in **G**. At the end,

in Step 6, group index vector **G** representing the pixel grouping result is integrated into (4.6) to estimate iteratively the conductivity variation utilising the group sparsity prior.

The alternating direction method of multipliers (ADMM) (Fukushima, 1992, Deng et al., 2013) was adopted to solve (4.6). ADMM is a method to solve convex optimisation problems by dividing them into easier sub-problems (Fukushima, 1992). Generally, ADMM is targeted to solve a type of optimisation problems with the following form:

$$\begin{cases} \min\limits_{\mathbf{x},\,\mathbf{z}} & f(\mathbf{x}) + h(\mathbf{z}) \\ s.t. & \mathbf{A}\mathbf{x} + \mathbf{B}\mathbf{z} = \mathbf{E} \end{cases} \tag{4.8}$$

By introducing an auxiliary variable **z**, (4.6) can be firstly rewritten as the following equivalent form:

$$\begin{cases} \min\limits_{\Delta\boldsymbol{\sigma},\,\mathbf{z}} & \|\mathbf{z}\|_{w,2,1} := \sum\limits_{i=1}^{N} w_i \left\| \mathbf{z}_{\mathbf{s}_i} \right\|_2 \\ s.t. & \mathbf{z} = \Delta\boldsymbol{\sigma},\ \mathbf{J}\Delta\boldsymbol{\sigma} = \Delta\mathbf{V}, \\ & g(\Delta\boldsymbol{\sigma}) \cdot \Delta\boldsymbol{\sigma} \geq 0 \end{cases} \tag{4.9}$$

where (4.9) can be further rewritten as an unconstrained form based on the principle of augmented Lagrangian problem without considering the non-negativity constraint, which is stated by:

$$\begin{aligned} \min_{\Delta\boldsymbol{\sigma},\,\mathbf{z}} \quad & \sum_{i=1}^{N} w_i \left\| \mathbf{z}_{\mathbf{s}_i} \right\|_2 - \boldsymbol{\mu}_1^{\mathrm{T}}(\mathbf{z} - \Delta\boldsymbol{\sigma}) + \frac{\eta_1}{2} \| \mathbf{z} - \Delta\boldsymbol{\sigma} \|_2^2 - \ldots \\ & \boldsymbol{\mu}_2^{\mathrm{T}}(\mathbf{J}\Delta\boldsymbol{\sigma} - \Delta\mathbf{V}) + \frac{\eta_2}{2} \| \mathbf{J}\Delta\boldsymbol{\sigma} - \Delta\mathbf{V} \|_2^2 \end{aligned} \tag{4.10}$$

where $\boldsymbol{\mu}_1$ and $\boldsymbol{\mu}_2$ are multipliers and η_1 and η_2 are penalty parameters. Equation (4.9) without considering the non-negativity constraint has been proved to converge to the solution of (4.10) (Fukushima, 1992), and (4.10) with non-negativity constraint can

Table 4-2 ADMM for The Minimisation Problem in (4.10) with Non-negativity Constraint.

Initialization: Starting point ($\mathbf{z}$, $\Delta\boldsymbol{\sigma}$, $\boldsymbol{\mu}_1$, $\boldsymbol{\mu}_2$, η_1, η_2, α_1, α_2)

iteration:

a) solve the Δσ-subproblem:

$$\Delta\boldsymbol{\sigma}_{k+1} = \arg\min_{\Delta\boldsymbol{\sigma}} \ \boldsymbol{\mu}_1^{\mathrm{T}}\Delta\boldsymbol{\sigma}_k + \frac{\eta_1}{2}\| \mathbf{z} - \Delta\boldsymbol{\sigma}_k \|_2^2 - \boldsymbol{\mu}_2^{\mathrm{T}}\mathbf{J}\Delta\boldsymbol{\sigma}_k + \frac{\eta_2}{2}\| \mathbf{J}\Delta\boldsymbol{\sigma}_k - \Delta\mathbf{V} \|_2^2$$

b) solve the z-subproblem:

$$\mathbf{z}_{k+1} = \arg\min_{\mathbf{z}} \ \sum_{i=1}^{N} w_i \left\| \mathbf{z}_{\mathbf{s}_i} \right\|_2 - \boldsymbol{\mu}_1^{\mathrm{T}}\mathbf{z} + \frac{\eta_1}{2}\| \mathbf{z} - \Delta\boldsymbol{\sigma} \|_2^2$$

c) apply the non-negative constraint $g(\Delta\boldsymbol{\sigma})\cdot\Delta\boldsymbol{\sigma} \geq 0$

d) update the multipliers:

$$\boldsymbol{\mu}_1 = \boldsymbol{\mu}_1 - \alpha_1\eta_1(\mathbf{z} - \Delta\boldsymbol{\sigma})$$

$$\boldsymbol{\mu}_2 = \boldsymbol{\mu}_2 - \alpha_2\eta_2(\mathbf{J}\Delta\boldsymbol{\sigma} - \Delta\mathbf{V})$$

until a stopping criterion is satisfied.

be tackled using the ADMM algorithm demonstrated in Table 4-2. Note that the non-negativity constraint in (4.9) is imposed by step c) in Table 4-2.

By applying ADMM, (4.10) can be divided into two subproblems, i.e., the $\Delta\boldsymbol{\sigma}$-subproblem and the $\mathbf{z}$-subproblem. The $\Delta\boldsymbol{\sigma}$-subproblem as depicted in step a) in Table 4-2 is a convex quadratic problem which can be directly solved in one step by calculating its gradient, which is expressed as:

$$\Delta\boldsymbol{\sigma}_{k+1} = (\eta_1\mathbf{I} + \eta_2\mathbf{J}^{\mathrm{T}}\mathbf{J})^{-1}(\eta_1\mathbf{z} - \boldsymbol{\mu}_1 + \mathbf{J}^{\mathrm{T}}(\eta_2\Delta\boldsymbol{\sigma}_k + \boldsymbol{\mu}_2)) \tag{4.11}$$

The $\mathbf{z}$-subproblem as demonstrated in step b) can be rewritten as:

$$\begin{aligned}\mathbf{z}_{k+1} &= \arg\min_{\mathbf{z}} \sum_{i=1}^{N} (w_i \left\| \mathbf{z}_{\mathbf{s}_i} \right\|_2 - \boldsymbol{\mu}_1^{\mathrm{T}} \mathbf{z}_{\mathbf{s}_i} + \frac{\eta_1}{2} \| \mathbf{z}_{\mathbf{s}_i} - \Delta\boldsymbol{\sigma}_{\mathbf{s}_i} \|_2^2) \\ &= \arg\min_{\mathbf{z}} \sum_{i=1}^{N} (w_i \left\| \mathbf{z}_{\mathbf{s}_i} \right\|_2 + \frac{\eta_1}{2} \| \mathbf{z}_{\mathbf{s}_i} - \Delta\boldsymbol{\sigma}_{\mathbf{s}_i} - \frac{1}{\eta_1} \boldsymbol{\mu}_{\mathbf{s}_i} \|_2^2 + \mathrm{M}(\Delta\boldsymbol{\sigma}_{\mathbf{s}_i})) \end{aligned} \tag{4.12}$$

where $\mathrm{M}(\Delta\boldsymbol{\sigma}_{\mathbf{s}_i})$ is a function of $\Delta\boldsymbol{\sigma}_{\mathbf{s}_i}$ which has no effect on the result therefore can be regarded as a constant in the **z**-subproblem. Equation (4.12) has a closed form solution by applying the group-wise soft thresholding (Donoho, 1995), which is given by:

$$\mathbf{z}_{\mathbf{s}_i} = \max\left\{ \left\| \Delta\boldsymbol{\sigma}_{\mathbf{s}_i} + \frac{1}{\eta_1} (\boldsymbol{\mu}_1)_{\mathbf{s}_i} \right\|_2 - \frac{w_i}{\eta_1}, 0 \right\} \frac{\Delta\boldsymbol{\sigma}_{\mathbf{s}_i} + \frac{1}{\eta_1} (\boldsymbol{\mu}_1)_{\mathbf{s}_i}}{\left\| \Delta\boldsymbol{\sigma}_{\mathbf{s}_i} + \frac{1}{\eta_1} (\boldsymbol{\mu}_1)_{\mathbf{s}_i} \right\|_2} \tag{4.13}$$

In AGS, appropriate weight w_i chosen based on *a priori* knowledge may improve its recovery performance. For the simplest case, w_i=1 can be applied to treat each group equally, i.e.:

$$w_i = 1, \quad i = 1, ..., N \tag{4.14}$$

Alternatively, a smaller weight can be given to the large groups while a larger one to the other small groups to promote the sparsity of the estimation for large groups. In this case, the weight can be calculated by:

$$\begin{cases} w_i = \dfrac{1}{N_b + 2N_s} & \text{if the } i^{th} \text{ group is large,} \\ w_i = \dfrac{2}{N_b + 2N_s} & \text{if the } i^{th} \text{ group is small,} \\ N_b + N_s = N \end{cases} \tag{4.15}$$

where N_b is the number of large groups and N_s is the number of small groups; N is the total number of groups. Equation (4.15) shows a weighting example where the

weight of large group is half of that of the small group under the assumption that the summation of all weights is one. The influence of weight on image quality is further discussed in the following section.

Finally, several remarks of the AGS method are summarised as follows:

1) A group index vector with the same length as the total pixel number is defined to denote the adaptive pixel grouping result.
2) Pixels belonging to the same group have the same group index value.
3) The pixel group containing more than one pixel is defined as a large group in the following sections.
4) The pixel group containing only one pixel is defined as a small group in the following sections.
5) The pixel groups may overlap.
6) The pixel grouping method guarantees complete cover.

4.3 Results and Discussion

4.3.1 Numerical Simulation

The AGS method was comprehensively evaluated in this subsection by numerical simulation of a series of phantoms. The performance of AGS was compared with that of the conventional Landweber iteration (4.1), l_1 regularisation (2.16) (see Chapter 2), and TV regularisation algorithms (2.17) (see Chapter 2), which have been popularly applied in image reconstruction and denoise problems.

As illustrated in Figure 4-3(a), a 16-electrode EIT sensor was modelled in COMSOL Multiphysics for numerical evaluation of the AGS method. The inner diameter of the sensor was 95 mm. The background substance was saline with a conductivity value of 0.05 $S \cdot m^{-1}$. Four conductivity variation phantoms, i.e., phantom 1 to phantom 4, were established, as shown from Figure 4-3(b) to Figure 4-3(e), respectively. Phantom 1 simulates a large air bubble (non-conductive) with an object-sensor diameter ratio of 20%. Phantom 2 simulates five dispersed small air

bubbles with two different object-sensor diameter ratios, i.e., 4% (left top bubbles) and 5% (right below bubbles). Phantom 3 simulates three objects with an object-sensor diameter ratio of 10% but different conductivities, i.e., 0.03 $S \cdot m^{-1}$ of the left object, 0.01 $S \cdot m^{-1}$ of the right object and 1e+7 $S \cdot m^{-1}$ of the bottom object. Phantom 4 simulates two conductive objects (1e+7 $S \cdot m^{-1}$) with an object-sensor diameter ratio larger than 10% and different shapes.

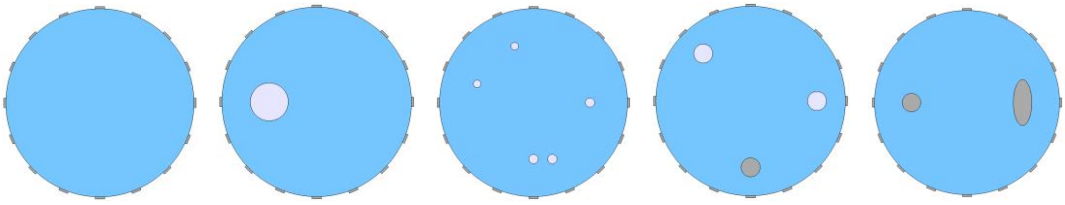

Figure 4-3 Modelled EIT sensor and simulation phantoms. (a) The 16-electrode EIT sensor. (b) Phantom 1. (c) Phantom 2. (d) Phantom 3. (e) Phantom 4.

Adjacent sensing strategy was adopted in simulation to obtain the boundary voltage data (Brown and Seagar, 1987). Using this strategy, a completed data frame is composed of 104 independent measurements. White noise was then added to the simulation data to obtain 50 dB SNR. When implementing the Landweber iteration, l_1 regularisation, TV regularisation and AGS algorithm, the maximum iteration number was set as 500 and the stopping tolerance was selected to be 1e-7. The iteration would stop if either condition was firstly met. The algorithm parameters, such as step factors and weights were empirically determined based on a series of practices and the same parameters were applied to all the test phantoms, which can be explicitly found in the first row of Table 4-3.

To evaluate quantitatively the accuracy of the reconstructed images, relative image error (IE) and correlation coefficient (CC) between the normalised conductivity variation and the true phantom were employed. The definition of IE and CC is expressed as:

$$\mathrm{IE} = \frac{\left\| \Delta\boldsymbol{\sigma} - \Delta\boldsymbol{\sigma}_{true} \right\|}{\left\| \Delta\boldsymbol{\sigma}_{true} \right\|} \tag{4.16}$$

$$\mathrm{CC} = \frac{\sum_{i=1}^{p}\left(\Delta\boldsymbol{\sigma}_i - \Delta\boldsymbol{\sigma}_{avr}\right)\left(\Delta\boldsymbol{\sigma}_{true,i} - \Delta\boldsymbol{\sigma}_{true,avr}\right)}{\sqrt{\sum_{i=1}^{p}\left(\Delta\boldsymbol{\sigma}_i - \Delta\boldsymbol{\sigma}_{avr}\right)^2 \sum_{i=1}^{p}\left(\Delta\boldsymbol{\sigma}_{true,i} - \Delta\boldsymbol{\sigma}_{true,avr}\right)^2}} \tag{4.17}$$

where $\Delta\boldsymbol{\sigma}$ and $\Delta\boldsymbol{\sigma}_{true}$ are the reconstructed conductivity variation and true conductivity variation, respectively; p is the number of pixels and in this work p=3228; $\Delta\boldsymbol{\sigma}_i$ and $\Delta\boldsymbol{\sigma}_{avr}$ are the i^{th} element and the average of the reconstructed conductivity variation, respectively; $\Delta\boldsymbol{\sigma}_{true,i}$ and $\Delta\boldsymbol{\sigma}_{true,avr}$ are the i^{th} element and the average of the true conductivity variation, respectively.

Table 4-3 also provides the image reconstruction results of the test phantoms and their IE and CC values, based on the Landweber iteration, TV regularisation, l_1 regularisation and AGS algorithm. The pixel grouping result of each phantom is shown in Table 4-4, where the large groups are highlighted using different colours and the small groups are represented by the same light green colour.

Phantom 1 was designed to evaluate the reconstruction performance of large objects. Compared with Landweber iteration, TV regularisation and l_1 regularisation, the reconstructed image based on AGS demonstrates significantly improved noise reduction performance as well as more accurate position and shape of the target object. In addition, the result using AGS has a much smaller image error, i.e., 47.47%, and higher correlation coefficient, i.e., 0.9192, in comparison with the results using other algorithms. Note that for the large object, l_1 regularisation provides an estimation with a too small size.

Phantom 2 evaluated the reconstruction performance of multiple small objects with slightly different sizes and close locations. The two spheres located near the bottom are close to each other. The pixel grouping result in Table 4-4 shows that the two spheres near the bottom are clustered into a big pixel group due to the low spatial resolution of the estimation in step 1, Table 4-1. However, in this case, group sparsity structure still stands and the AGS method could further distinguish these two objects after several iterations, whilst the other algorithms fail to achieve the same performance.

Table 4-3 Image Reconstruction Results Based on Noisy Simulation Data (SNR=50 dB).

Phantom	**Landweber** Step factor α in Eq.(4.1): 2	**l_1** Step factor in Eq. (2.16): 2	**TV** Step factor α in Eq. (4.2): 2	**AGS** d_{max}: 20; **w**: Eq. (4.15), λ: 0.01
	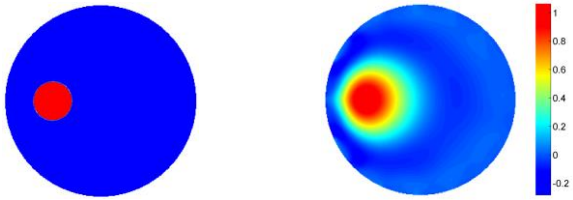	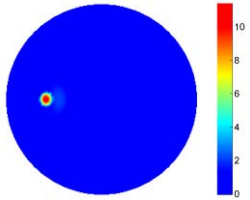	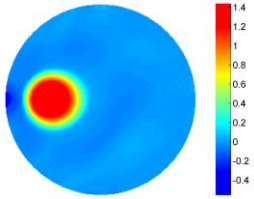	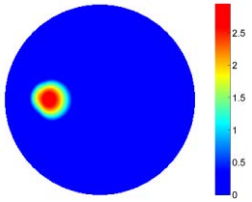
IE [%]	87.87	85.64	64.13	47.47
CC	0.6840	0.6238	0.8212	0.9192
	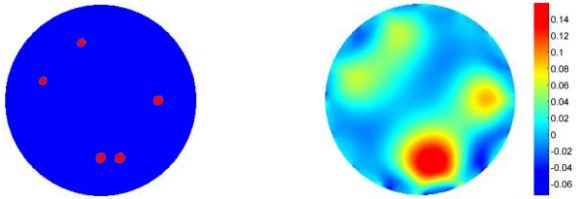	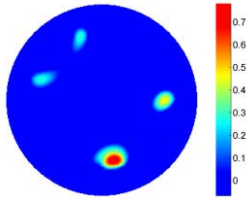	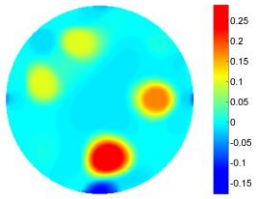	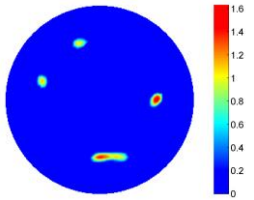
IE [%]	244.6	100.1	202.8	64.88
CC	0.2374	0.4567	0.3108	0.7621
	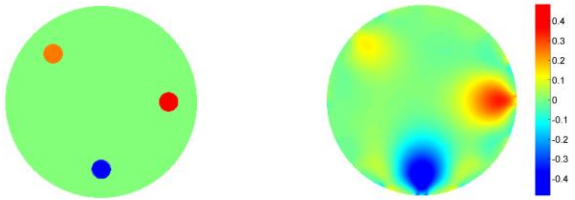	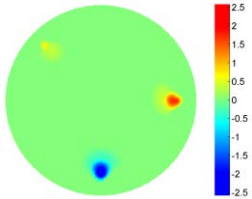	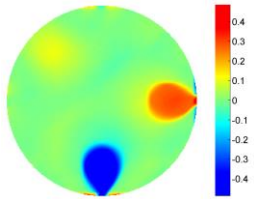	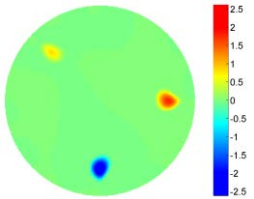

IE [%]	177.6	61.16	154.7	42.21
CC	0.4769	0.7940	0.4562	0.9098
	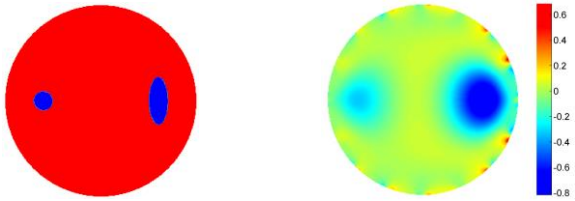			
IE [%]	126.4	97.70	85.07	64.59
CC	0.5351	0.7346	0.6586	0.8092

Table 4-4 Pixel Grouping Result of Each Phantom.

Phantom 1	**Phantom 2**	**Phantom 3**	**Phantom 4**
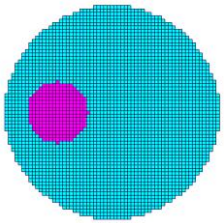	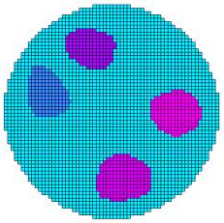	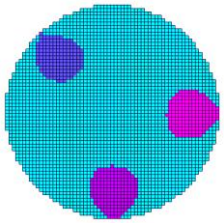	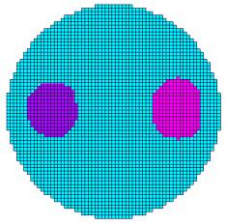
Large group number: 1 Small group number: 2977	Large group number: 4 Small group number: 2601	Large group number: 3 Small group number: 2725	Large group number: 2 Small group number: 2817

Phantom 3 tested the performance of imaging objects with three different conductivity values and phantom 4 validated the performance of imaging objects with different geometry shapes. For all the test phantoms, the AGS algorithm demonstrated superior image quality, by using which more accurate object shapes and locations were demonstrated; image errors were significantly decreased (below 65%) and correlation coefficients were increased (above 0.7621), in comparison with other iterative algorithms.

Figure 4-4 illustrates the comparison of elapsed time between Landweber iteration, TV regularisation, l_1 regularisation, and the proposed AGS method. Image reconstruction was performed using Matlab 2013a installed on a Windows desktop with an Intel Xeon CPU (X5650 @ 2.67 GHz, 2 processors) and 24 GB RAM memory. According to previous studies (Deng et al., 2013), the computation cost of each iteration of ADMM was O(*mn*) when applied to solve (4.10), while the computation cost of solving (4.2) using the gradient method was O(*nn*). As indicated in Figure 4-4, the elapsed time of all phantoms using AGS is less than 0.6 seconds, faster than the other given methods, reassuring its low computation cost as well as its feasibility of real-time implementation in the future.

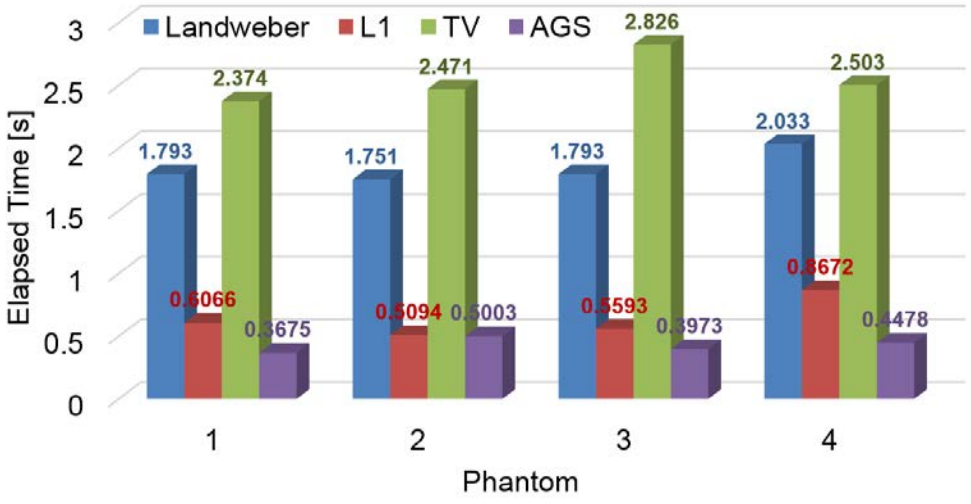

Figure 4-4 Comparison of elapsed time of the image reconstruction procedure for each simulation phantom.

Figure 4-5 demonstrates the effect of weighting value, i.e., w_i, on image quality, using phantom 3 as an example. Two weighting strategies were compared, i.e., weighting based on (4.15) and weighting using the all one vector as described by (4.14). Figure 4-5(a) shows the reconstructed image using the same weight for all pixel groups. The correlation coefficient and image error of Figure 4-5(a) are 0.8764 and 51.65, respectively. Compared with the image shown in Figure 4-5(a), slightly better image quality was obtained in Figure 4-5(b), if the weighting strategy in (4.15) was adopted. The result suggests that by giving a smaller weight to the large pixel groups and a larger weight to the small pixel groups as stated by (4.15), the image quality can be further improved, because in this way the sparsity of the estimation is promoted.

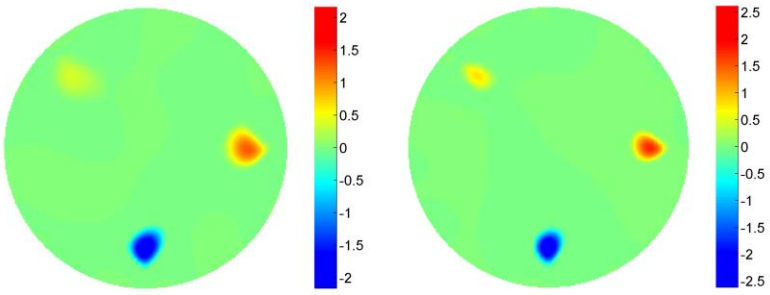

IE: 51.65
CC: 0.8764

(a)

IE: 42.21
CC: 0.9098

(b)

Figure 4-5 Comparison of different weight values of AGS on image quality of Phantom 3. (a) Weighting strategy in (4.14). (b) Weighting strategy in (4.15).

4.3.2 Experiment Results

The performance of AGS was also validated by phantom experiments in this subsection. Figure 4-6 illustrates the experiment setup. The experiments were conducted with the mfEIT system demonstrated in Chapter 2. A 16-electrode EIT sensor was used, whose inner diameter is 95 mm. All test phantoms had the same background substance as a reference, i.e., saline with a conductivity of 0.05 $S \cdot m^{-1}$. In the experiments, current excitation frequency was selected as 10 kHz and current amplitude was set as 1.5 mA peak to peak. Adjacent sensing strategy was adopted and the amplitude data of the response signal were acquired for image reconstruction.

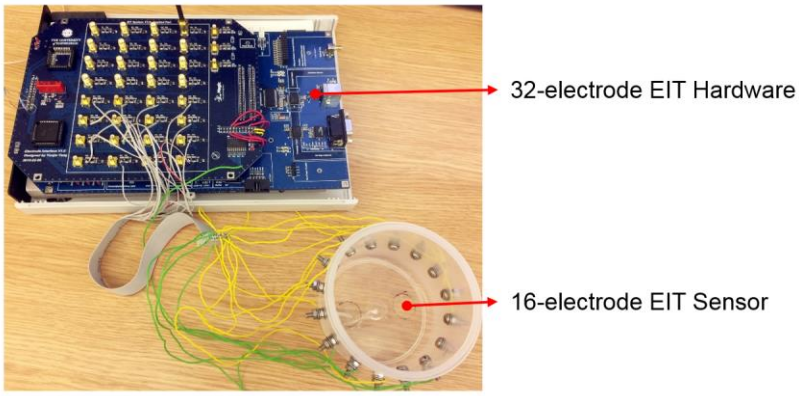

Figure 4-6 The experiment setup.

Four practical phantoms as illustrated in the first column of Table 4-5 were imaged, i.e., three glass rods (object-sensor diameter ratio is 6%), a glass rod (object-sensor diameter ratio is 6%) with a metal rod (object-sensor diameter ratio is 7%), three plastic rods (object-sensor diameter ratio is 16%), and three metal rods (object-sensor diameter ratio is 6%). While implementing the algorithms, the maximum iteration number of Landweber iteration, l_1 regularisation, TV regularisation and AGS algorithm was set to be 500 and the stopping tolerance was set to be 1e-7. Other algorithm parameters were chosen the same with the simulation setup, which are demonstrated in the first row of Table 4-5. In order to quantitatively evaluate the accuracy of reconstruction, the imaging results were normalised to the interval [-1, 1], then the relative image error and correlation coefficient stated by (4.16) and (4.17) were calculated for each phantom. Note that the reconstructed images were only normalised for the calculation of image error and correlation coefficient but not in the displayed results.

Table 4-5 provides the image reconstruction results based on Landweber iteration, l_1 regularisation, TV regularisation and the proposed AGS algorithm, as well as their quantitative evaluation results. The pixel grouping results and detail group numbers of each phantom are presented in Table 4-6. Overall, comparable results with respect to the simulation study were obtained. The AGS algorithm achieves much smaller image errors below 55%, and higher correlation coefficients above 0.84 for the first and the third phantoms, whilst slightly larger errors for the second and last phantoms because of their challenging setups. Instead, the comparing

Table 4-5 Image Reconstruction Results Based on Experiment Data.

Phantom	**Landweber** Step factor α in Eq.(4.1): 2	**l_1** Step factor in Eq. (2.16): 2	**TV** Step factor α in Eq. (4.2): 2	**AGS** d_{max}: 20; **w**: Eq. (4.15), λ: 0.01
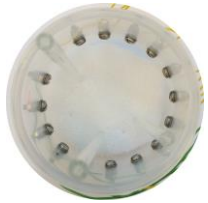	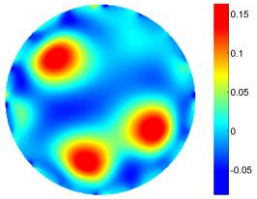	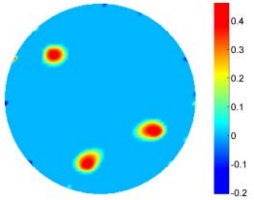	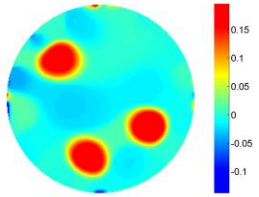	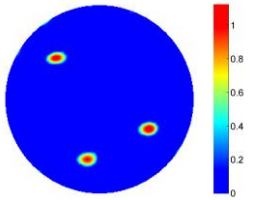
IE [%]	246.4	87.34	240.8	54.04
CC	0.3393	0.6238	0.3328	0.8410
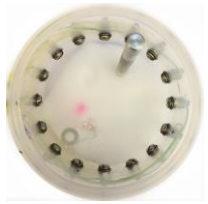	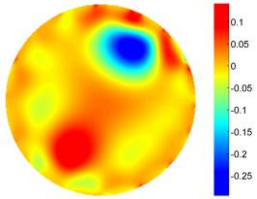	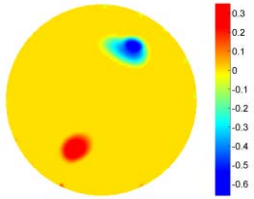	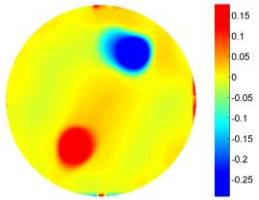	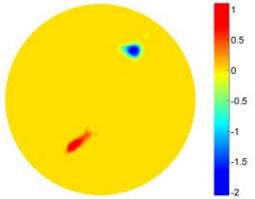
IE [%]	366.8	94.20	335.8	61.53
CC	0.2845	0.5206	0.2788	0.7842
	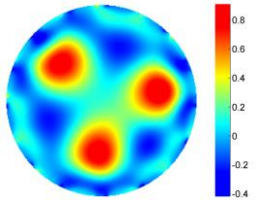	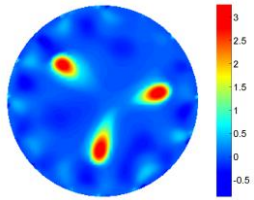	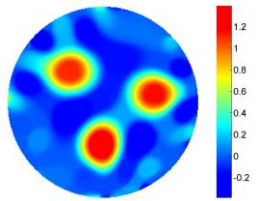	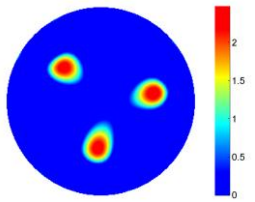

IE [%]	90.44	65.01	71.73	52.41
CC	0.6342	0.7725	0.7251	0.8571
	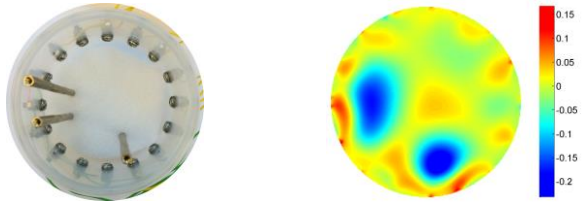			
IE [%]	367.3	107.70	267.7	75.40
CC	0.2592	0.4112	0.2454	0.6649

Table 4-6 Pixel Grouping Result of Each Phantom.

Phantom 1		**Phantom 2**		**Phantom 3**		**Phantom 4**	
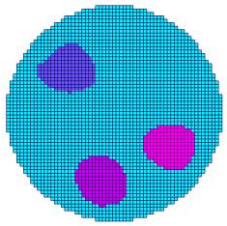	Large group number: 3 Small group number: 2711	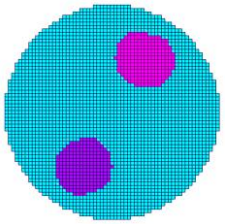	Large group number: 2 Small group number: 2781	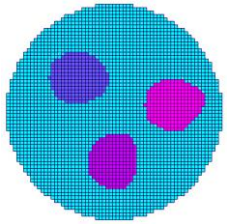	Large group number: 3 Small group number: 2624	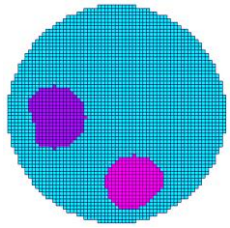	Large group number: 2 Small group number: 2872

algorithms, i.e., Landweber iteration, l_1 regularisation and TV regularisation offer much larger image errors and smaller correlation coefficients, and also cannot distinguish the small objects close to each other. It is suggested by the results that significant image noise reduction and spatial resolution improvement have been observed from the AGS based results, indicating a much better image quality in comparison with the conventional iterative algorithms.

The adaptive pixel grouping results of each phantom are illustrated in Table 4-6. It shows great similarity with the simulation study, which verifies the effectiveness of the adaptive pixel grouping method in practical applications.

In summary, the experiment results confirmed further the superior performance of the proposed AGS algorithm under practical setup. The AGS algorithm can be expected to generate high quality tomographic images especially for the applications requiring high spatial resolution and enhanced noise deduction performance, such as cell spheroid imaging in cell culture process sensing and dispersed air bubbles imaging in multiphase flow measurement.

4.4 Summary

In this chapter, a novel image reconstruction algorithm on the basis of adaptive group sparsity constraint was presented. The EIT image reconstruction problem was modelled with a weighted group-sparse basis pursuit model with a non-negativity constraint. The proposed AGS method efficiently utilised the underlying group sparsity structure as *a priori* knowledge for enhanced imaging performance. To facilitate fast group structure extraction, an adaptive pixel grouping method was developed for dynamic, self-adapting conductivity variation grouping. Both numerical simulation and phantom experiments on several challenging conductivity distributions were carried out for performance evaluation. The imaging results were compared with other iterative algorithms, indicating that the AGS algorithm outperforms other methods in terms of image quality and denoise performance.

The practical application of AGS algorithm in cell spheroid imaging will be presented in Chapter 7.

Chapter 5 EIT Image Reconstruction Using Enhanced Adaptive Group Sparsity with Total Variation

5.1 Introduction

Most of the conventional regularisation based EIT image reconstruction algorithms focus on the global characteristics of the conductivity, for instance, distinct boundaries or smooth distributions. Therefore, constraints are generally posed on the image as a whole. Recently, the effect of regional structure information on image quality improvement has aroused a great deal of interest. In Chapter 4, the encoding of regional structure information based on an adaptive group sparsity constraint named AGS was presented, and the effectiveness of utilising structure information as prior was justified. In this chapter, as a following-up study of the work in Chapter 4, another novel image reconstruction algorithm for EIT with constraints not only on regional structure features but also on global characteristics was proposed. The combination was expected to integrate both features in the images. The regional structure feature was extracted adaptively by proposing an enhanced adaptive group sparsity method based on Otsu's thresholding method (Otsu, 1979). Meanwhile, the global characteristic of the inclusions' boundary was considered by imposing a TV constraint on the whole image. The enhanced adaptive group sparsity with TV method was named as EAGS-TV. An accelerated alternating direction method of multipliers was utilised to solve the optimisation problem for a faster convergence rate. The performance of EAGS-TV was evaluated by numerical simulation and phantom experiments, and the results were compared with other iterative algorithms, including AGS.

5.2 Enhanced Adaptive Group Sparsity with Total Variation

5.2.1 Enhanced Adaptive Structure Features Extraction

Recall that in subsection 1.2.2 of Chapter 4, it was proposed that the conductivity variation $\Delta\boldsymbol{\sigma}$ could be split into a number of subsets or groups based on

amplitude similarity defined by ***Criterion 1*** and Euclidean distance of individual pixels defined by ***Criterion 2***, as expressed by:

$$\begin{cases} \Delta\boldsymbol{\sigma}_{\mathbf{s}_i} = \left[\Delta\boldsymbol{\sigma}(\mathbf{S}_i(1)), \quad \cdots \quad \Delta\boldsymbol{\sigma}(\mathbf{S}_i(K_i))\right], \\ \Delta\boldsymbol{\sigma}_{\mathbf{s}_i} \subseteq \Delta\boldsymbol{\sigma}, \\ \mathrm{U}_{i=1}^{N} \Delta\boldsymbol{\sigma}_{\mathbf{s}_i} = \Delta\boldsymbol{\sigma} \end{cases} \tag{5.1}$$

where $\mathbf{S}_i$ denotes the index vector of the i^{th} group, and i=1, 2, …, N; K_i is the length of $\mathbf{S}_i$ and N denotes the total number of subsets or groups after partition. On this basis, the underlying structure features of conductivity variation can be encoded by a reasonable group partition of all pixels.

In order to obtain better pixel grouping with improved noise immunity performance, an enhanced adaptive pixel grouping method based on the estimated conductivity variation using the filtered one-step Gauss-Newton solver with Laplacian regularisation (Yang et al., 2014) and Otsu's thresholding method (Otsu, 1979) was proposed. The filtered form of (2.14) is formulated as:

$$\Delta\hat{\boldsymbol{\sigma}} = P\left\{\left|(\mathbf{J}^{\mathrm{T}}\mathbf{J} + \lambda^2\mathbf{L}^{\mathrm{T}}\mathbf{L})^{-1}\mathbf{J}^{\mathrm{T}}\Delta\mathbf{V}\right|\right\} \tag{5.2}$$

where λ and $\mathbf{L}$ denote the regularisation factor and the four-connected region second-order Laplacian operator matrix (Yang et al., 2014), respectively. The operator $|\boldsymbol{\gamma}|$ means that each element of the vector $\boldsymbol{\gamma}$ takes its absolute value. The filtering operator P is defined as:

$$P[f(x)] = \begin{cases} f(x), & f(x) > t^* \\ 0, & f(x) \le t^* \end{cases} \tag{5.3}$$

where t^* is the optimal threshold. It is calculated based on the Otsu's thresholding method (Otsu, 1979). The Otsu's thresholding method is used commonly in the image processing field for purpose of extracting objects from the background (Sha et al., 2016). The purpose of using the filter operation is to obtain good robustness against noise. Refer to Otsu's work (Otsu, 1979), the optimal threshold t^* is

calculated by maximising the between-class (i.e., the conductivity variation and the background) variance with an exhaustive search, which is stated by:

$$t^* = \arg\max_{1\le t<L} \frac{\left[(\sum_{i=1}^{L} ip_i)(\sum_{i=1}^{t} p_i) - \sum_{i=1}^{t} ip_i\right]^2}{(\sum_{i=1}^{t} p_i)\left[1-\sum_{i=1}^{t} p_i\right]} \tag{5.4}$$

where L denotes the total gray levels of the absolute value of the reconstruction image, and $p_i = e_i / n$; e_i is the number of pixels at the i^{th} gray level and n is the total number of pixels.

After the estimation is performed by using (5.2), the number and geometric centres of the inclusions are further identified by calculating all of the local maximum points of the conductivity estimation. The pixel indices of all local maximum points is represented by a vector $\mathbf{D} \in \mathrm{R}^q$ and the coordinate of all pixels is denoted by a matrix $\mathbf{C} \in \mathrm{R}^{n\times 2}$. The pixel grouping result is then expressed by a group index vector $\mathbf{G} \in \mathrm{R}^n$. In $\mathbf{G}$, pixels belonging to the same group are assigned the same index value. On the basis of the above definitions, the index set of the pixels which have amplitude similarity, i.e. satisfying ***Criterion 1*** defined in the last chapter, with the i^{th} (i=1, 2, …, q) local maximum point $\mathbf{D}(i)$, is defined by:

$$\mathbf{A}_{\mathrm{s}} = \left\{ j \mid \Delta\hat{\boldsymbol{\sigma}}_j > \frac{1}{4}\Delta\hat{\boldsymbol{\sigma}}_{\mathbf{D}(i)}, j = 1,...,n \right\} \tag{5.5}$$

and the index set of the pixels which have proximity Euclidean distance, i.e. satisfying ***Criterion 2*** defined in the last chapter, with the i^{th} (i=1, 2, …, q) local maximum point $\mathbf{D}(i)$, is stated by:

$$\mathbf{E}_{\mathrm{s}} = \left\{ j \mid \left\| \mathbf{C}_j - \mathbf{C}_{\mathbf{D}(i)} \right\|^2 < (\frac{d_{\max}}{2})^2, \quad j = 1,...,n \right\} \tag{5.6}$$

Finally, the pixel group centres on the i^{th} local maximum point $\mathbf{D}(i)$ is denoted by an index vector $\mathbf{Q}$, which is defined to satisfy both the amplitude similarity and proximity Euclidean distance criteria, as stated by:

$$\mathbf{Q}=\mathbf{A}_s \bigcap \mathbf{E}_s \tag{5.7}$$

The amplitude similarity and geographic proximity are guaranteed by (5.7). An intuitional schematic illustration of the enhanced adaptive pixel grouping algorithm is shown in Figure 5-1. The detailed implementation is summarised in Table 5-1.

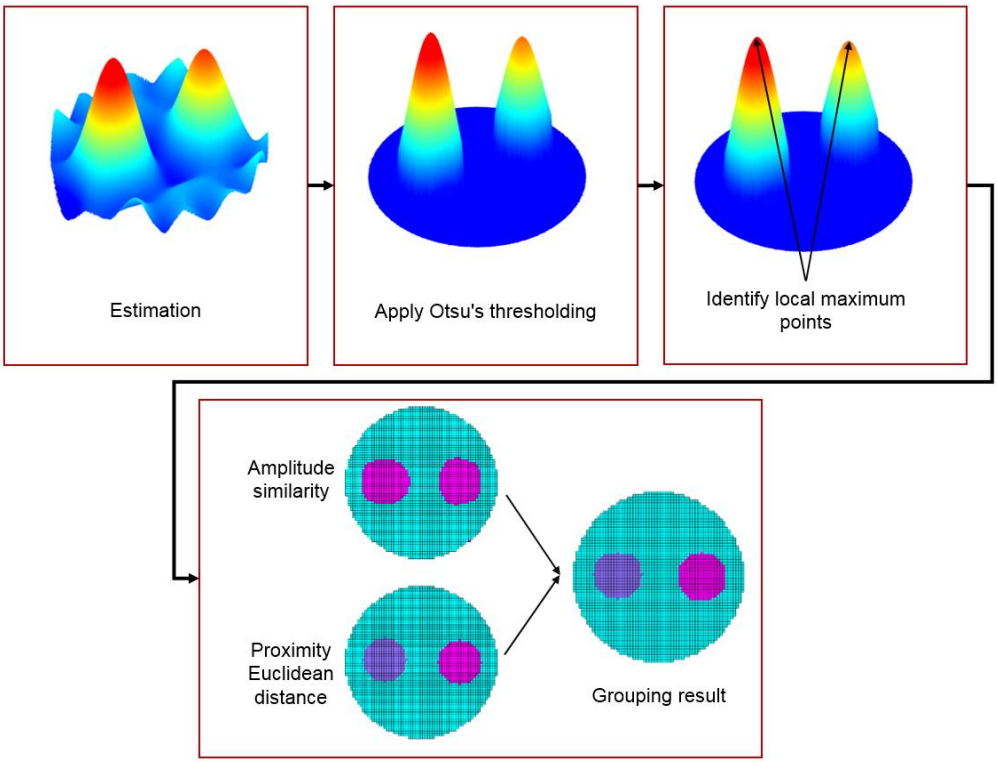

Figure 5-1 Schematic illustration of adaptive pixel grouping algorithm.

Table 5-1 Enhanced Adaptive Pixel Grouping Algorithm.

Algorithm 5-1: Enhanced adaptive pixel grouping algorithm

Input: Boundary voltage $\Delta\mathbf{V}$, Jacobian matrix $\mathbf{J}$, and maximum group diameter d_{max}

Step 1: Estimate the filtered absolute conductivity change based on (5.2).

Step 2: Identify the number and pixel index of the local maximum points of the estimated conductivity from Step 1.

Step 3: Calculate the group index vector $\mathbf{G}$ based on (5.5), (5.6) and (5.7).

Output: The group index vector $\mathbf{G}$.

5.2.2 The Proposed EAGS-TV Algorithm

As a further study of the work demonstrated in the last chapter, the new work not only considers to utilise the regional structure features as *a priori* information but also merge simultaneously some global constraints such as the explicit boundary of conductivity distribution, in order to promote both features in the reconstructed images. To achieve this target, an EIT image reconstruction algorithm using the enhanced adaptive group sparsity with total variation, named as EAGS-TV, was developed. This is formulated as:

$$\begin{cases} \min\limits_{\Delta\boldsymbol{\sigma}} & \sum\limits_{i=1}^{N} w_i \left\| \Delta\boldsymbol{\sigma}_{\mathbf{s}_i} \right\|_2 + \left\| \Delta\boldsymbol{\sigma} \right\|_{\mathrm{TV}} \\ s.t. & \mathbf{J}\Delta\boldsymbol{\sigma} = \Delta\mathbf{V}, \\ & g(\Delta\boldsymbol{\sigma}) \cdot \Delta\boldsymbol{\sigma} \geq 0 \end{cases} \tag{5.8}$$

where $\sum_{i=1}^{N} w_i \left\| \Delta\boldsymbol{\sigma}_{\mathbf{s}_i} \right\|_2$ is the weighted $l_{2,1}$ norm, i.e. $\|\Delta\boldsymbol{\sigma}\|_{w,2,1}$; w_i is the weight for the i^{th} group; $\|\Delta\boldsymbol{\sigma}\|_{\mathrm{TV}}$ is the isotropic TV norm which is defined by (2.18) in Chapter 2; and the operator g is defined by (4.7) in Chapter 4.

The accelerated alternating direction method of multipliers (A-ADMM) (Goldstein et al., 2014) was utilised to tackle the coupled constraint problem in (5.8).

A-ADMM is an accelerated variant of ADMM. By applying an over-relaxation step in each iteration, A-ADMM exhibits a faster convergence rate than the conventional ADMM (Goldstein et al., 2014). In order to implement this method to solve (5.8), an auxiliary vector $\mathbf{z}$ is firstly introduced, then (5.8) can be rewritten equivalently as:

$$\begin{cases} \min\limits_{\Delta\boldsymbol{\sigma},\mathbf{z}} & \sum\limits_{i=1}^{N} w_i \left\| \mathbf{z}_{\mathbf{s}_i} \right\|_2 + \left\| \Delta\boldsymbol{\sigma} \right\|_{\mathrm{TV}} \\ s.t. & \mathbf{z} = \Delta\boldsymbol{\sigma},\ \mathbf{J}\Delta\boldsymbol{\sigma} = \Delta\mathbf{V}, \\ & g(\Delta\boldsymbol{\sigma}) \cdot \Delta\boldsymbol{\sigma} \geq 0 \end{cases} \tag{5.9}$$

The augmented Lagrangian scheme of (5.9) without considering the non-negative constraint is expressed as:

$$\begin{aligned} \min_{\Delta\boldsymbol{\sigma},\,\mathbf{z}} \quad & \sum_{i=1}^{N} w_i \left\| \mathbf{z}_{\mathbf{s}_i} \right\|_2 + \left\| \Delta\boldsymbol{\sigma} \right\|_{\mathrm{TV}} - \ldots \\ & \boldsymbol{\mu}_1^{\mathrm{T}} (\mathbf{z} - \Delta\boldsymbol{\sigma}) + \frac{\eta_1}{2} \| \mathbf{z} - \Delta\boldsymbol{\sigma} \|_2^2 - \ldots \\ & \boldsymbol{\mu}_2^{\mathrm{T}} (\mathbf{J}\Delta\boldsymbol{\sigma} - \Delta\mathbf{V}) + \frac{\eta_2}{2} \| \mathbf{J}\Delta\boldsymbol{\sigma} - \Delta\mathbf{V} \|_2^2 \end{aligned} \tag{5.10}$$

where $\boldsymbol{\mu}_1$ and $\boldsymbol{\mu}_2$ are multipliers and η_1 and η_2 are penalty parameters. Then (5.10) can be split into two sub-problems, i.e. the $\mathbf{z}$-subproblem and the $\Delta\boldsymbol{\sigma}$-subproblem. Then, the two sub-problems can be solved separately.

The $\Delta\boldsymbol{\sigma}$-subproblem is expressed as:

$$\begin{aligned} \Delta\boldsymbol{\sigma}^{(k+1)} = \arg\min_{\Delta\boldsymbol{\sigma}} \Big\{ & \| \Delta\boldsymbol{\sigma}^{(k)} \|_{\mathrm{TV}} + \boldsymbol{\mu}_1^{\mathrm{T}} \Delta\boldsymbol{\sigma}^{(k)} + \frac{\eta_1}{2} \| \mathbf{z} - \Delta\boldsymbol{\sigma}^{(k)} \|_2^2 - \ldots \\ & \boldsymbol{\mu}_2^{\mathrm{T}} \mathbf{J}\Delta\boldsymbol{\sigma}^{(k)} + \frac{\eta_2}{2} \| \mathbf{J}\Delta\boldsymbol{\sigma}^{(k)} - \Delta\mathbf{V} \|_2^2 \Big\} \end{aligned} \tag{5.11}$$

A gradient-based recovery algorithm is proposed to solve (5.11) iteratively, and its iteration form is given by:

$$\Delta\boldsymbol{\sigma}^{(k+1)} = \Delta\boldsymbol{\sigma}^{(k)} - \alpha \left\{ \mathbf{H} + \nabla(\left\| \Delta\boldsymbol{\sigma}^{(k)} \right\|_{\mathrm{TV}}) \right\} \tag{5.12}$$

where α is the step length and

$$\mathbf{H} = \boldsymbol{\mu}_1 + \eta_1(\Delta\boldsymbol{\sigma}^{(k)} - \mathbf{z}) + \mathbf{J}^{\mathrm{T}}(\eta_2(\mathbf{J}\Delta\boldsymbol{\sigma}^{(k)} - \Delta\mathbf{V}) - \boldsymbol{\mu}_2) \tag{5.13}$$

The gradient of the TV norm, i.e. $\nabla(\|\Delta\boldsymbol{\sigma}\|_{\mathrm{TV}})$, is defined by (4.2) in Chapter 4 by using a smooth approximation strategy. Consequently, (5.12) can be finally formulated as:

$$\begin{aligned}\Delta\boldsymbol{\sigma}^{(k+1)} = \Delta\boldsymbol{\sigma}^{(k)} - \alpha\Bigg\{ & \boldsymbol{\mu}_1 + \eta_1(\Delta\boldsymbol{\sigma}^{(k)} - \mathbf{z}) + \dots \\ & \mathbf{J}^{\mathrm{T}}(\eta_2(\mathbf{J}\Delta\boldsymbol{\sigma}^{(k)} - \Delta\mathbf{V}) - \boldsymbol{\mu}_2) + \dots \\ & \frac{D^h_{x,y}(\Delta\boldsymbol{\sigma}) + D^v_{x,y}(\Delta\boldsymbol{\sigma})}{\sqrt{(\mathrm{D}^v_{x,y}(\Delta\boldsymbol{\sigma}))^2 + (\mathrm{D}^h_{x,y}(\Delta\boldsymbol{\sigma}))^2 + \varepsilon}} - \dots \\ & \frac{D^h_{x-1,y}(\Delta\boldsymbol{\sigma})}{\sqrt{(\mathrm{D}^v_{x-1,y}(\Delta\boldsymbol{\sigma}))^2 + (\mathrm{D}^h_{x-1,y}(\Delta\boldsymbol{\sigma}))^2 + \varepsilon}} - \dots \\ & \frac{D^v_{x,y-1}(\Delta\boldsymbol{\sigma})}{\sqrt{(\mathrm{D}^v_{x,y-1}(\Delta\boldsymbol{\sigma}))^2 + (\mathrm{D}^h_{x,y-1}(\Delta\boldsymbol{\sigma}))^2 + \varepsilon}}\Bigg\}\end{aligned} \tag{5.14}$$

The **z**-subproblem is given by:

$$\mathbf{z}^{(k+1)} = \arg\min_{\mathbf{z}} \left\{ \sum_{i=1}^{N} w_i \left\| \mathbf{z}_{\mathbf{s}_i}^{(k+1)} \right\|_2 - \boldsymbol{\mu}_1^{\mathrm{T}}\mathbf{z}^{(k)} + \frac{\eta_1}{2} \| \mathbf{z}^{(k)} - \Delta\boldsymbol{\sigma} \|_2^2 \right\} \tag{5.15}$$

The problem can be solved explicitly by using the group-wise soft thresholding method (Donoho, 1995), which is stated by:

$$\mathbf{z}_{s_i} = \max\left\{ \left\| \Delta\boldsymbol{\sigma}_{s_i} + \frac{1}{\eta_1}(\boldsymbol{\mu}_1)_{s_i} \right\|_2 - \frac{w_i}{\eta_1}, 0 \right\} \frac{\Delta\boldsymbol{\sigma}_{s_i} + \frac{1}{\eta_1}(\boldsymbol{\mu}_1)_{s_i}}{\left\| \Delta\boldsymbol{\sigma}_{s_i} + \frac{1}{\eta_1}(\boldsymbol{\mu}_1)_{s_i} \right\|_2} \tag{5.16}$$

The detailed implementation of the EAGS-TV algorithm is demonstrated in Table 5-2.

Table 5-2 Enhanced Adaptive Group Sparsity with Total Variation (EAGS-TV) Algorithm.

Algorithm 5-2: Enhanced adaptive pixel grouping algorithm

Input: Boundary voltage change $\Delta\mathbf{V}$, Jacobian matrix $\mathbf{J}$, group index vector $\mathbf{G}$, and weighting vector $\mathbf{w}$.

initialize: Starting point ($\mathbf{z}$, $\Delta\boldsymbol{\sigma}$, $\boldsymbol{\mu}_1$, $\boldsymbol{\mu}_2$, η_1, η_2, α_1, α_2, d)

iteration:

1): Solve the $\Delta\boldsymbol{\sigma}$-subproblem depicted by (5.11).

2): Solve the $\mathbf{z}$-subproblem depicted by (5.15).

3): Impose the constraint based on (4.7).

4): Update the multipliers based on the accelerated method as stated below:

$$\hat{\boldsymbol{\mu}}_1^{(k+1)} = \boldsymbol{\mu}_1^{(k)} - \alpha_1\boldsymbol{\eta}_1(\mathbf{z}^{(k+1)} - \Delta\boldsymbol{\sigma}^{(k+1)})$$

$$\hat{\boldsymbol{\mu}}_2^{(k+1)} = \boldsymbol{\mu}_2^{(k)} - \alpha_2\boldsymbol{\eta}_2(\mathbf{J}\Delta\boldsymbol{\sigma}^{(k+1)} - \Delta\mathbf{V})$$

$$d^{(k+1)} = \frac{1+\sqrt{1+4(d^{(k)})^2}}{2}$$

$$\mathbf{z}^{(k+1)} = \mathbf{z}^{(k+1)} + \frac{d^{(k)}-1}{d^{(k+1)}}(\mathbf{z}^{(k+1)} - \mathbf{z}^{(k)})$$

$$\boldsymbol{\mu}_1^{(k+1)} = \hat{\boldsymbol{\mu}}_1^{(k+1)} + \frac{d^{(k)}-1}{d^{(k+1)}}(\hat{\boldsymbol{\mu}}_1^{(k+1)} - \hat{\boldsymbol{\mu}}_1^{(k)})$$

$$\boldsymbol{\mu}_2^{(k+1)} = \hat{\boldsymbol{\mu}}_2^{(k+1)} + \frac{d^{(k)}-1}{d^{(k+1)}}(\hat{\boldsymbol{\mu}}_2^{(k+1)} - \hat{\boldsymbol{\mu}}_2^{(k)})$$

until a stopping criterion is satisfied.

Output: The estimated conductivity distribution.

5.3 Results and Discussion

5.3.1 Numerical Simulation

1) Modelling.

As illustrated in Figure 5-2, a 2D 16-electrode EIT sensor with 95 mm diameter was modelled using the COMSOL Multiphysics. The homogeneous saline which conductivity was 0.05 $\mathrm{S \cdot m^{-1}}$ was used as background reference for Jacobian matrix calculation and phantom modelling. Two representative phantoms, i.e. one

circle with one ellipse as shown in Figure 5-2(b) and two circles with one square as shown in Figure 5-2(c), were established for simulation study. The purpose of using the first phantom was to evaluate the algorithm performance for spatially non-sparse distribution and the second phantom was to assess the algorithm performance for spatially sparse distribution with bi-direction conductivity changes. The conductivity value of the red objects was set as 0.0001 $\mathrm{S \cdot m^{-1}}$ and the blue circle was 10 $\mathrm{S \cdot m^{-1}}$.

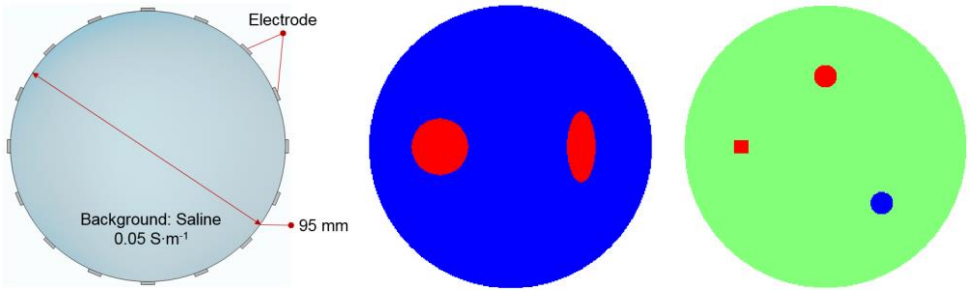

(a) (b) (c)

Figure 5-2 Simulation modelling. (a) Sensor model. (b) Phantom 1: circle with ellipse. (c) Phantom 2: circles with square.

The adjacent sensing strategy (Brown and Seagar, 1987) was adopted for tomographic measurement. The currents were injected through an adjacent pair of electrodes and differential voltage measurements were conducted through successive pairs of the neighbouring electrodes. Therefore, a completed frame was composed of 104 independent measurements.

2) Comparing algorithms and parameters.

To verify the effectiveness of EAGS-TV, this method was compared with the state-of-the-art image reconstruction algorithms, i.e., the l_1 regularisation algorithm (l_1) formulated by (2.16) in Chapter 2, the TV regularisation algorithm (TV) stated by (2.17) in Chapter 2, and AGS depicted in (4.6) in the last chapter.

When EAGS-TV was implemented, the regularisation factor λ in (5.2) was set as 0.001. The penalty parameters η_1 and η_2 in (5.11) were empirically selected as 1/mean(abs($\Delta\mathbf{V}$)) and 0.6/mean(abs($\Delta\mathbf{V}$)) respectively, based on a series of practices. Here, mean denotes the average function and abs denotes the absolute value function. The step length α_1 and α_2 were selected equally as 0.98. The maximum group

diameter d_{max} was set as 20 pixels, which was large enough for the targeted biomedical applications. With respect to the weighting strategy, following the discussion in the last chapter, the all-one vector in (4.14) was applied for the non-sparse phantom 1 and (4.15) was employed for the sparse phantom 2.

For l_1 regularisation, the relaxation factor was set as 0.1 and the step factor was set as 2 and, for TV regularisation, the regularisation factor was set as 0.01. The algorithm parameters of AGS were set as the same with those in the last chapter. The maximum iteration number for all algorithms was set as 500 and the stopping criterion was defined as follows:

$$\left\| \Delta\boldsymbol{\sigma}^{(k+1)} - \Delta\boldsymbol{\sigma}^{(k)} \right\|_2 < tol \tag{5.17}$$

where *tol* was select to be 1e-5 in this work.

In the simulation study, the same parameters were applied for all test phantoms.

3) Image quality evaluation.

The quality of reconstructed images were evaluated quantitatively by using relative image error (IE) and correlation coefficient (CC) with respect to the ground truth. A smaller value of image error and a larger value of correlation coefficient suggest a better image quality. The definitions of IE and CC are demonstrated respectively in (4.16) and (4.17) in Chapter 4.

4) Simulation results.

The noise-contaminated measured data with different SNR levels, i.e. 60 dB, 40 dB, 35 dB and 25 dB, were adopted for image reconstruction in order to evaluate the noise reduction performance of the algorithms. The image reconstruction results of the two test phantoms by using l_1 regularisation, TV regularisation, AGS and EAGS-TV are illustrated in Figure 5-3 (60 dB SNR), Figure 5-4 (40 dB SNR), Figure 5-5 (35 dB SNR), and Figure 5-6 (25 dB SNR), respectively.

The spatial distribution of conductivity variation in phantom 1 is not sparse. As a result, l_1 regularisation evidently underestimated the dimension of the inclusions. Moreover, the boundary distortion near the centre of the sensor revealed that l_1 regularisation could not perform well on such kind of non-sparse phantoms. With the decrease of SNR, more noise and distortion were presented in the reconstructed images by using the l_1 regularisation. By contrast, TV regularisation could generate slightly better reconstructions than l_1 regularisation, but it was still not able to show the correct shape of the targets. Compared with l_1 and TV regularisation, both AGS and EAGS-TV demonstrated pretty good estimation of the shape of targets and superior background noise reduction. Further comparison of the two algorithms showed that the EAGS-TV apparently demonstrated the best image quality with more accurate shape estimations and clearer inclusion boundaries. Moreover, the EAGS-TV results showed fewer distortions than the AGS results with the decrease of SNR, which justified the improved robustness of this method against noise.

Regarding phantom 2, the spatial distribution of conductivity change is sparse. Under this circumstance, although the TV regularisation provided clear boundaries, it overestimated the dimension of the inclusions. Different from the results of phantom 1, the l_1 regularisation performed pretty well on phantom 2 with good background noise reductions and shape estimations. However, the distortion still existed towards the direction of the sensor centre. As suggested by the images, both AGS and EAGS-TV outperformed the l_1 regulation and TV regularisation for this sparse phantom. Compared with AGS, more accurate shape estimations and clearer boundaries of the inclusions were obtained by using EAGS-TV and, its noise reduction performance was much better than AGS when the SNR was 40 dB and 35 dB.

Figure 5-7 provides the image errors and correlation coefficients of the imaging results in Figure 5-3, Figure 5-4, Figure 5-5 and Figure 5-6. In summary, the image error decreased and the correlation coefficient increased with the increase of SNR for all the algorithms discussed. The smallest image errors and the highest correlation coefficients were obtained by EAGS-TV. As for phantom 1, EAGS-TV could achieve image errors lower than 52% and correlation coefficients higher than 0.8670, when the SNR was higher than 40 dB. With respect to phantom 2, the image

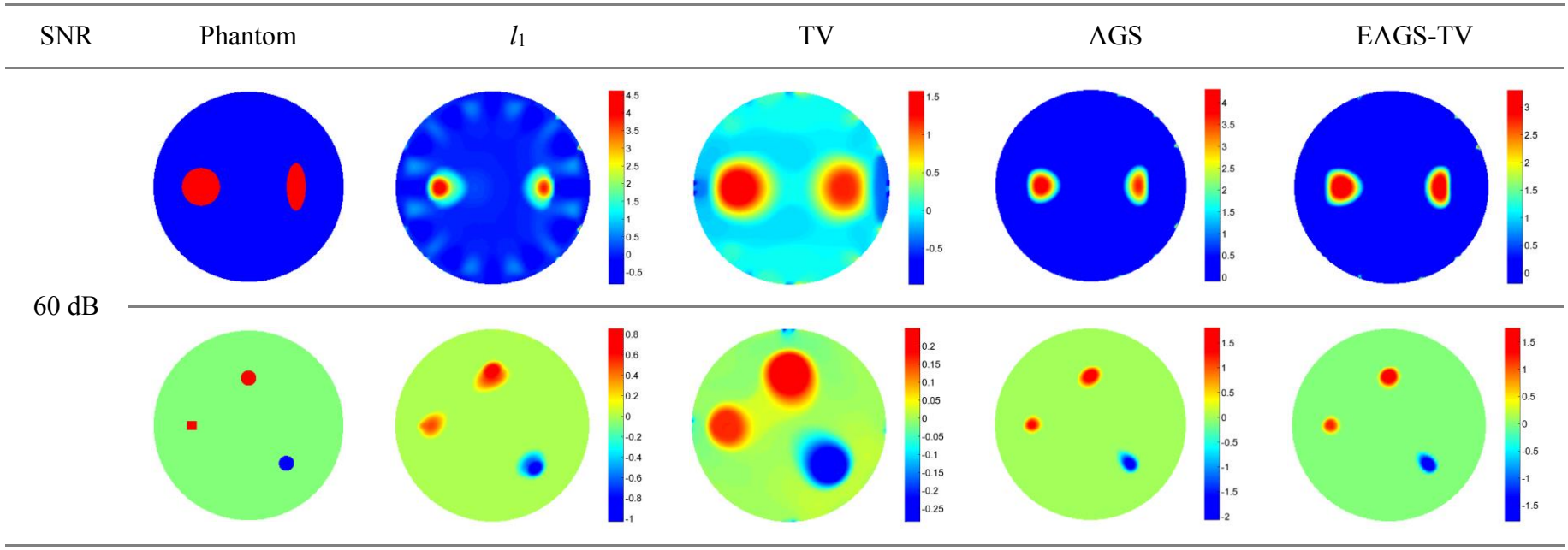

Figure 5-3 Image reconstruction results based on simulation data with 60 dB SNR.

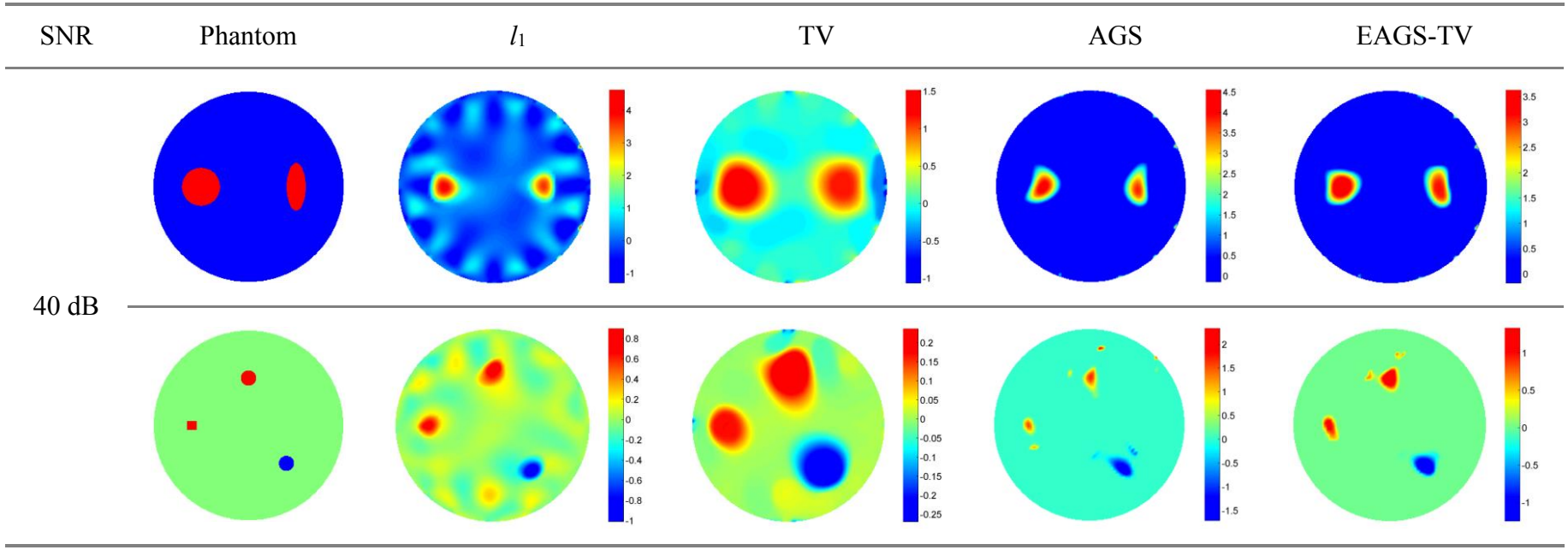

Figure 5-4 Image reconstruction results based on simulation data with 40 dB SNR.

SNR	Phantom	l_1	TV	AGS	EAGS-TV
35 dB	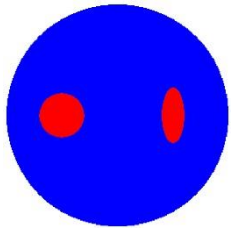	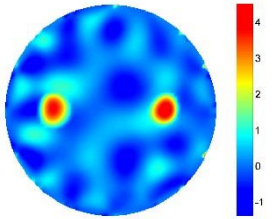	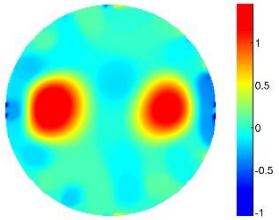	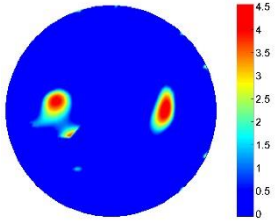	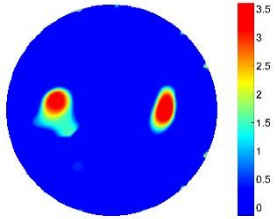
	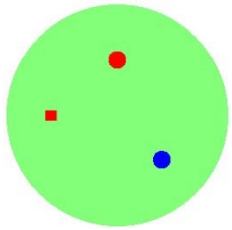	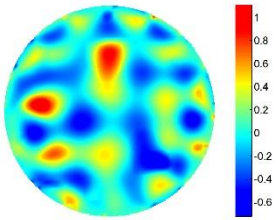	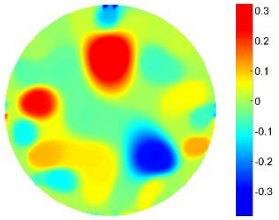	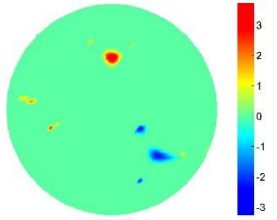	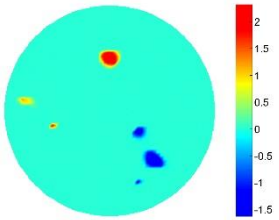

Figure 5-5 Image reconstruction results based on simulation data with 35 dB SNR.

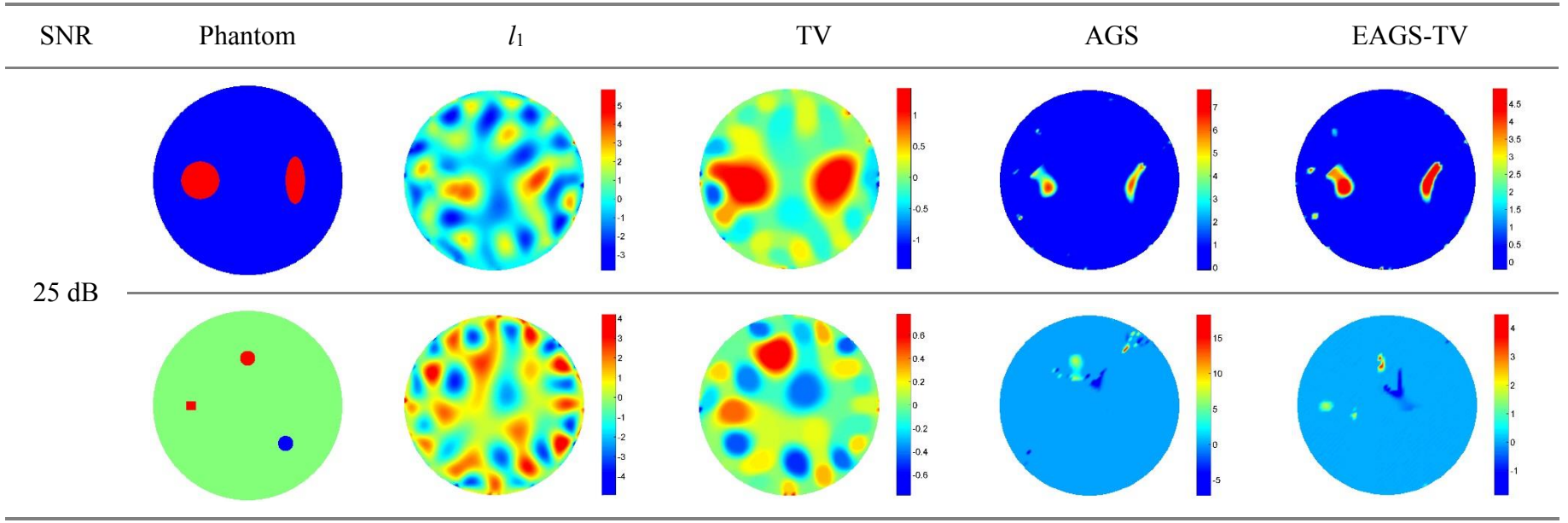

Figure 5-6 Image reconstruction results based on simulation data with 25 dB SNR.

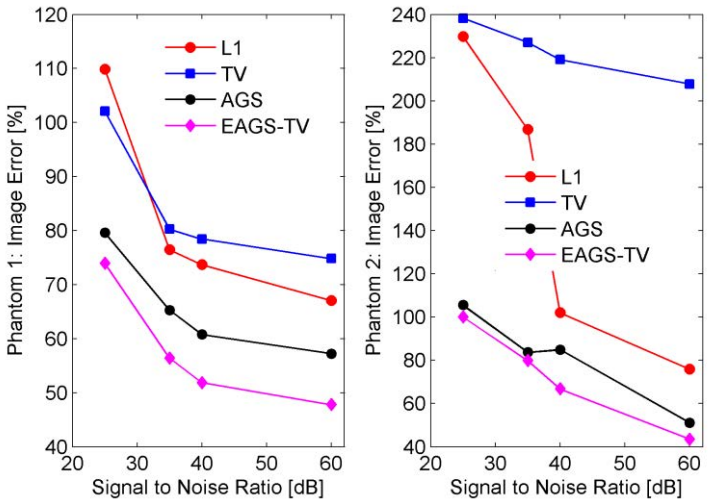

(a)

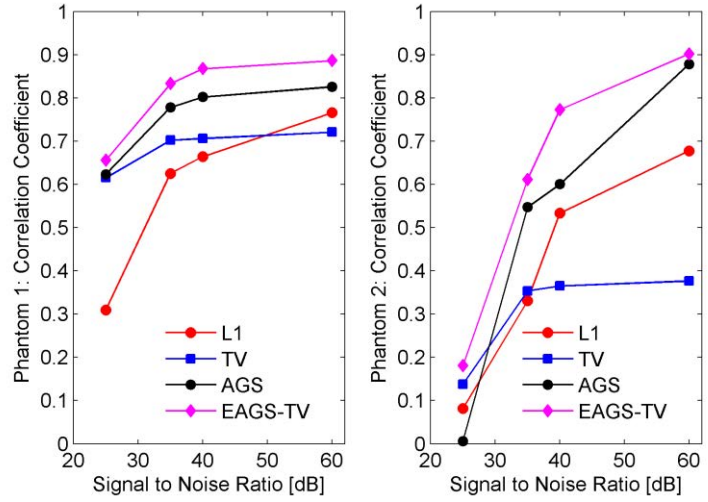

(b)

Figure 5-7 Quantitative evaluation results. (a) Image errors. (b) Correlation Coefficients.

errors were below 67% and correlation coefficients were above 0.7720, when the SNR was higher than 40 dB, which apparently outperformed the other algorithms. Overall, the image errors of EAGS-TV were improved by about 9% when compared with the AGS method while the SNR was above 40 dB. The quantitative evaluation results further validated the superior performance of EAGS-TV.

Figure 5-8 shows the pixel grouping results of the two phantoms under the given SNR levels. The total number of groups was denoted as nG and the number of groups containing the inclusions, highlighted by darker colours, was denoted as nBG.

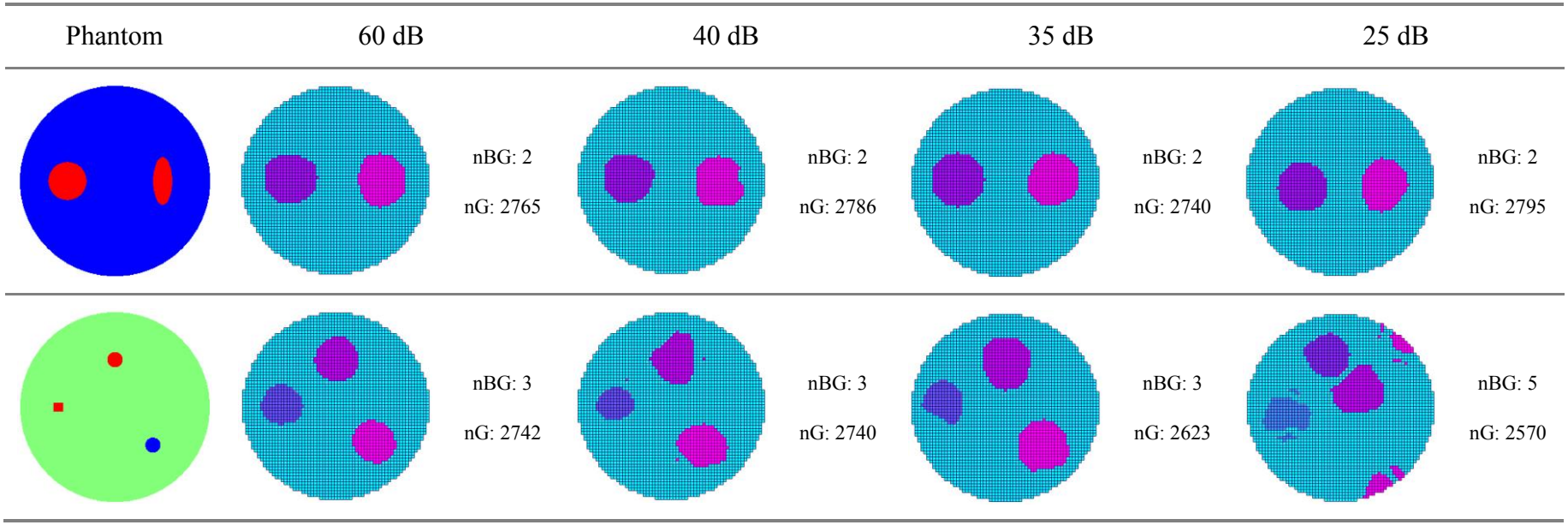

Figure 5-8 Enhanced adaptive pixel grouping results based on algorithm 5-1 in Table 5-1.

It was shown that reasonable grouping results could be obtained at different SNR levels for phantom 1. However, the pixel grouping for phantom 2 collapsed when the SNR was 25 dB, because in this case, the measured data could not be well distinguished from noise. Overall, in spite of the existence of some noisy spots and distortions, the generated groups could include the inclusion areas and demonstrated the correct position of the imaging targets.

Figure 5-9 illustrates the elapsed time of the given algorithms for the two simulated phantoms. The reconstruction procedures were conducted on a laptop with an Intel i7-3537U CPU (2.0 GHz) and 8.0 GB RAM memory. Figure 5-9 indicated that all the algorithms completed the reconstruction process within 5 seconds and their elapsed times were comparable. Although EAGS-TV was slightly more time-consuming than other algorithms due to the incorporation of total variation constraint, it outperformed other algorithms in image quality with an affordable computation cost.

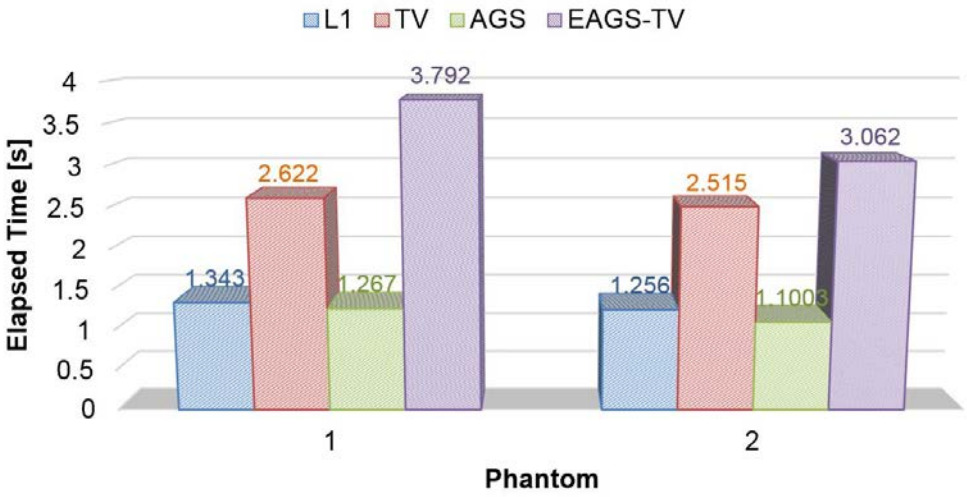

Figure 5-9 Elapsed time of the algorithms for two phantoms.

5.3.2 Experiment Results

In this subsection, the practical performance of EAGS-TV was assessed via phantom experiments on a 16-electrode EIT sensor by using the mfEIT system demonstrated in Chapter 3. The experimental setup is shown in Figure 5-10. The

inner diameter of the 16-electrode sensor was 95 mm. The background substance for reference purpose was saline, which conductivity was 0.05 $S \cdot m^{-1}$.

In all of the experiments, the frequency of current excitation was set as 10 kHz and the amplitude of the injected currents was approximately 1.5 mA peak to peak. The adjacent sensing strategy was adopted for tomographic measurement and amplitude data of the measured voltage were acquired for image reconstruction.

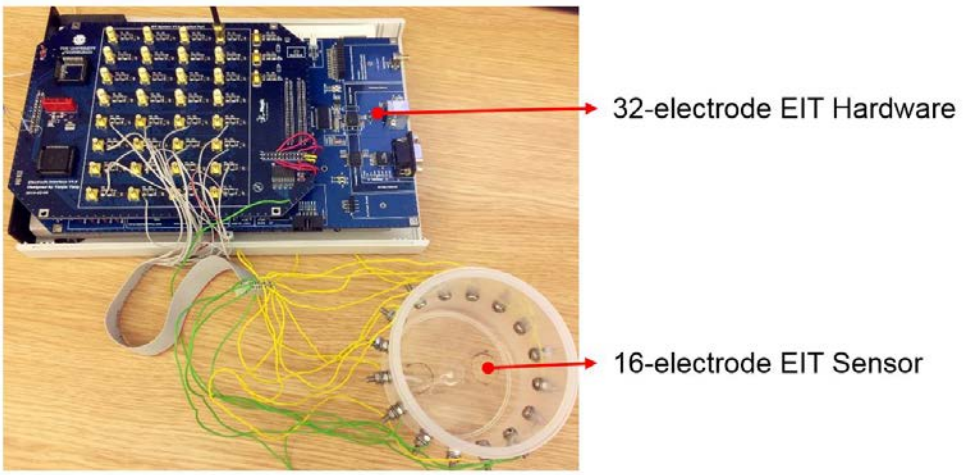

Figure 5-10 Experimental setup.

Two phantoms, i.e. the non-sparse phantom 1 as shown in the first row of Figure 5-11 and the sparse phantom 2 as shown in the second row of Figure 5-11, were imaged. The same algorithm parameters and stopping criterion as presented in the numerical simulation part were adopted.

Figure 5-11 presents the image reconstruction results from l_1 regularisation, TV regularisation, AGS and EAGS-TV based on experimental data. In general, the results showed good similarity with the numerical simulation results. By comparing the results of phantom 1, it was found that EAGS-TV demonstrated the best image quality in terms of noise reduction of the background, accuracy of shape estimation and object boundary estimation. Similar to the simulation result, l_1 regularisation was likely to present an estimation with smaller dimensions, if the target distribution was not sparse. While TV regularisation failed to estimate the shape accurately. The AGS demonstrated good noise performances, but the boundaries of the inclusions were not

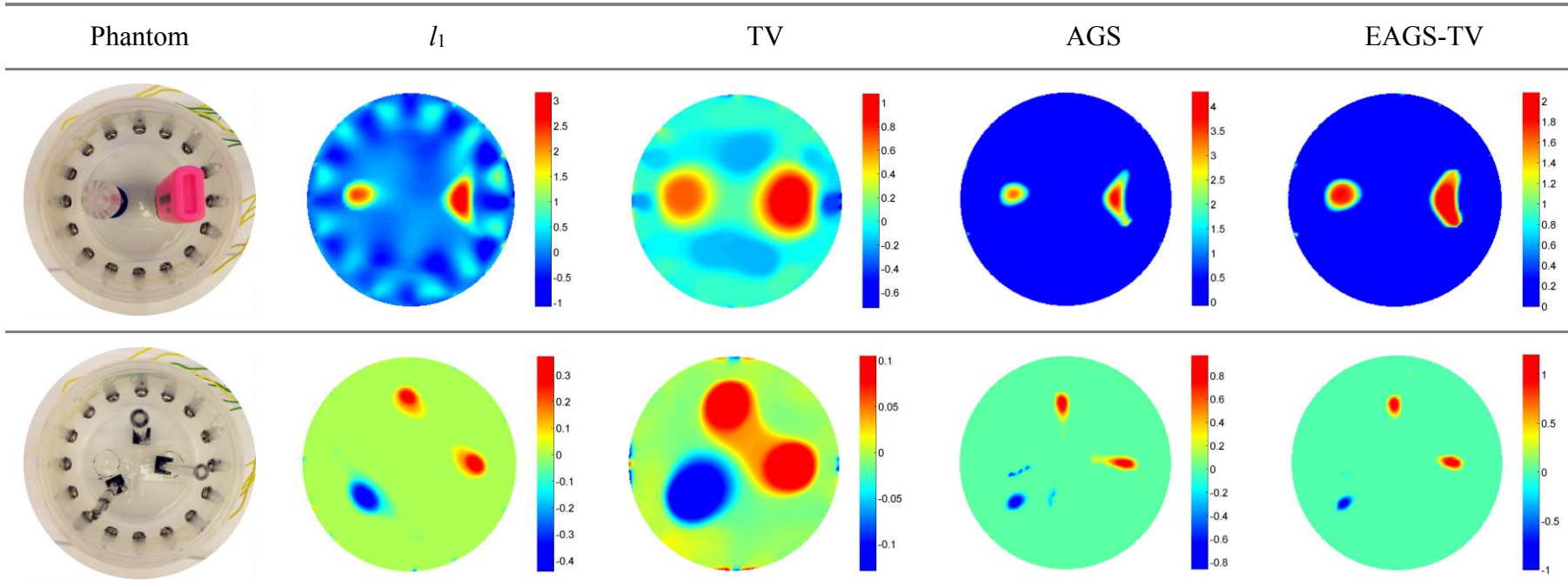

Figure 5-11 Image reconstruction results based on experimental data.

explicit enough. As for phantom 2, l_1 regularisation offered relatively good image, but there still existed distortions towards the centre of the sensor. The TV regularisation, which gave much bigger sizes for the tiny objects, could not estimate accurately the dimension of the inclusions. The AGS method provided much better image qualities than the l_1 and TV methods, but a few artefacts still existed. In contrast, the EAGS-TV method not only provided correct position of the inclusions but also demonstrated more accurate dimensions with less distortions and fewer artefacts.

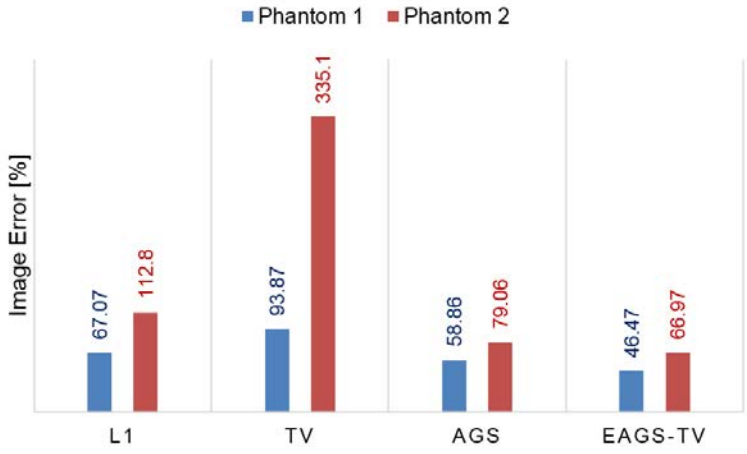

(a)

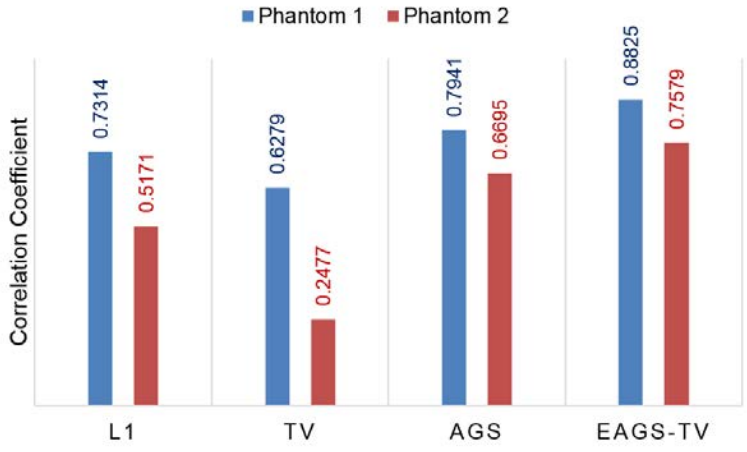

(b)

Figure 5-12 Quantitative evaluation results. (a) Image errors. (b) Correlation Coefficients.

Figure 5-12 illustrates the comparison of image errors and correlation coefficients of the imaging results in Figure 5-11. From the quantitative perspective,

EAGS-TV outperformed l_1, TV regularisation and AGS in terms of small image errors and large correlation coefficients. The image error of phantom 1 from using EAGS-TV was more than 20% smaller and that of phantom 2 was more than 40% smaller than l_1 regularisation. The correlation coefficient of EAGS-TV was 0.15 larger than l_1 regularisation for phantom 1 and 0.24 larger than l_1 regularisation for phantom 2. By comparing with AGS, image errors were reduced by more than 11% by using EAGS-TV for the two tested phantoms. The results in Figure 5-12 further justified the improvement of image quality by using EAGS-TV.

The pixel grouping results of these two experimental phantoms by using the enhanced adaptive pixel grouping algorithm are shown in Figure 5-13.

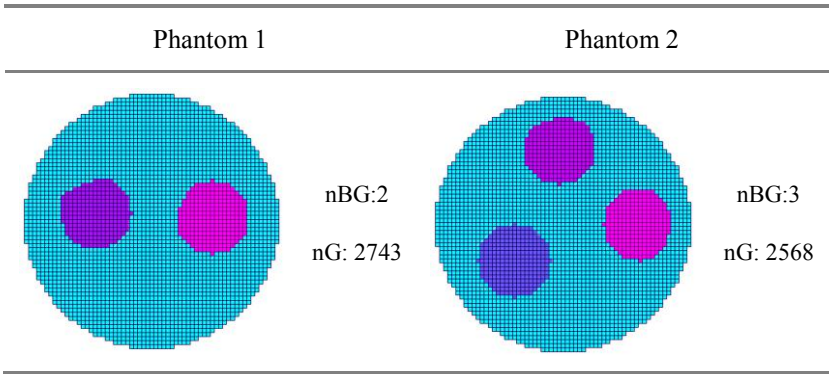

Figure 5-13 The enhanced adaptive pixel grouping results of Figure 5-11.

5.4 Summary

In this chapter, a novel image reconstruction algorithm based on enhanced adaptive group sparsity with total variation constraints (EAGS-TV) was proposed. By combining adaptive group sparsity and total variation, the *a priori* information of regional structure features and global characteristics of the conductivity variation were simultaneously utilised. For this goal, an enhanced adaptive pixel grouping algorithm was developed based on Otsu's thresholding method and an accelerated alternating direction method of multipliers was introduced to solve the image reconstruction problem with a faster convergence rate. Superior image qualities were obtained by using EAGS-TV both in simulation studies and phantom experiments. In

comparison with l_1 regularisation, TV regularisation and AGS, it was concluded that EAGS-TV was a more effective algorithm for high resolution conductivity imaging.

The application of EAGS-TV in high resolution cell spheroid imaging will be presented in Chapter 7.

Chapter 6 Miniature EIT Sensors and Image Reconstruction for 3D Cell Culture Imaging

6.1 Introduction

This chapter probes the application of EIT in real-time and non-destructive imaging of the 3D cell culture system. The advantageous features of EIT, such as high temporal resolution, accredited spatial resolution, label-free detection and non-destructive sensing capability, are highly desirable for cellular imaging of a 3D cell culture system.

This chapter presents a study of EIT in 3D cell culture imaging from the perspectives of sensor design, characterisation and high quality 3D image reconstruction. Firstly, a planar miniature EIT sensor together with a 3D forward model that, when compared with the 2D one, accords better with electric field distribution, was proposed. Furthermore, a novel 3D-Laplacian and sparsity joint regularisation algorithm for enhanced 3D cell culture imaging was developed. The miniature sensor was designed in consideration of the sensing challenges under practical cell culture environment, e.g. the DC drift under highly conductive cell culture medium, direct contact of cell spheroids with the electrode, and compatibility with the real cell culture dish. The structure, manufacture and modelling of the sensor were demonstrated and its sensitivity was analysed. The performance of the proposed 3D-Laplacian and sparsity joint regularisation algorithm was compared with the 3D Total Variation (3D-TV) regularisation method (Ertas et al., 2013). Finally, both simulations of test phantoms and experiments of breast cancer cells were conducted to verify the performance of the sensor and the 3D image reconstruction method.

6.2 Design and Modelling of the Miniature EIT Sensor

6.2.1 Sensor Design

Figure 6-1 shows the schematic illustration of the designed miniature EIT sensor for 3D cell cultivation imaging. The sensor consists of 16 micro electrodes near the boundary of the base. This electrode configuration is adopted to form easily

an appropriate cell culture dish and to avoid the severe noise caused by the contact impedance between the imaging target, e.g. cell spheroid and the electrode. The inner diameter of the circular chamber is 15 mm and the height is 10 mm. The length and width of each microelectrode is 1.2 mm and 0.6 mm, respectively. All the electrodes are distributed evenly on the substrate. Furthermore, in order to reduce the DC drift of the measurement, caused by the highly conductive cell culture medium, a grounded point with a diameter of 0.4 mm is integrated in the bottom centre of the chamber as a reference electrode. The planar electrodes configuration can generate a 3D electric field near the substrate in the axial direction; this can be used to perform subsurface imaging (Hu and Yang, 2010).

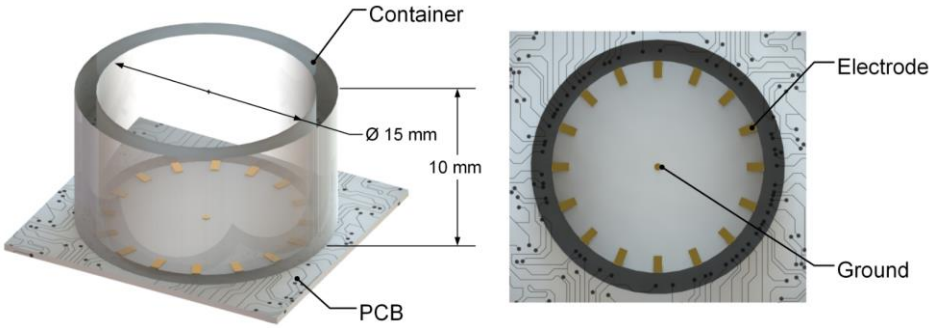

Figure 6-1 Schematic illustration of the designed miniature EIT sensor.

As shown in Figure 6-2, the planar miniature EIT sensor was manufactured on a printed circuit board. After gold plating, rectangular bonding pads were used as sensing electrodes to prevent corrosion by the solution and electrochemical reaction. The length of all traces connecting the electrodes and sensor socket was equalized to minimise the difference in impedance caused by trace length discrepancy.

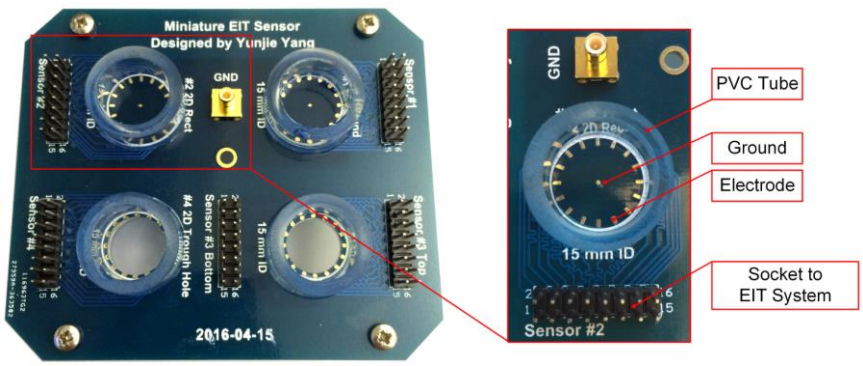

Figure 6-2 Schematic illustration of the designed miniature EIT sensor.

6.2.2 3D Modelling and Sensitivity Analysis

The formerly reported work (Sun et al., 2010), which used a planar EIT sensor, was based on a conventional 2D model. This did not conform to the actual situation and could introduce errors in the model. Moreover, the 3D imaging ability was not utilised. As illustrated in Figure 6-3, in this work, a 3D model of the designed planar miniature EIT sensor with culture medium was developed in COMSOL Multiphysics in order to reduce modelling error while investigating 3D imaging. To be consistent with practical circumstances, the sensor model was filled up to a height of 3 mm with a background substance. As shown in Figure 6-4, a 3D mesh for the inverse problem was developed, where the illustrated sensing domain is divided longitudinally into 12 layers, and each layer has 32×32 voxels. Consequently, the mesh consists of 9744 voxels in the cylindrical sensing domain. Accordingly, the 3D Jacobian matrix can be calculated as follows:

$$\mathbf{J}_{dm}(t,z,q)=\frac{\partial \mathrm{V}_{dm}}{\partial \sigma_k}=-\int_{\text{voxel } k}\nabla \mathrm{u}_{tzq}\left(I^{d}\right)\cdot\nabla \mathrm{u}_{tzq}\left(I^{m}\right)\mathrm{dV} \tag{6.1}$$

where $\mathbf{J}_{dm}(t, z, q)$ is the sensitivity value at voxel (t, z, q) when electrode pairs d and m are selected as current excitation and measurement, respectively, where $1\leq t \leq 32$, $1\leq z \leq 32$, $1\leq q \leq 12$. $\mathrm{U}_{tzq}(I^d)$ and $\mathrm{U}_{tzq}(I^m)$ are electrical potential within the 3D sensing region when the d^{th} and m^{th} pair of electrodes are selected as current excitation electrodes, respectively. In this work, the adjacent sensing protocol (Brown and Seagar, 1987) was adopted; this generates 104 independent measurements in a completed scan.

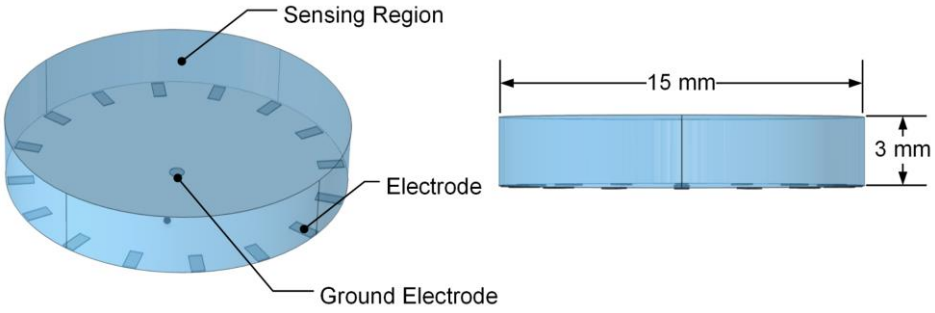

Figure 6-3 The modelled planar miniature EIT sensor.

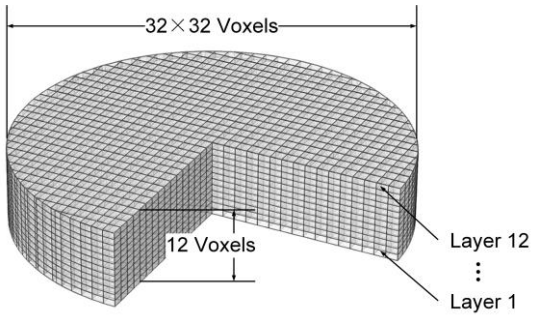

Figure 6-4 Voxel mesh for inverse problem calculation.

Figure 6-5 illustrates the cross sectional distribution of the summation of the Jacobian matrix. The summation indicates the sensitivity of the designed miniature EIT sensor. The miniature sensor has the largest sensitivity to at the bottom layer and reduces gradually towards the top layers. However, within the oblate sensing region, i.e. 3 mm of chamber height, the sensitivity is large enough for performing 3D imaging.

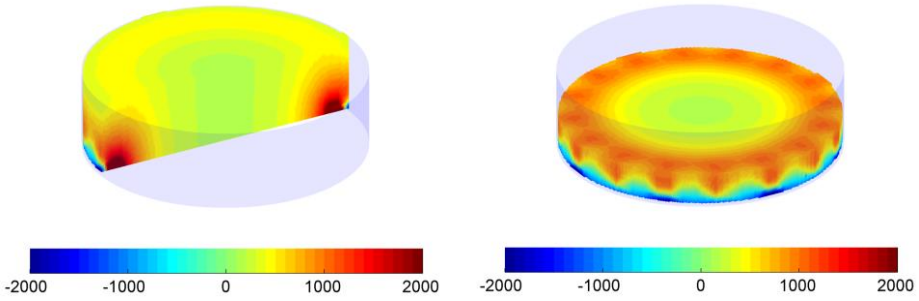

(a) (b)

Figure 6-5 Summation of the Jacobian matrix. (a) Longitudinal section. (b) Transverse section.

6.3 3D Image Reconstruction Algorithm

Conductivity distribution in the sensing region can be estimated based on the voltage measurement and the 3D Jacobian matrix by using certain image reconstruction algorithms. In this section, a novel 3D-Laplacian and sparsity joint regularisation algorithm was proposed specifically for enhanced 3D cell culture imaging on the designed sensor. In addition, the 3D-TV method was also presented for comparative purposes.

6.3.1 3D-Laplacian and Sparsity Joint Regularisation

In this subsection, a novel 3D-Laplacian and sparsity joint regularisation (3D-Lap-l_1) algorithm was presented for enhanced 3D cell culture imaging on the designed miniature sensor. In this context, the sparsity constraint and 3D-Lapalacian operator are combined together to deal with the ill-posed 3D EIT image reconstruction problem of the designed sensor. As shown in Figure 6-6, the 3D-Laplacian operator imposes a constraint on the vertical and horizontal directions for enhanced 3D positioning, while the sparsity constraint introduces the sparse prior and excellent noise reduction performance. The combination of both terms exhibits the features of both terms. The algorithm is formulated as follows:

$$\Delta\boldsymbol{\sigma}_{\text{3D-Lap-}l_1} = \arg\min_{\Delta\boldsymbol{\sigma}} \left\{ \frac{1}{2} \left\| \mathbf{J}\Delta\boldsymbol{\sigma} - \Delta\mathbf{V} \right\|_2^2 + \lambda_1 \left\| \mathbf{L}\Delta\boldsymbol{\sigma} \right\|_2^2 + \lambda_2 \left\| \Delta\boldsymbol{\sigma} \right\|_1 \right\} \tag{6.2}$$

where, $\Delta\boldsymbol{\sigma}_{\text{3D-Lap-}l_1}$ denotes the estimation of the true conductivity distribution; λ_1 and λ_2 are regularisation factors of the 3D-Laplacian term and the sparsity term, respectively; $\mathbf{L}$ is the 3D-Laplacian operator matrix (Yang et al., 2014), which can be calculated readily based on the definition illustrated in Figure 6-6 as:

$$\mathbf{L} = \begin{bmatrix} 3 & -1 & \cdots & 0 \\ -1 & 6 & \cdots & 0 \\ & & \ddots & \\ 0 & 0 & \cdots & 3 \end{bmatrix} \in \mathrm{R}^{n \times n} \tag{6.3}$$

where, n is the total number of voxels, i.e. 9744 in this work.

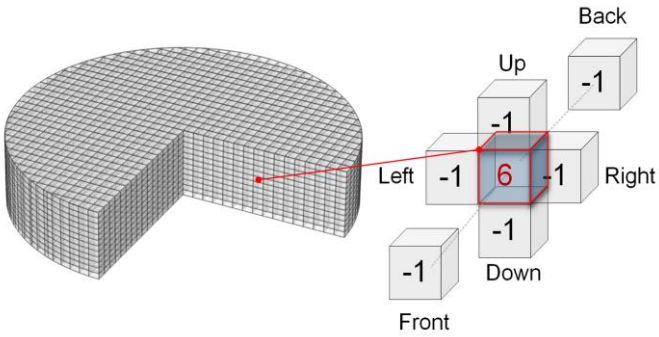

Figure 6-6 3D Laplacian operator applied to a voxel.

Equation (6.2) can be rewritten easily as:

$$\Delta\boldsymbol{\sigma}_{\text{3D-Lap-}l_1} = \arg\min_{\Delta\boldsymbol{\sigma}} \left\{ \frac{1}{2} \left\| \begin{bmatrix} \Delta\mathbf{V} \\ 0 \end{bmatrix} - \begin{bmatrix} \mathbf{J} \\ \sqrt{\lambda_1}\mathbf{L} \end{bmatrix} \Delta\boldsymbol{\sigma} \right\|_2^2 + \lambda_2 \left\| \Delta\boldsymbol{\sigma} \right\|_1 \right\} \tag{6.4}$$

For simplicity, (6.4) can be rewritten further as:

$$\hat{\mathbf{x}} = \arg\min_{\mathbf{x}} \left\{ \frac{1}{2} \left\| \mathbf{b} - \mathbf{A}_{\lambda_1} \mathbf{x} \right\|_2^2 + \lambda_2 \left\| \mathbf{x} \right\|_1 \right\} \tag{6.5}$$

where

$$\mathbf{b} = \begin{bmatrix} \Delta\mathbf{V} \\ 0 \end{bmatrix}; \quad \mathbf{A}_{\lambda_1} = \begin{bmatrix} \mathbf{J} \\ \sqrt{\lambda_1}\mathbf{L} \end{bmatrix}; \quad \mathbf{x} = \Delta\boldsymbol{\sigma} \tag{6.6}$$

The optimisation problem in (6.5) with nonquadratic convex regularizer was solved by a Two-step Iterative Shrinkage/Thresholding Algorithm (TwIST) (Bioucas-Dias and Figueiredo, 2007); it exhibits fast convergence rates for ill-conditioned problems. The iteration framework is expressed as:

$$\begin{cases} \hat{\mathbf{x}}_1 = \Psi_\mu\left(\hat{\mathbf{x}}_0\right) \\ \hat{\mathbf{x}}_{k+1} = \left(1-\alpha\right)\hat{\mathbf{x}}_{k-1} + \left(\alpha-\delta\right)\hat{\mathbf{x}}_k + \delta\cdot\Psi_\mu\left(\hat{\mathbf{x}}_k\right) \end{cases} \tag{6.7}$$

where, $\mathbf{x}_{k+1}$ and $\mathbf{x}_k$ are the estimation of conductivity distribution at the k+1 and k step ($k \geq 1$) respectively; $\mathbf{x}_0$ is the initial value, which is calculated by (2.13) in Chapter 2; α, $\delta > 0$ are parameters and:

$$\Psi_\mu\left(\mathbf{x}\right) = \Gamma_\mu\left(\mathbf{x} + \mathbf{A}_{\lambda_1}^{\mathrm{T}}\left(\mathbf{b} - \mathbf{A}_{\lambda_1}\mathbf{x}\right)\right) \tag{6.8}$$

where $\mu = \lambda_2$ is the regularisation parameter. Γ_μ is the denoising function and in this case is the well-known soft-thresholding function (Donoho, 1995), which is expressed as:

$$[\cdots, sign(x_i)\cdot \max\{0, |x_i| - \mu\}, \cdots] = \Gamma_{\mu}([\cdots, x_i, \cdots]) \tag{6.9}$$

where x_i is the i^{th} element of $\mathbf{x}$ and *sign* is the sign function.

6.3.2 3D Total Variation Regularisation

For comparative purposes, the 3D-TV method (Ertas et al., 2013) was also implemented for 3D image reconstruction; it is formulated as:

$$\Delta\boldsymbol{\sigma}_{\text{3D-TV}} = \arg\min_{\Delta\boldsymbol{\sigma}} \left\{ \frac{1}{2} \left\| \mathbf{J}\Delta\boldsymbol{\sigma} - \Delta\mathbf{V} \right\|_2^2 + \lambda \left\| \Delta\boldsymbol{\sigma} \right\|_{\text{TV}_{3D}} \right\} \tag{6.10}$$

where, $\Delta\boldsymbol{\sigma}_{\text{3D-TV}}$ denotes the estimation of the true conductivity variation; λ is regularisation factor; and $\|\Delta\boldsymbol{\sigma}\|_{\text{TV3D}}$ is the 3D-TV norm of the conductivity variation distribution, which is defined as:

$$\begin{aligned} \left\| \Delta\boldsymbol{\sigma} \right\|_{\text{TV}_{3D}} &= \sum_{m,k,l} \sqrt{\left(D^{v}_{m,k,l}\Delta\boldsymbol{\sigma} \right)^2 + \left(D^{h}_{m,k,l}\Delta\boldsymbol{\sigma} \right)^2 + \left(D^{n}_{m,k,l}\Delta\boldsymbol{\sigma} \right)^2} \\ &= \sum_{m,k,l} \left| \nabla_{m,k,l}\, \Delta\boldsymbol{\sigma} \right| \end{aligned} \tag{6.11}$$

where, $[m, k, l]$ is the coordinate of a voxel at the $N\times N\times P$ 3D conductivity image $\Delta\boldsymbol{\sigma}$, with $1 \le m \le N$, $1 \le k \le N$ and $1 \le l \le P$. $D^{v}_{m,k,l}\Delta\boldsymbol{\sigma}$, $D^{h}_{m,k,l}\Delta\boldsymbol{\sigma}$ and $D^{n}_{m,k,l}\Delta\boldsymbol{\sigma}$ are the derivatives of $\Delta\boldsymbol{\sigma}$ along vertical, horizontal and normal directions respectively, and each can be expressed as:

$$D^{h}_{m,k,l}\Delta\boldsymbol{\sigma} = \begin{cases} \Delta\boldsymbol{\sigma}_{m,k,l} - \Delta\boldsymbol{\sigma}_{m+1,k,l} & 1 \le m < N \\ 0 & m = N \end{cases} \tag{6.12}$$

$$D^{v}_{m,k,l}\Delta\boldsymbol{\sigma} = \begin{cases} \Delta\boldsymbol{\sigma}_{m,k,l} - \Delta\boldsymbol{\sigma}_{m,k+1,l} & 1 \le k < N \\ 0 & k = N \end{cases} \tag{6.13}$$

$$D^{n}_{m,k,l}\Delta\boldsymbol{\sigma} = \begin{cases} \Delta\boldsymbol{\sigma}_{m,k,l} - \Delta\boldsymbol{\sigma}_{m,k,l+1} & 1 \le l < P \\ 0 & n = P \end{cases} \tag{6.14}$$

The gradient based steepest descent method was applied to solve the optimisation problem depicted in (6.10) iteratively (Yang and Peng, 2013).

6.4 Results and Discussion

In this section, on the basis of simulation and experiment data, 3D image reconstructions were carried out in order to validate the miniature EIT sensor's performance and the proposed 3D image reconstruction algorithm.

6.4.1 Results Based on Simulation Data

To test the 3D imaging performance, six small spheroid phantoms were modelled in the simulation, simulating the cell spheroids along the vertical and horizontal directions. Figure 6-7 shows the top view and side view of the test phantoms established in the simulation based on the sensor model depicted in Figure 6-3. The material of the spheroid is Titanium beta-21S. The diameter of the spheroid is 0.55 mm and the diameter ratio regarding the sensor is 3.2%. In order to be consistent with the cell culture requirements, the simulated background substance has the same conductivity (1.9 $\mathrm{S \cdot m^{-1}}$) with Phosphate Buffer Solution (PBS), which is a common cell culture medium. In order to evaluate quantitatively the image quality, correlation coefficients (CC) as defined by (4.17) (see Chapter 4) was adopted.

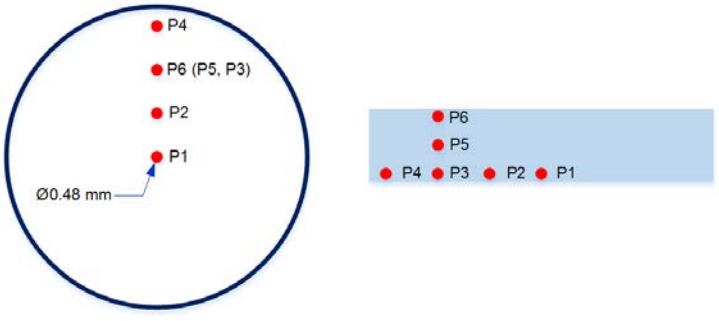

(a) (b)

Figure 6-7 Spheroid phantoms used in 3D imaging tests. (a) Top view. (b) Side view.

Figure 6-8 to Figure 6-13 present the image reconstruction results of the six spheroid phantoms, P1 to P6, from using the proposed 3D-Laplacian and sparsity joint regularisation (3D-Lap-l_1) and the 3D-TV regularisation algorithms. The parameters used in the algorithms, such as the regularisation factor λ, iteration step factor α and maximum iteration number r, are illustrated also in the corresponding figures. Each figure presents both sliced images of each layer and synthesized 3D images. In sliced images, layer 1 corresponds to the bottom layer in Figure 6-4 and, in sequence, layer 12 corresponds to the top layer in Figure 6-4. The synthesized 3D image is the superposition of each layer and scatter interpolation is applied between layers to achieve a smooth illustration. In order to visualise the object more vividly, the isosurface of 90% maximum and minimum conductivity value in the synthesized 3D images are shown.

The simulation results demonstrate that the planar miniature EIT sensor with the proposed 3D image reconstruction algorithms can estimate correctly the conductivity variations in the vertical and horizontal directions of the 3D sensing domain. When comparing the results, the 3D-Lap-l_1 algorithm demonstrates explicitly better image quality, superior noise reduction performance and more accurate location estimation. By using 3D-Lap-l_1, the reconstructed images have also, higher correlation coefficients when compared with those using the 3D-TV method.

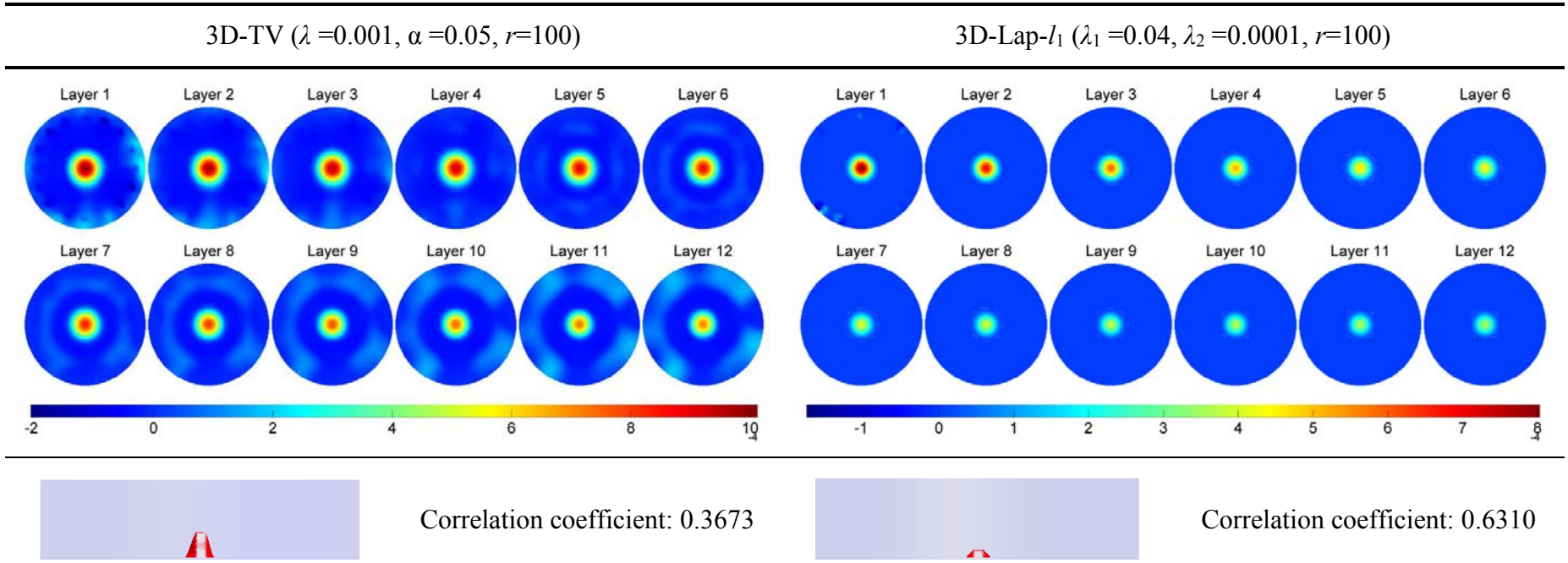

Figure 6-8 Reconstructed images of spheroid phantom P1. The second row shows the sliced images of each layer the third row shows the synthesized 3D images.

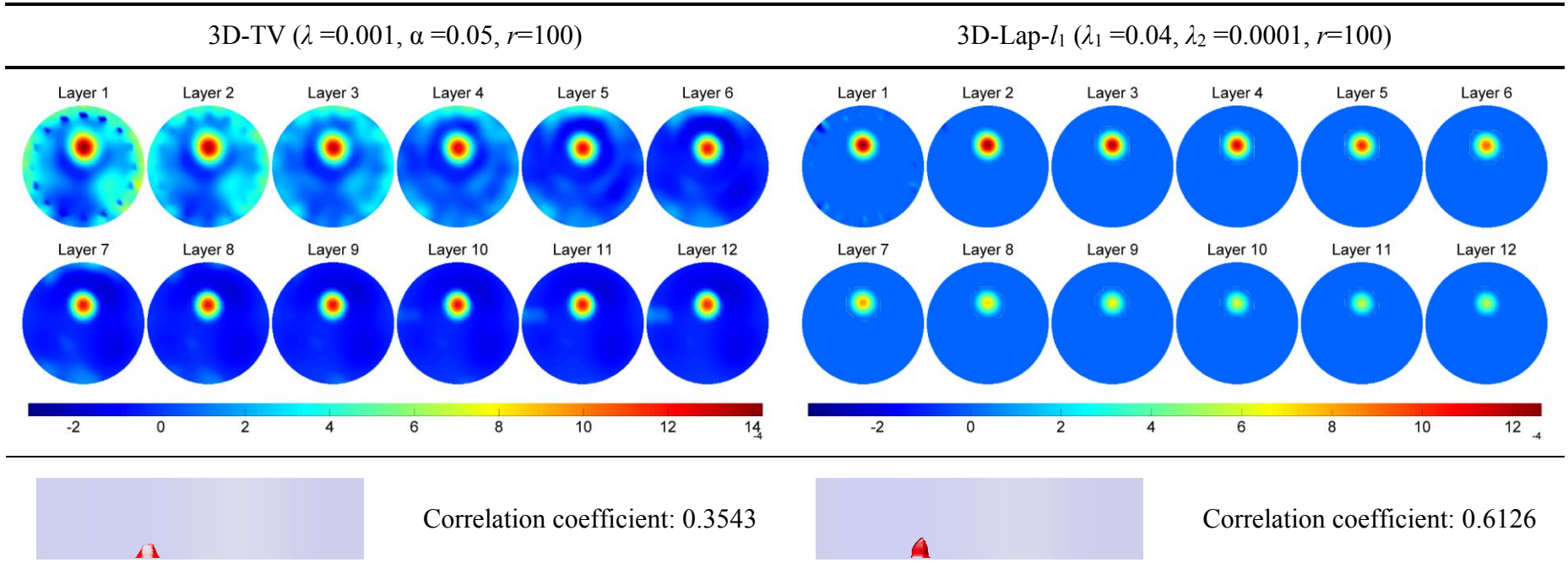

Figure 6-9 Reconstructed images of spheroid phantom P2. The second row shows the sliced images of each layer the third row shows the synthesized 3D images.

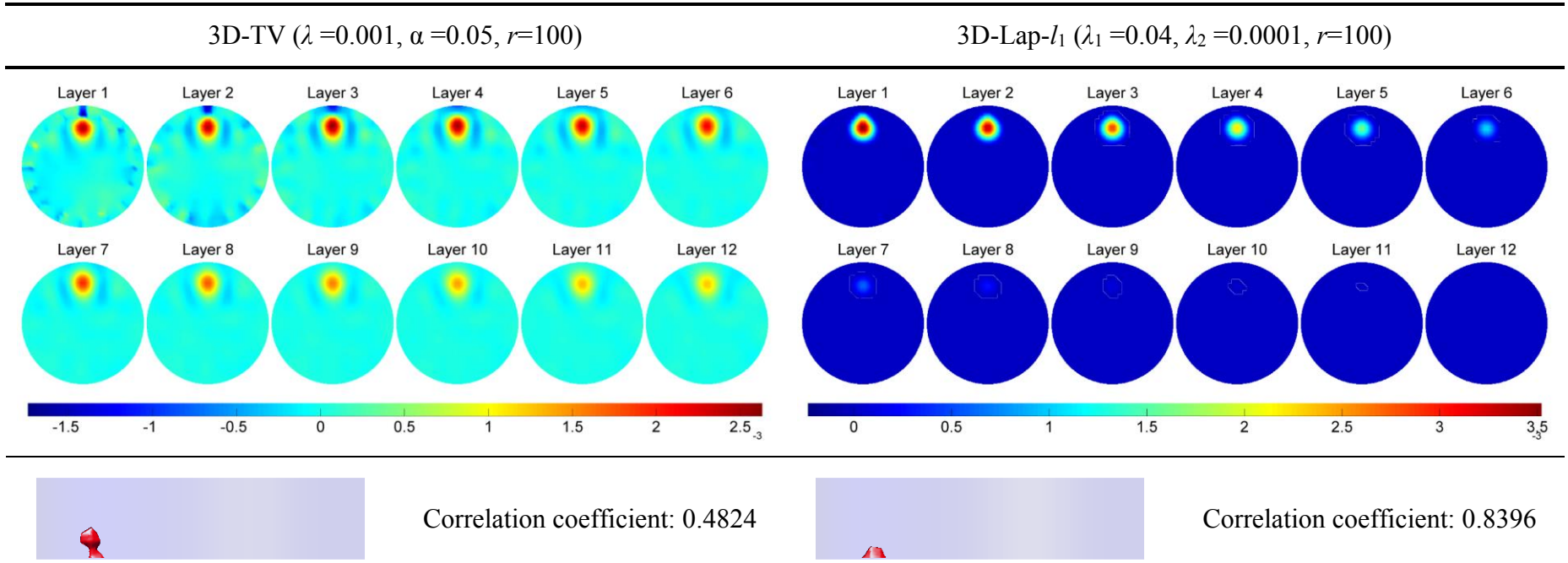

Figure 6-10 Reconstructed images of spheroid phantom P3. The second row shows the sliced images of each layer the third row shows the synthesized 3D images.

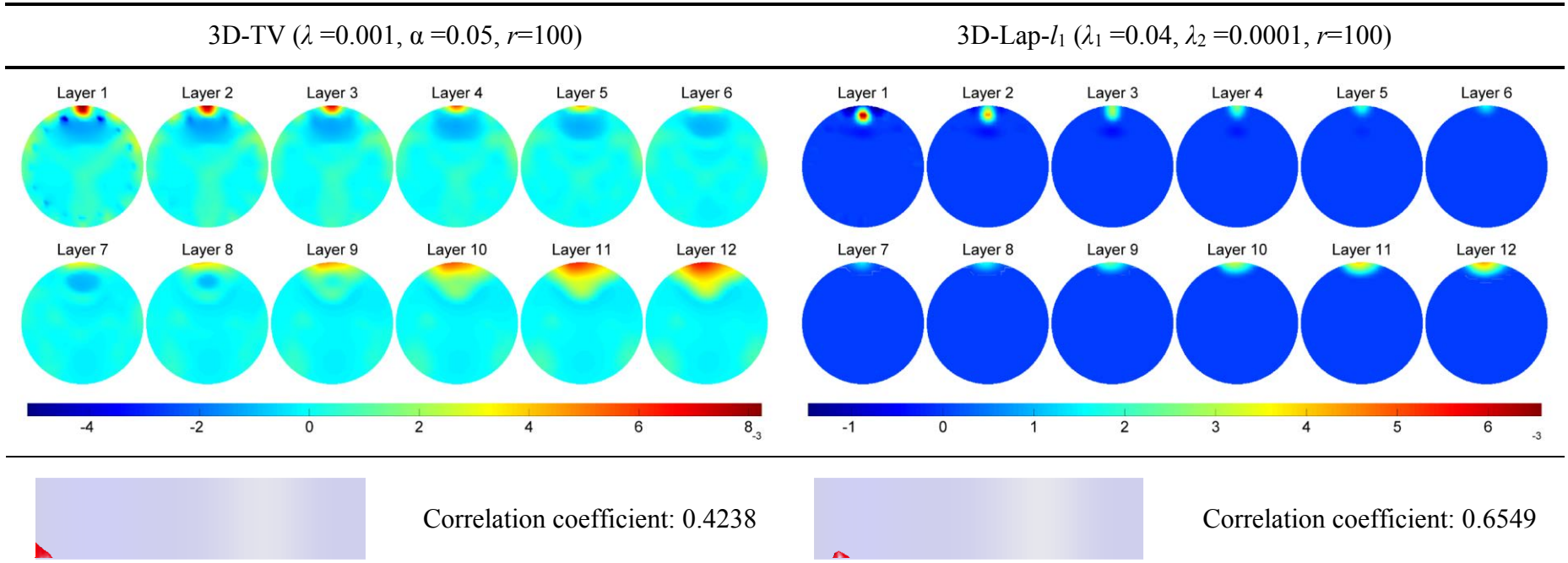

Figure 6-11 Reconstructed images of spheroid phantom P4. The second row shows the sliced images of each layer the third row shows the synthesized 3D images.

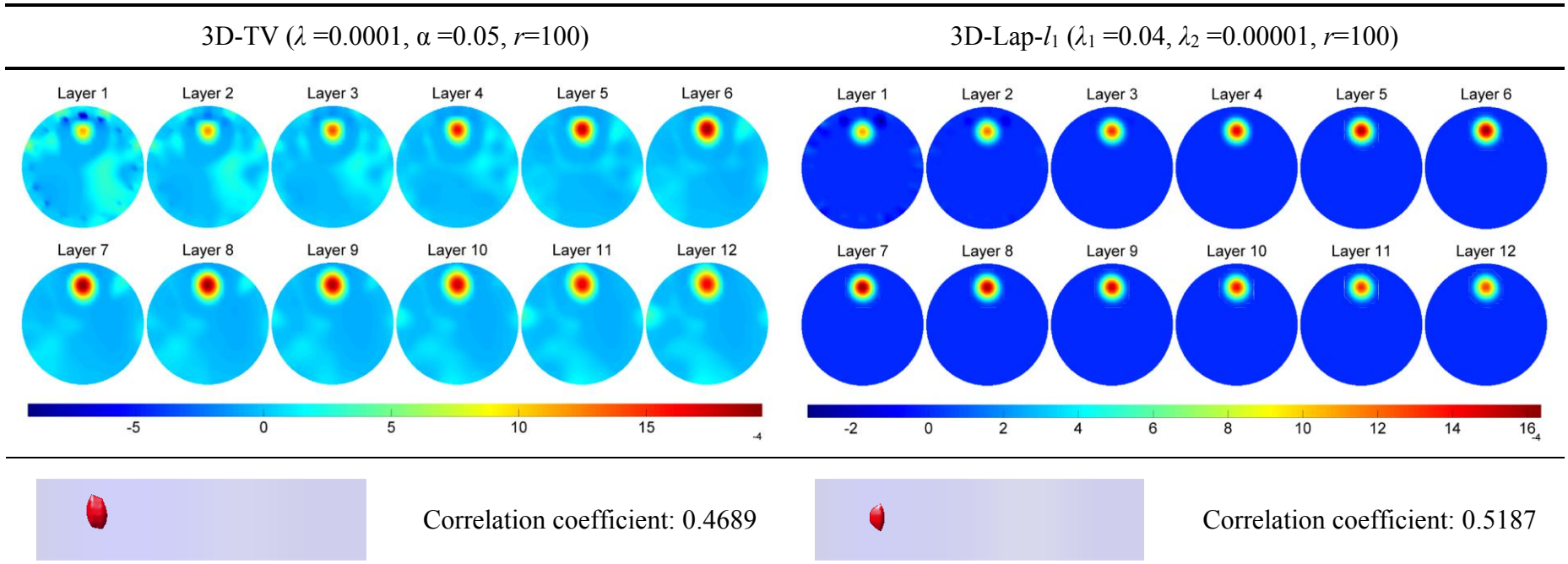

Figure 6-12 Reconstructed images of spheroid phantom P5. The second row shows the sliced images of each layer the third row shows the synthesized 3D images.

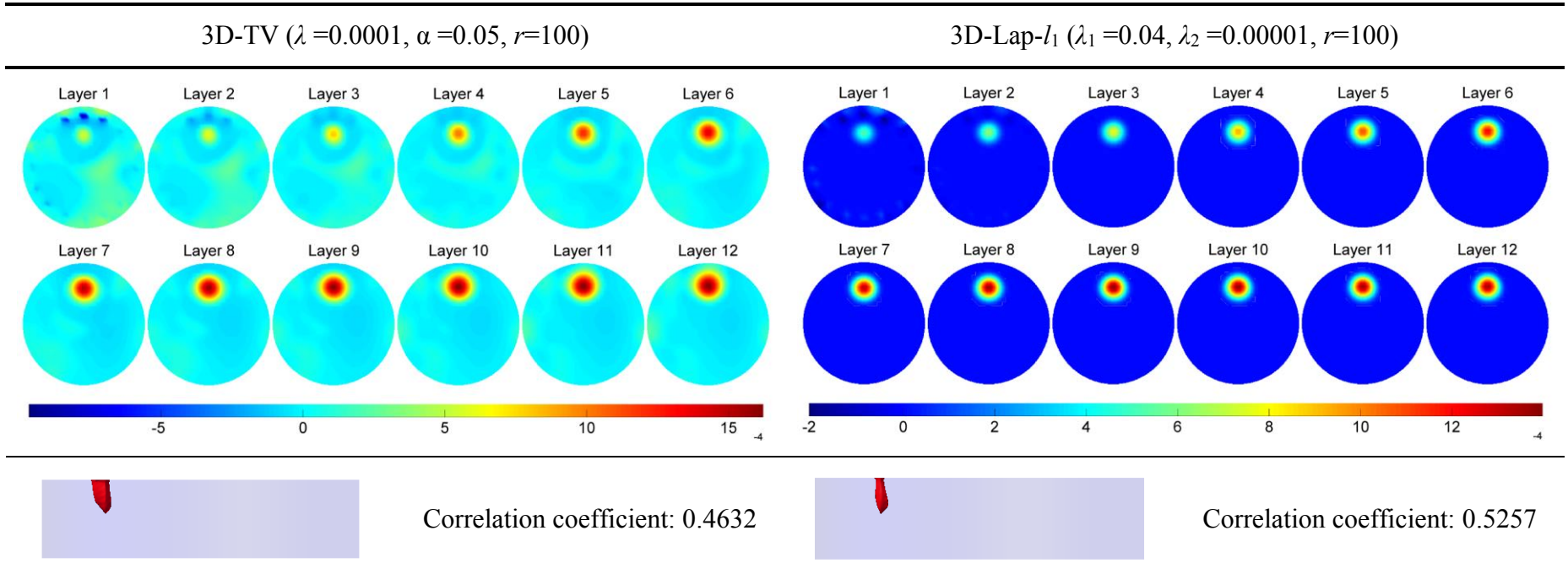

Figure 6-13 Reconstructed images of spheroid phantom P6. The second row shows the sliced images of each layer the third row shows the synthesized 3D images.

6.4.1 Results Based on Experimental Data

3D cell culture imaging using EIT is challenging due to the small dimension of the sensor, highly conductive cell culture medium (approximately 2.0 $S \cdot m^{-1}$ or higher), and weak conductivity variation caused by cellular dynamics. In this section, static imaging on human breast cancer cell spheroids (MCF-7) and triangular pellet were carried out in order to validate the sensor's performance and the proposed 3D image reconstruction algorithm.

Figure 6-14 shows the experimental setup. The mfEIT system, demonstrated in Chapter 3, was utilised in the experiments. The cell culture medium, i.e. PBS, was chosen as the background substance. The conductivity of PBS was measured to be 1.9 $S \cdot m^{-1}$. The frequency of current excitation was selected as 10 kHz and the amplitude of current was approximately 1.5 mA peak to peak. The height of PBS in the sensor chamber was controlled to be 3 mm.

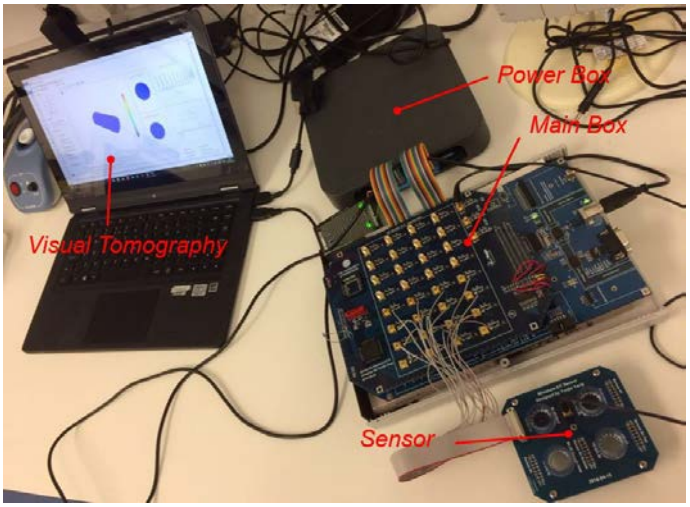

Figure 6-14 Experimental setup in cell imaging experiments.

Two experiment phantoms, i.e. a human breast cancer cell spheroid and a high-density triangular breast cancer cell pellet, were imaged; please see respectively Figure 6-15(b) and Figure 6-15(c). Figure 6-15(a) shows, also, the microscope image of the cell spheroid to be imaged by using the Olympus CK2 Inverted Microscope. The diameter of the cell spheroid is approximately 0.55 mm. For practical reasons,

i.e. to remove cell pellet from centrifuge tube, a 1% agarose gel was cast on top and, as a result, part of the cell pellet was attached to the gel but not mixed together. Gel (agarose) was made with PBS which was the same with the background substance and was seen as transparent by the mfEIT system.

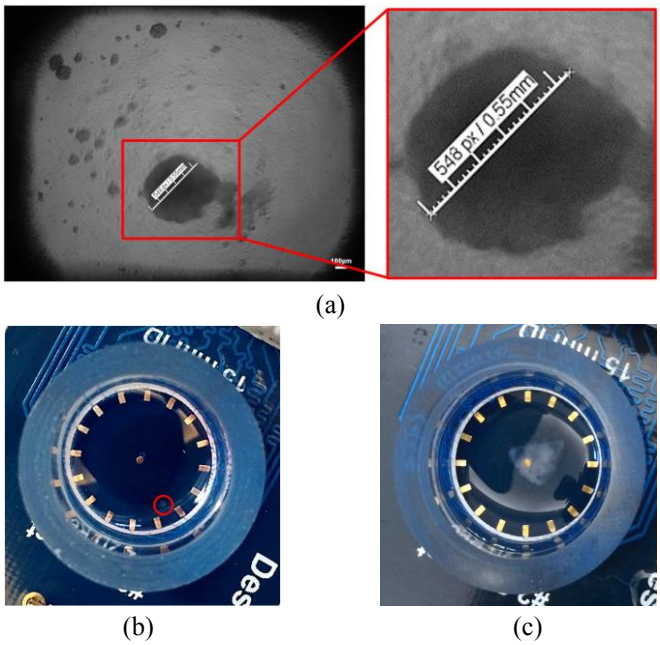

(a)

(b) (c)

Figure 6-15 Experiment phantoms. (a) Microscope image of the cell spheroid. (b) Phantom 1: cell spheroid with 0.55 mm diameter. (c) Phantom 2: triangular cell pellet.

Figure 6-16 and Figure 6-17 illustrates the measured voltage of all electrode combinations, the sliced reconstruction images of each layer and the synthesized 3D images of the two tested phantoms, respectively. In addition, algorithm parameters, used in the reconstruction procedures, are presented also in these figures.

With respect to phantom 1 in Figure 6-16, the diameter ratio of the spheroid and the sensor is 3.7%; this makes the measurement and image reconstruction challenging. As indicated by Figure 6-16, the percentage change of the measured voltage due to the presence of the cells is smaller than 2%. By using the proposed algorithm, i.e. 3D-Lap-l_1, the reconstruction results demonstrate more accurate object position and better noise reduction performance in comparison with the 3D-TV algorithm.

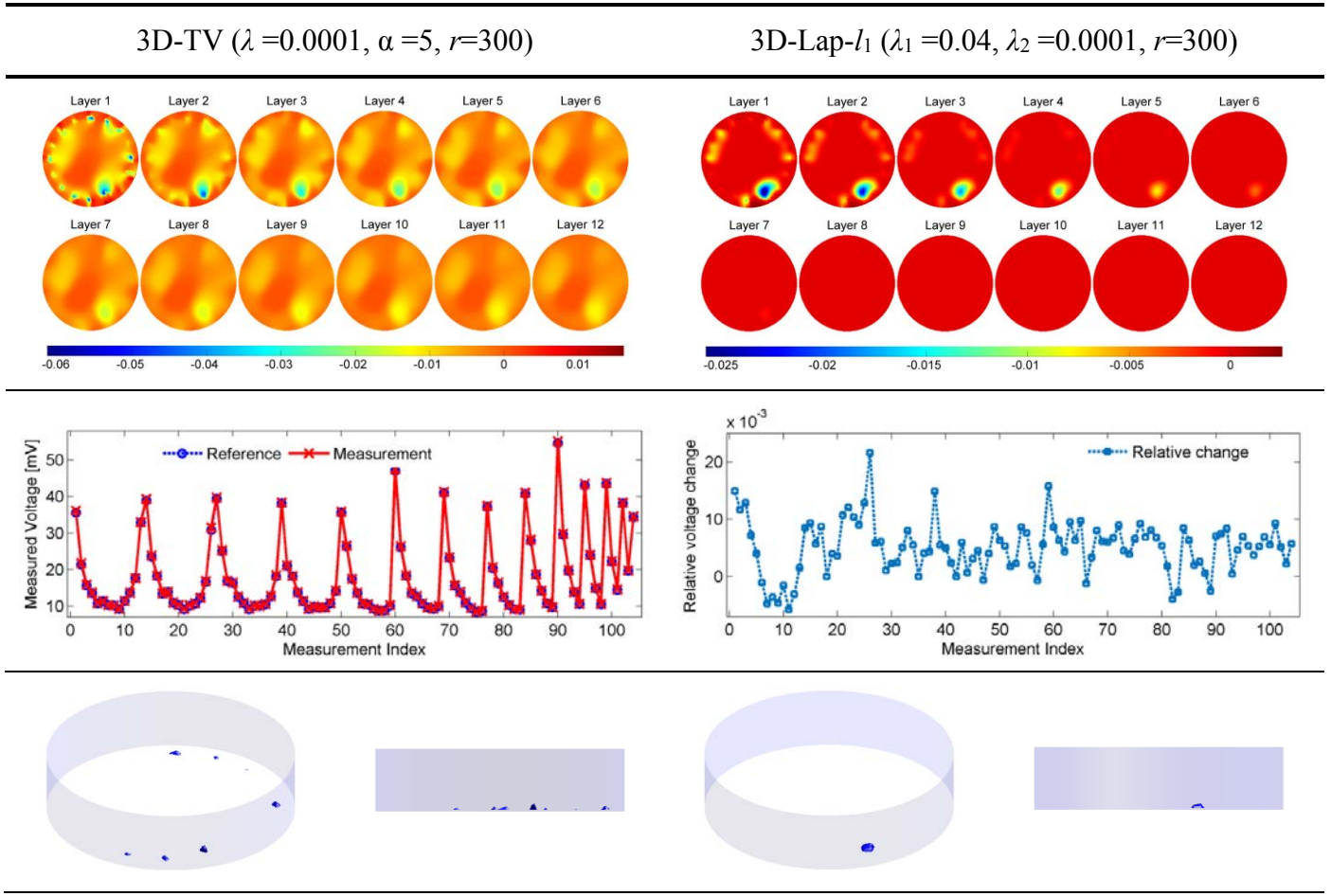

Figure 6-16 Reconstructed images of cell spheroid, phantom 1. The first row shows the sliced images of each layer; the second row shows the measurement voltage and relative voltage change; the third row shows the synthesized 3D images.

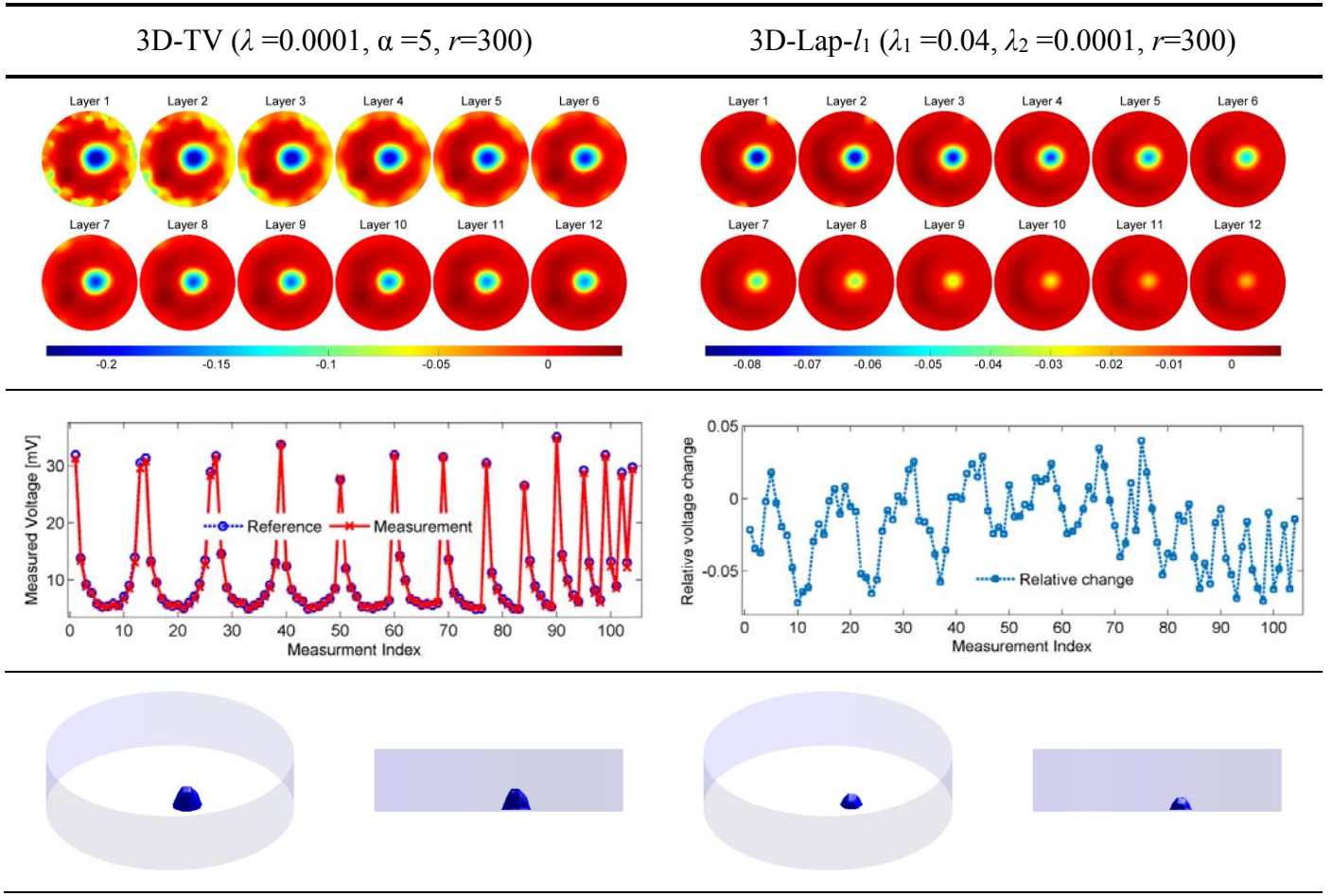

Figure 6-17 Reconstructed images of triangular cell pellet, phantom 2. The first row shows the sliced images of each layer; the second row shows the measurement voltage and relative voltage change; the third row shows the synthesized 3D images.

With regard to phantom 2 in Figure 6-17, i.e. triangular cell pellet, the length of each side of the trilateral is around 4.2 mm, 3.6 mm, and 4.5 mm respectively. As can be seen from Figure 6-17, the relative voltage change in this case is smaller than 5%. The sliced images demonstrate that the proposed 3D-Lap-l_1 method incurs much less noise near the bottom of the sensor when compared with the 3D-TV algorithm. Furthermore, the 3D-Lap-l_1 method illustrates better 3D imaging ability on the vertical direction in terms of position estimation.

In summary, the experiment results verified the feasibility of using the designed miniature EIT sensor and 3D image reconstruction algorithm to perform high quality 3D cellular imaging. By using the proposed 3D-Lap-l_1 algorithm, a significant improvement of image quality has been obtained.

6.5 Summary

This chapter focused on the systematic study of applying EIT to image and monitor 3D cell culture systems. To this end, a planar miniature EIT sensor for subsurface imaging was firstly designed and characterized. Then a novel 3D-Laplacian and sparsity joint regularisation algorithm was proposed for enhanced 3D imaging while a 3D Total Variation regularisation algorithm was adopted for comparative purposes. Finally, simulation and experimental studies were performed.

Simulation indicated that the planar miniature EIT sensor could measure the voltage changes induced by conductivity changes at horizontal and vertical positions. Particularly, the sensor and 3D image reconstruction algorithm were tested by using the mfEIT system in Chapter 3. A human breast cancer cell spheroid and a triangular cancer cell pellet were imaged, reconstructed, and analysed. Both simulation and experiment results confirmed the improvement of image quality of the proposed algorithm. In conclusion, it was shown that the designed sensor together with the proposed 3D image reconstruction algorithm could produce stable, high quality images for 3D cellular substance imaging. The high image quality achieved in imaging tiny cell spheroids can ensure reliable and accurate analysis of the cell-drug response process in the further study presented in the follow-up chapter.

Chapter 7 Cell Imaging and Cell-Drug Response Monitoring

7.1 Introduction

This chapter presents the experimental studies of cell imaging and real-time cell-drug response monitoring by employing the mfEIT system (see Chapter 3), the AGS algorithm (see Chapter 4), the EAGS-TV algorithm (see Chapter 5), and the miniature EIT sensors with the 3D image reconstruction algorithm (see Chapter 6). In order to facilitate long-term, real-time monitoring of the 3D cell culture process by using the developed techniques, the stability of EIT measurement on the miniature sensor which was filled with cell culture medium was investigated firstly. Furthermore, by using a 2D electrode configuration, cell spheroid imaging was conducted based on the AGS and EAGS-TV algorithms in order to obtain high quality tomographic images. Finally, preliminary experiments on the real-time monitoring of cell-drug response between human breast cancer cells and the anti-cancer drug were carried out and the results were analysed by using the method presented in Chapter 6. Promising conclusion was drawn from the experiments.

7.2 Measurement Stability on the Miniature Sensor

In order to perform real-time, long-term cell culture imaging effectively, a highly stable EIT measurement over a long time period is essential to ensure that the weak physiological signal associated with cellular dynamics can be captured. To assess the mfEIT system's long-term measurement performance under such circumstances, a continuous measurement operation on the miniature EIT sensor was performed for 8 hours using a fixed frequency, 10 kHz, when the sensor was filled with cell culture medium, PBS.

Figure 7-1 presents the setup of the experiment for stability test. The volume of PBS injected into the sensor chamber was 1 millilitre and the conductivity of PBS was measured to be 2 $S \cdot m^{-1}$. During the measurement, a cover glass was applied on the top of the sensor chamber with the intention of avoiding the evaporation of PBS. The data acquisition was conducted at a full speed of 48 fps under the serial mode.

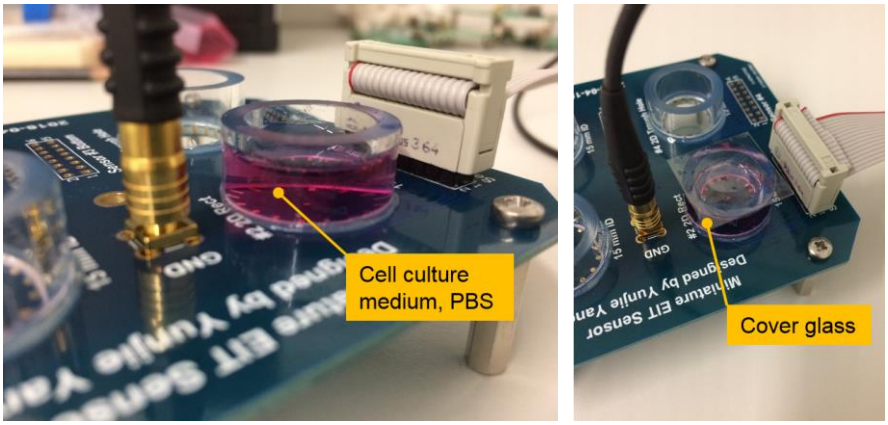

Figure 7-1 Experiment setup for stability test.

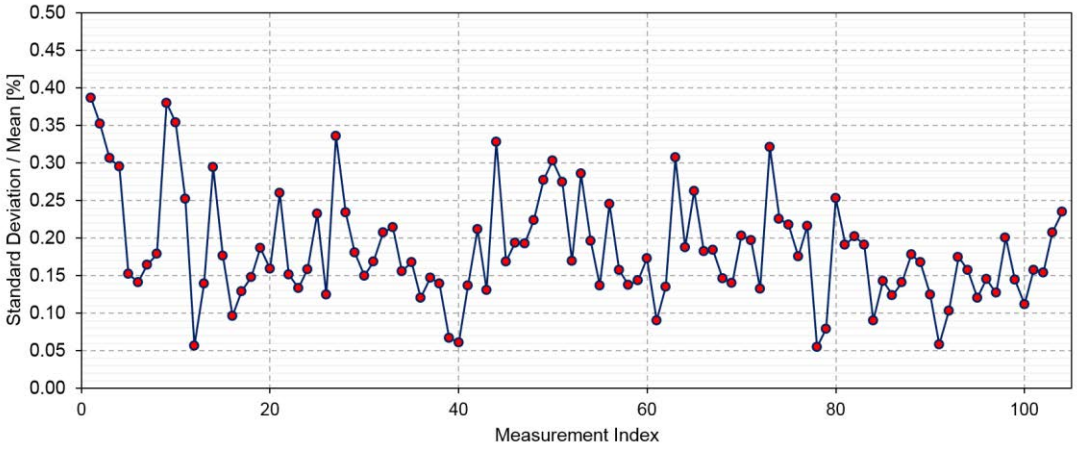

Figure 7-2 Coefficient of variation of the measurements over 8 hours.

Figure 7-2 illustrates the Coefficient of Variation (CV) of 104 measurement channels over 8 hours. The CV value indicates the extent of variability in relation to the average of the measurement. The definition of CV is expressed as:

$$\mathrm{CV} = \frac{s}{\mu} \tag{7.1}$$

where s denotes the standard deviation of the measurement and μ represents the average value of the measurement over a period of time. Figure 7-2 demonstrates that the CV values of all 104 measurement channels range from 0.05% to 0.4%. The result verified that the measurement, obtained from the developed mfEIT system, was stable enough for conducting long-term imaging of a 3D cell culture system.

7.3 Cell Imaging Experiments Using a 2D Sensor

In this section, the performance of AGS (see Chapter 4) and EAGS-TV (see Chapter 5) algorithms on cell imaging was assessed, by using the miniature EIT sensor with a conventional 2D electrode configuration. Figure 7-3(a) illustrates the sensor's schematic. The sensor was especially designed for conducting 2D imaging of a 3D cell culture system. It was manufactured on a PCB substrate (see Figure 6-2 in Chapter 6). The inner diameter of its effective sensing region is 14 mm. Along the circumference there existed 16 gold-coated electrodes which were manufactured based on the half hole process. The height of the sensing region is 1.6 mm and the bottom was sealed with a transparent glass cover in order to enable microscopic observation and meanwhile perform impedance measurement. Figure 7-3(b) presents a picture of the manufactured sensor based on the design shown in Figure 7-3(a).

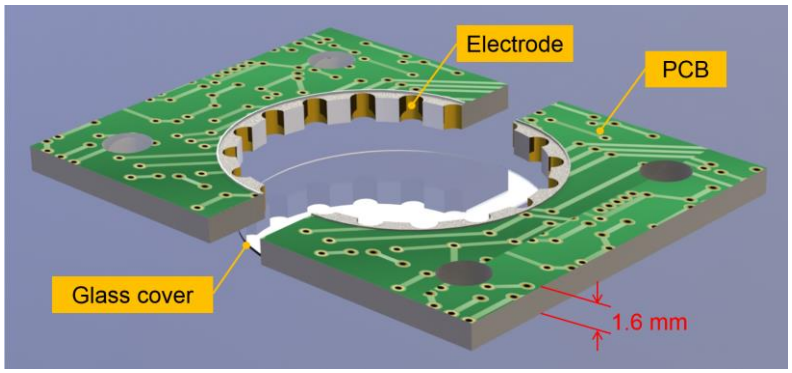

(a)

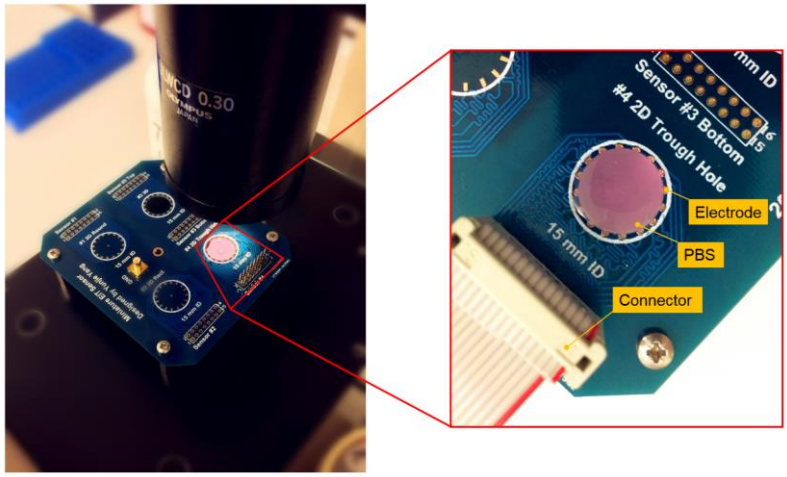

(b)

Figure 7-3 Miniature EIT sensor with a 2D electrode configuration. (a) Schematic of the sensor. (b) The manufactured sensor under microscope.

Figure 7-4 presents two 3D cultured MCF-7 human breast cancer cell spheroids (surrounded by the yellow circles) to be imaged in the experiments. The diameter of each cell spheroid is approximately 2 mm leading to a diameter ratio of 14.29% with respect to the sensor. As illustrated in Figure 7-5, a number of phantom imaging tests were performed. In the experiments, the excitation current's frequency was 10 kHz and its amplitude was approximately 1.5 mA peak to peak. Image reconstruction was performed based on the conventional 2D model by using the l_1 regularisation (see Chapter 2), AGS (see Chapter 4) and EAGS-TV (see Chapter 5) methods. The same setup of algorithm parameters with Chapter 5 were adopted when implementing these algorithms.

Figure 7-4 Two 3D cultured MCF-7 human breast cancer cell spheroids.

(a) (b) (c) (d)

Figure 7-5 Cell imaging test phantoms. (a) Phantom 1. (b) Phantom 2. (c) Phantom 3. (d) Phantom 4.

Figure 7-6 presents the 2D image reconstruction results of four cell spheroid phantoms from l_1 regularisation, AGS, and EAGS-TV methods. The reconstruction results, obtained from l_1 regularisation, present the basic location and shapes of the cell spheroids. However, evident artefacts and deformation of the target objects can

be observed. Apparently, the proposed AGS and EAGS-TV algorithms outperform l_1 regularisation in terms of noise reduction and the estimation accuracy of the targets' shape and location. When comparing the results, conclusion can be drawn that AGS and EAGS-TV can generate high quality tomographic images in practical biomedical scenarios and can be applied readily to 2D imaging of the 3D cell culture system. Note that the asymmetry of two cell spheroids in the reconstructions may be caused by the imperfections of sensor manufacture.

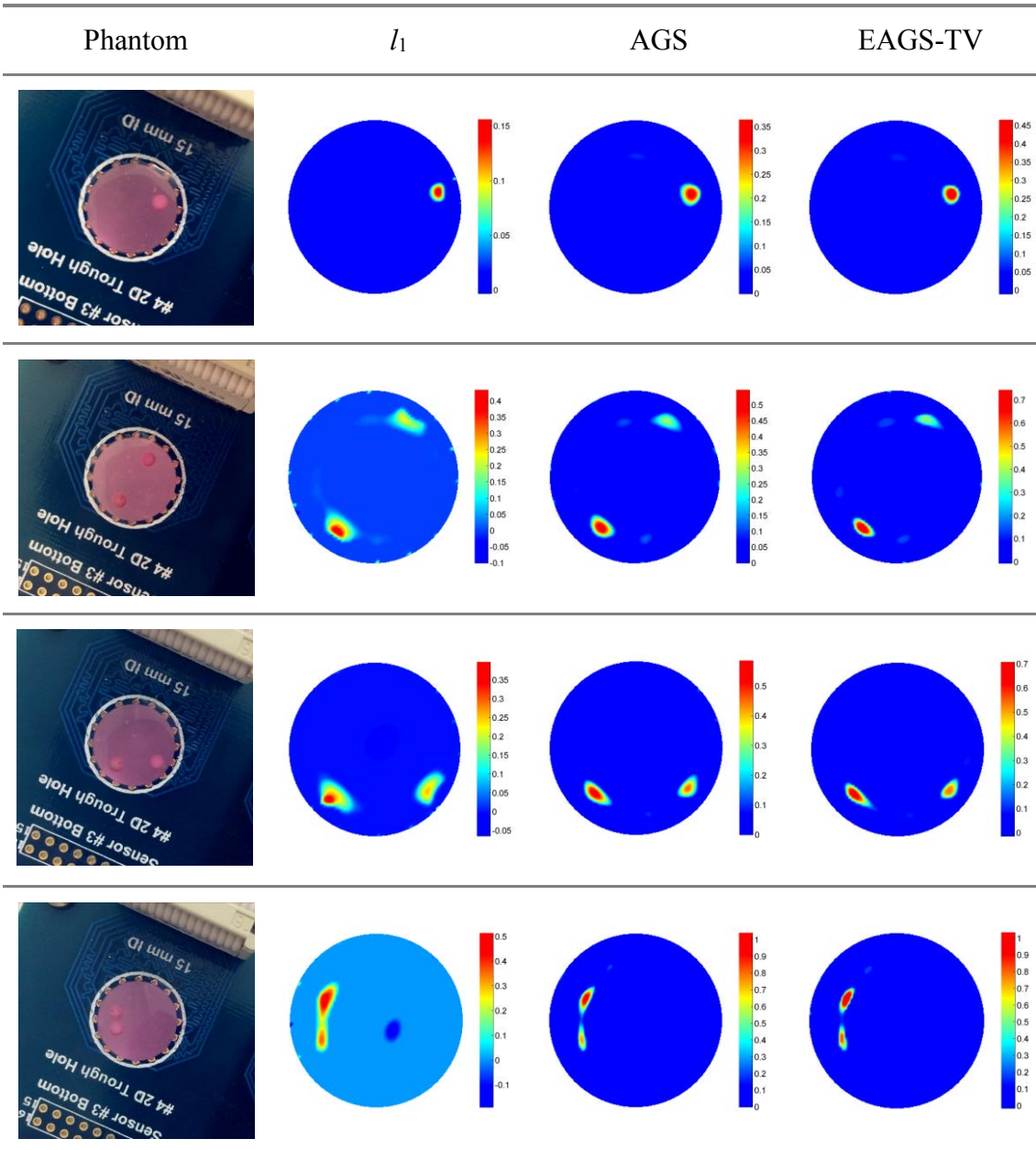

Figure 7-6 Image reconstruction results of cell spheroid phantoms.

7.4 Cell-Drug Response Monitoring — A Preliminary Study

Investigation of cell–drug response is of great significance in drug discovery and pharmaceutical research (Zheng et al., 2013). With attributes to the complicated and time-consuming nature of drug discovery, it is particularly challenging whilst demanded urgently to develop robust, fast, non-destructive and cost-efficient methods to profile potential drugs pharmacologically. In recent years, a number of such researches have focused on cancer cells and monitoring the physiological changes of cells in response to anti-cancer drugs indicated by either spectral characteristics or electrophysiological properties (Jamieson and Byrne, 2017).

In this context, the feasibility of employing EIT in rapid cell-drug response imaging was preliminarily investigated. Specifically, the interaction between MCF-7 human breast cancer cell spheroid and diluted Triton X-100 solution was studied. Triton X-100 was applied commonly to kill the cancer cells by lysing and permeabilizing the membranes of live cells (Koley and Bard, 2010). Experiments were performed on the miniature EIT sensor illustrated by Figure 6-2 of Chapter 6 and measurement were acquired by using the mfEIT system demonstrated in Chapter 3. In the following subsections, the drug diffusion process within cell culture medium is imaged first followed by the real-time imaging results of the cell-drug response process.

7.4.1 Drug Diffusion Process Imaging

When EIT is applied for cell-drug response imaging, only the conductivity variation caused by the drug effect is of interest. However, the addition of drug into the cell culture medium can also lead to the change of conductivity. Therefore, one of the key considerations in interpreting the results is how the drug diffusion process within the cell culture medium will affect the measurements and images. Since Triton X-100 is a non-ionic surfactant (Koley and Bard, 2010), it is necessary to study the conductivity variation of the cell culture medium throughout the drug diffusion process, when only the drug is added. By doing so, the influence of the

drug diffusion process on measurement and image can be assessed and further avoided by optimising the experiment procedure.

Figure 7-7 illustrates the setup of the experiment for drug diffusion process imaging. The volume of the cell culture medium, i.e. PBS in Figure 7-7(a), was 950 microliters and, as presented in Figure 7-7(b), the diluted Triton X-100 solution delivered to the sensor, was 50 microliters.

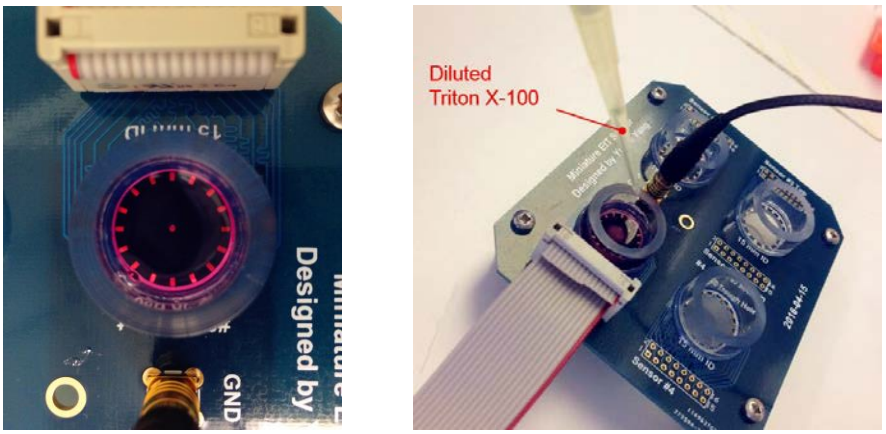

(a) (b)

Figure 7-7 Drug diffusion process imaging experiment setup. (a) Sensor with cell culture medium. (b) Delivery of drugs to the cell culture medium.

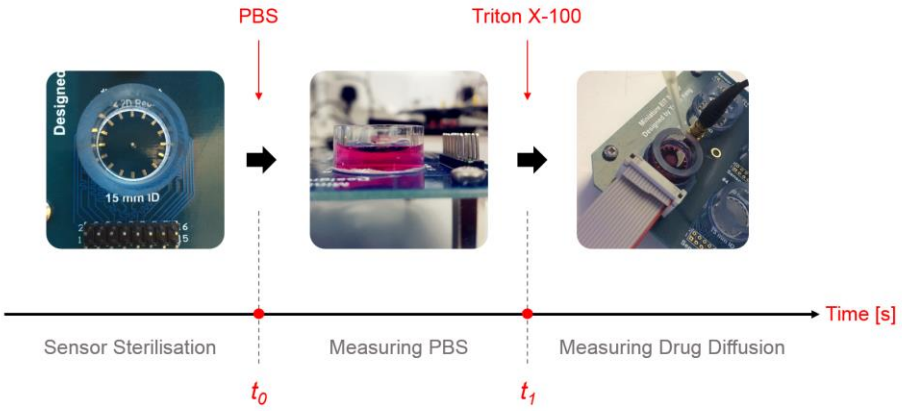

Figure 7-8 Schematic illustration of drug diffusion experiment procedure.

The experiment procedure of imaging drug diffusion is illustrated in Figure 7-8. The sensor was sterilised first and, at time point t_0, PBS was added to the sensor and continuous measurement was started. After a period of time, i.e. at time point t_1,

Triton X-100 was added to the PBS and measurement was recorded continuously for 10 minutes.

3D image reconstructions were conducted in time sequence, based on the 3D model developed in Chapter 6, in order to visualise the drug diffusion process. Considering the fact that the conductivity variation of the diffusion was smooth over time, Tikhonov regularisation (Vauhkonen et al., 1998) was adopted for 3D image reconstruction. Meanwhile, the time sequence of voltage response on the specific electrode pair, which was close to the position of the delivered drug, was analysed.

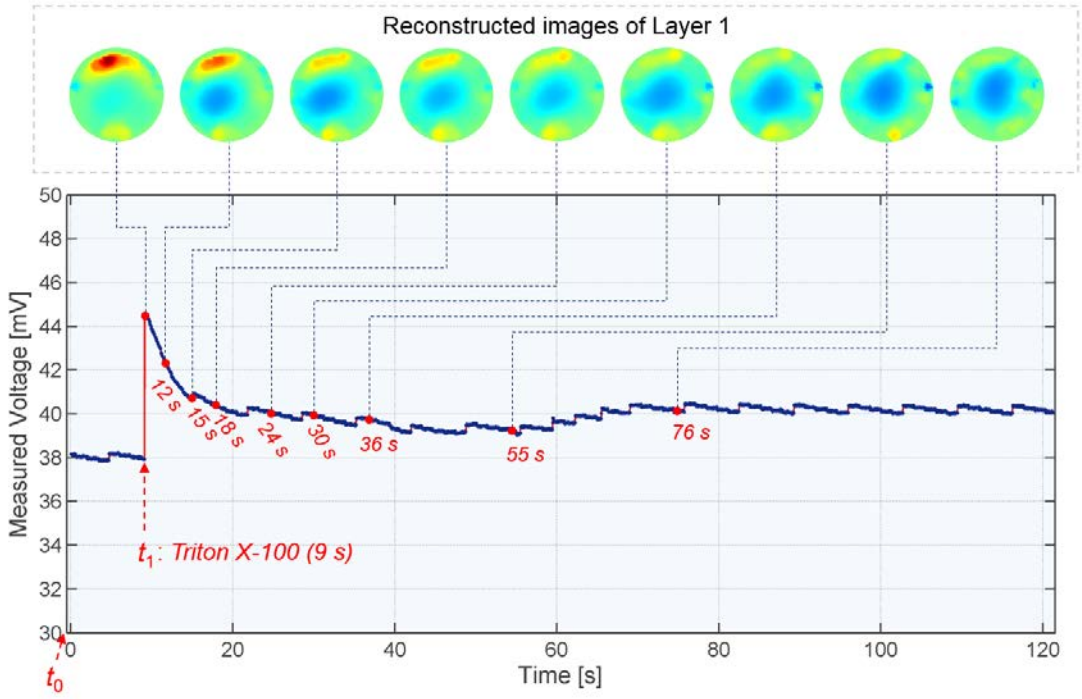

Figure 7-9 Voltage response of the 27th measurement out of 104 measurements over 120 seconds (electrode 3, 4 act as current injection, 5, 6 act as measurement).

Figure 7-9 illustrates the time sequence of voltage response of the 27th measurement over 120 seconds, where the 3rd and 4th electrodes acted as current injection and the 5th and 6th electrodes acted as differential voltage measurement. The reconstructions of layer 1, i.e. the bottom layer, were also presented over time. Since the drug was delivered near the 4th electrode, the response curve in Figure 7-9 is believed to be associated with the variation caused by drug diffusion. At time point t_1, Triton X-100 was delivered and a sudden increase of voltage could be observed.

Then the voltage decreases gradually with the diffusion of the drug. According to Figure 7-9, the diffusion process takes approximately 60 seconds to settle down, when the voltage measurement becomes stable again.

Figure 7-10 presents the 3D reconstructed images based on the measurements taken at the time points labelled in Figure 7-9. The sliced images of each layer are presented where layer 1 and layer 12 correspond respectively to the bottom and the top of the sensing domain, which is described in Figure 6-4 in Chapter 6. The regularisation parameter was 0.01 when image reconstruction was implemented.

Time	Sliced Images
t_0 (0s)	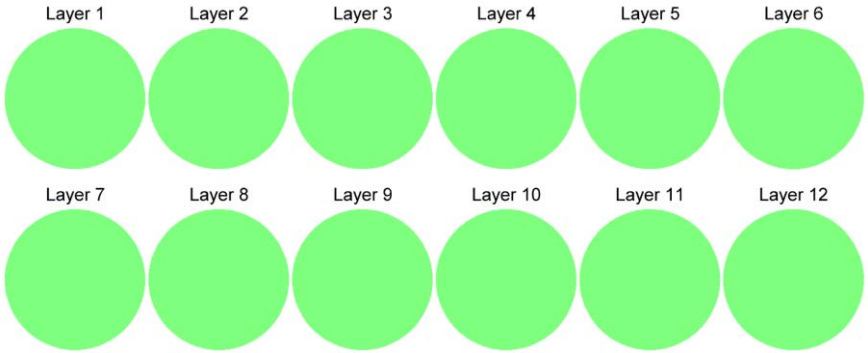
t_1 (9s)	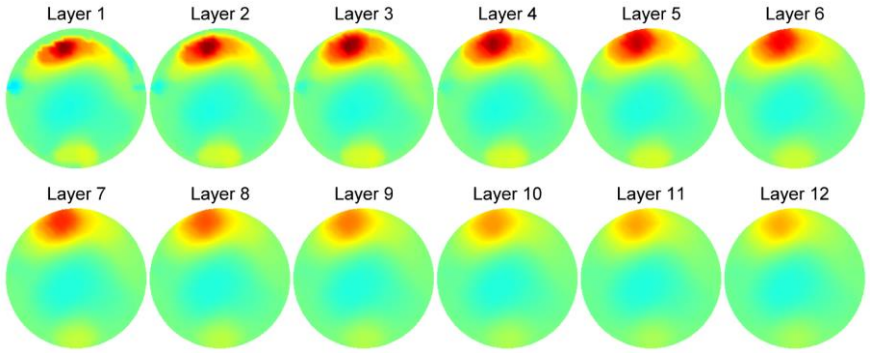
t_1+3s (12s)	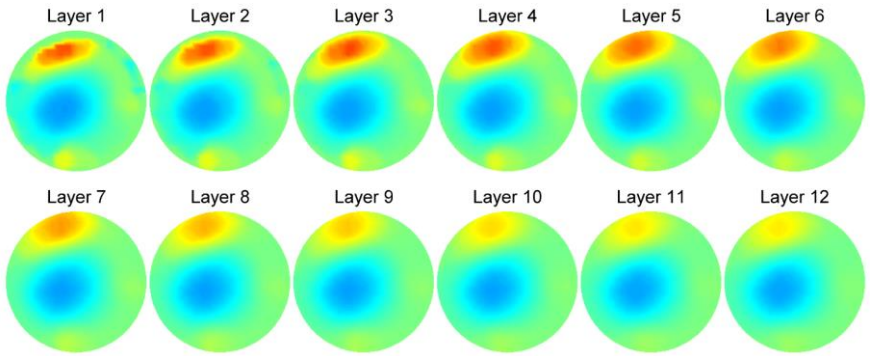

t_1+6s (15s)	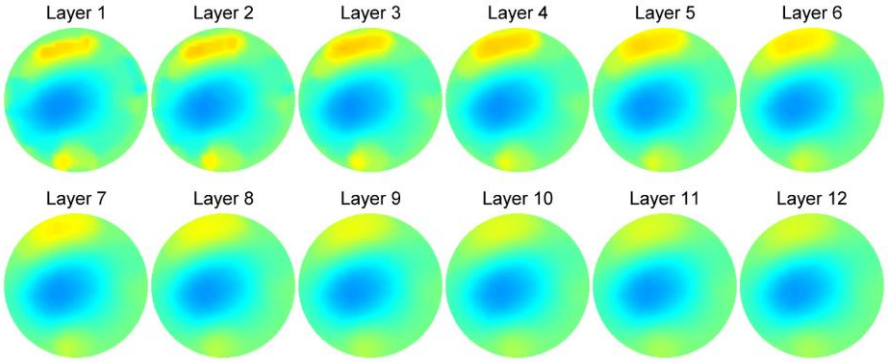
t_1+9s (18s)	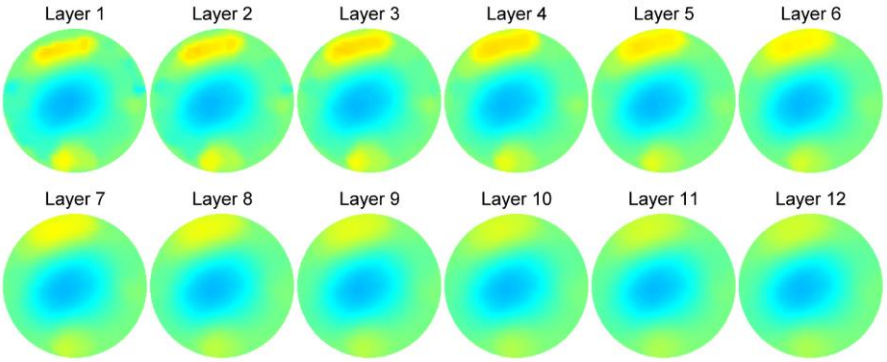
t_1+15s (24s)	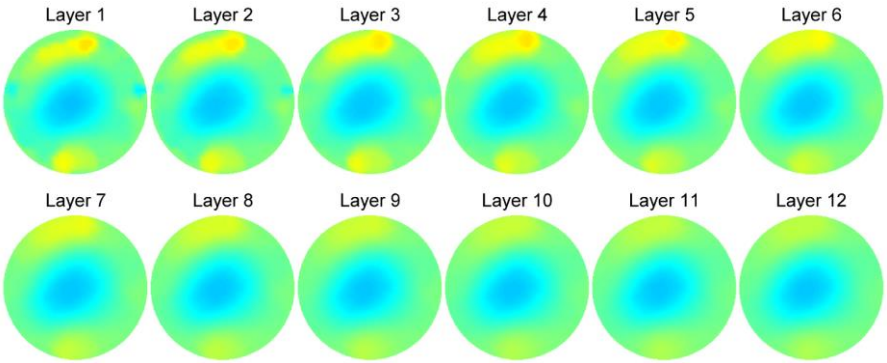
t_1+21s (30s)	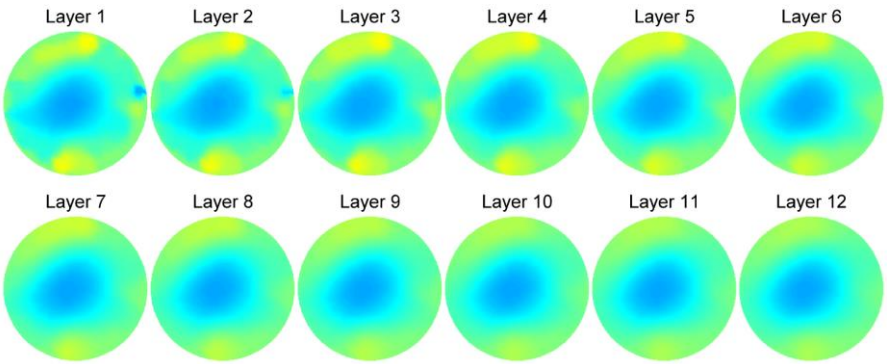

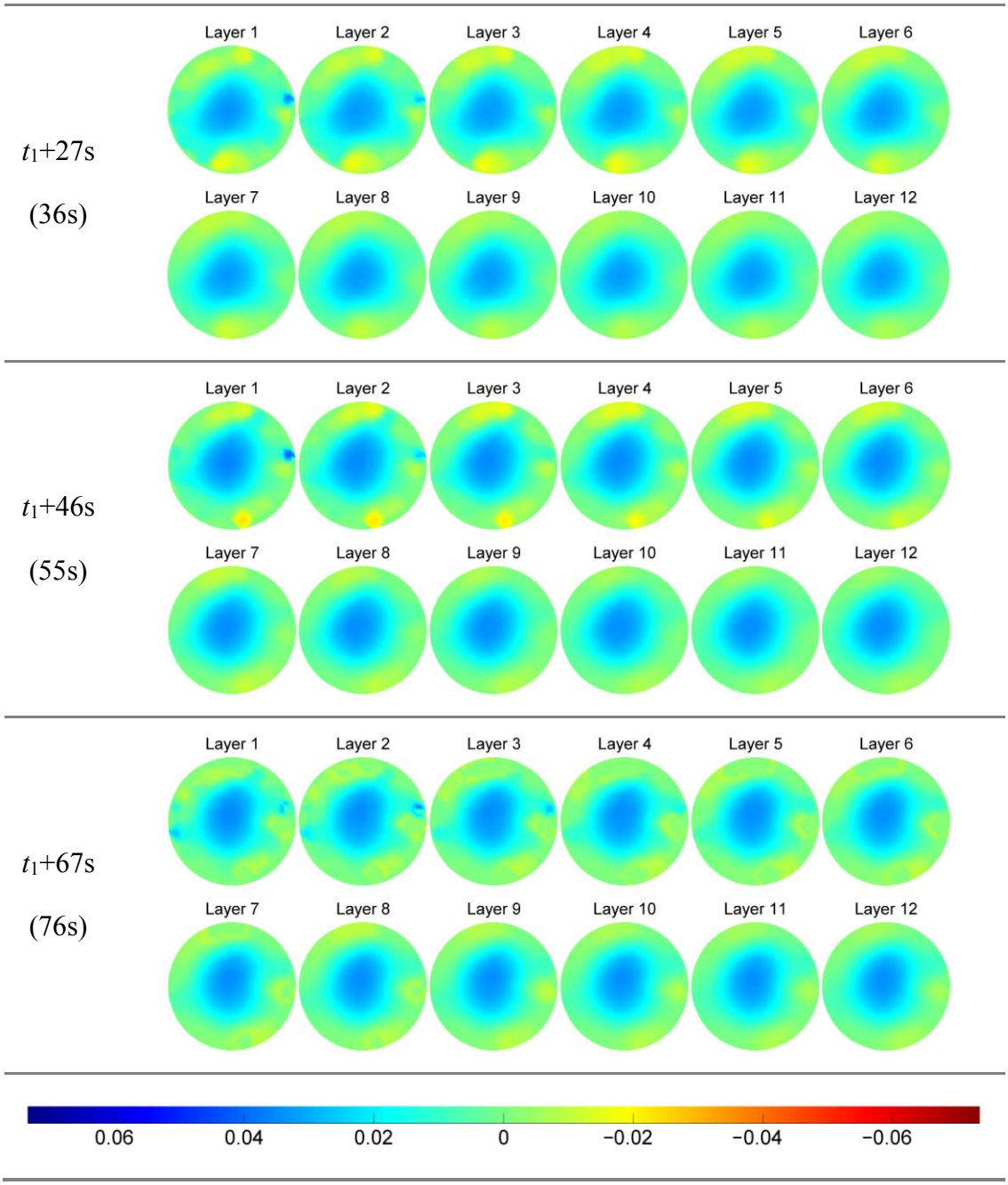

Figure 7-10 Sliced images of drug diffusion process by EIT.

As indicated by Figure 7-10, sequential conductivity variation of all layers associated with the diffusion process can be observed explicitly in the sliced images over time. The position where the drug was delivered demonstrates an evident decrease of conductivity and it vanishes gradually over time. The results suggest that the conductivity variation, caused by the drug diffusion process, may overlap with that caused by the drug effect on cells. Therefore, the experiment procedure of cell-

drug response should be designed carefully in order to avoid the effect of drug diffusion. The next subsection proposes a feasible solution to address this issue.

7.4.2 Cell-Drug Response Monitoring

The process of cell-drug response usually terminates in a few minutes (Koley and Bard, 2010). For a 3D cell culture system, this process cannot be visualised directly by optics based methods, such as microscopy, unless histological section is conducted. Therefore, a robust, fast and non-destructive method to screen such a transient process is demanded urgently for efficiency improvement and cost reduction of drug discovery.

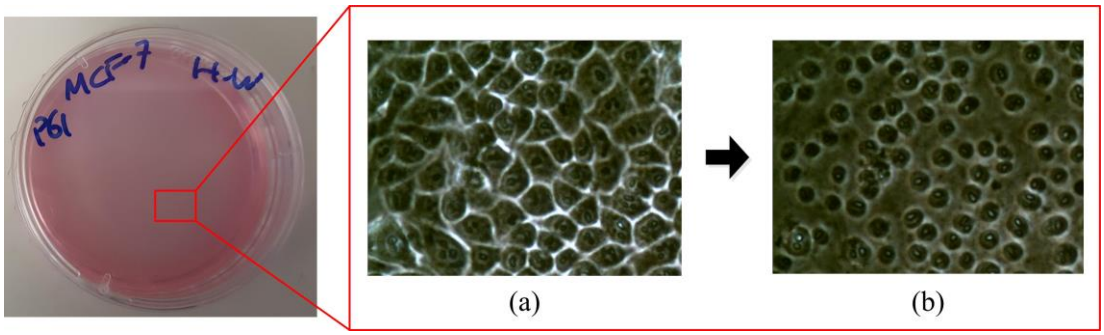

Figure 7-11 Cellular changes captured by the microscope. (a) Before applying Triton X-100. (b) 5 minutes after applying Triton X-100. (Image Provided by Mr. Hancong Wu)

In this subsection, the real-time, continuous, and non-destructive imaging of the interaction between MCF-7 human breast cancer cell spheroid and diluted Triton X-100 solution was carried out by using the developed EIT techniques in this thesis. In the experiment, Triton X-100 was utilised to lyse cells to permeabilize the membranes of MCF-7 cells. Consequently, the cancer cells would be killed (Koley and Bard, 2010). Figure 7-11 demonstrates the effect of Triton X-100 on MCF-7 cells. In order to examine cell status by the optical method, opaque cell solution, instead of cell spheroids, was adopted. Figure 7-11(a) and (b) illustrate the cellular changes, captured 5 minutes after applying Triton X-100, from using 10×20 magnifications with the Olympus CK2 Inverted Microscope. The membranolysis and shrinkage of MCF-7 cells is observed clearly in the figure. Theoretically, the physiological status change of cells, caused by Triton X-100 or other similar drugs,

can be indicated by conductivity variation indirectly (Bagnaninchi and Drummond, 2011). This suggests that EIT is a promising technique to visualise the process.

Figure 7-12 illustrates the setup of experiment. Figure 7-12(a) shows the MCF-7 cell spheroid in the sensor; the spheroid was placed near electrode 9 and 10. The diameter of the cell spheroid is around 3 mm. Figure 7-12(b) shows the miniature EIT sensor connected with the mfEIT system.

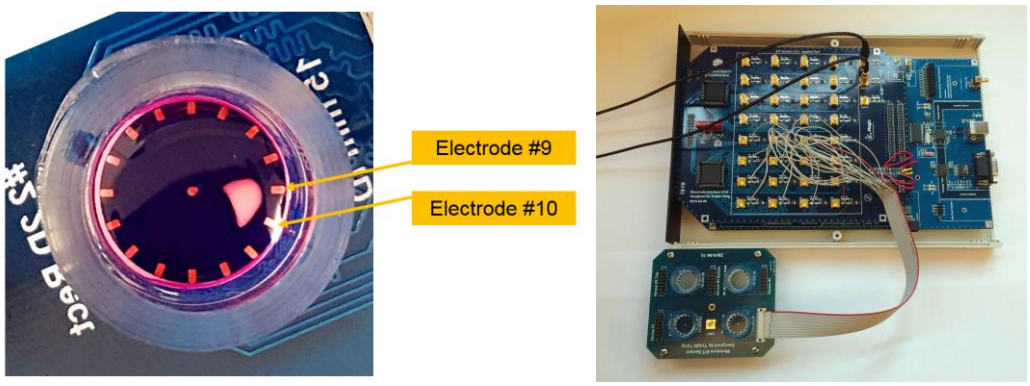

(a) (b)

Figure 7-12 Experiment setup. (a) The MCF-7 cell spheroid in the sensor. (b) The EIT system.

The schematic illustration of experiment procedure for cell-drug response imaging is presented in Figure 7-13. Firstly, the sensor was sterilised before the experiment began and, at time point t_0, 900 microliters of cell culture medium, i.e. PBS, were added to the sensor chamber. Then, the mfEIT system was started to take measurements. After PBS was measured for tens of seconds, 100 microliters of diluted Triton X-100 solution were delivered at time point t_1. As discussed in the last subsection, in order to avoid the influence from the drug diffusion process, the mixture of PBS and Triton X-100 was stirred quickly at time point t_2, in order to obtain a uniformly mixed solution before the cell spheroid was delivered. After a few minutes when the mixture was stable, a MCF-7 human breast cancer cell spheroid was delivered at time point t_3. By this way, the conductivity variation contributed by drug diffusion was separated from that by the drug effect. According to previous studies, Triton X-100 can kill the cells in a few minutes (Koley and Bard, 2010). Hence, the measurement process was terminated approximately 10 minutes later, when the reaction was completely over.

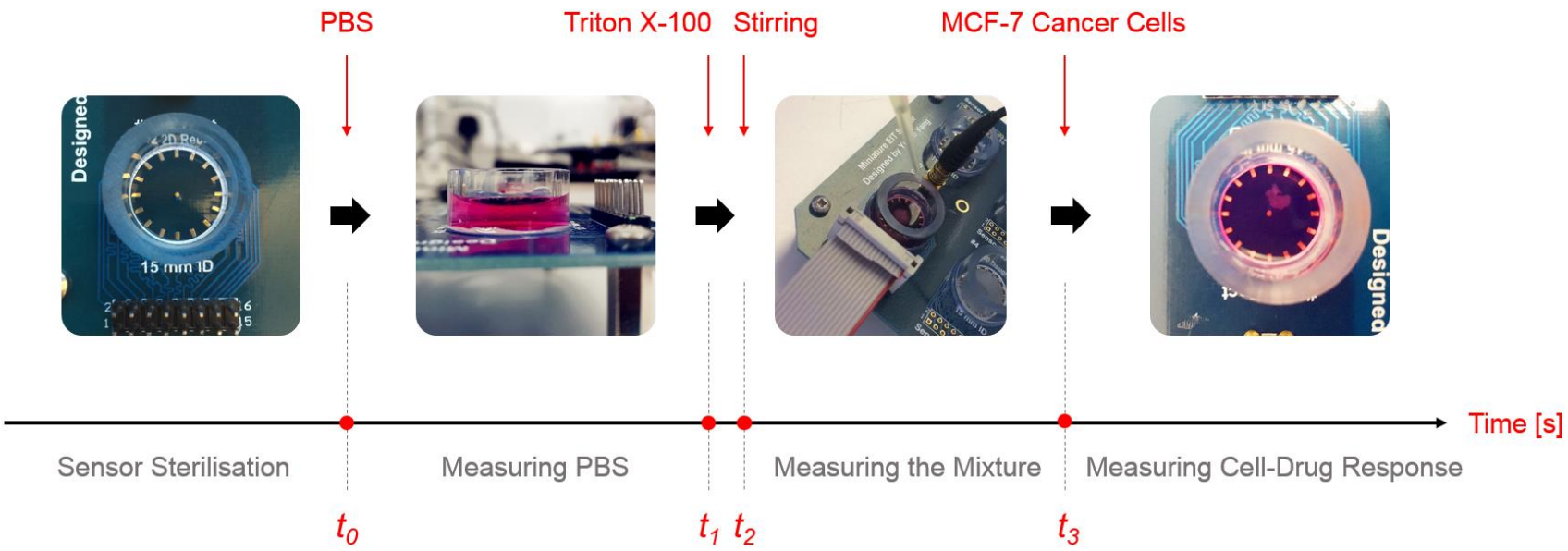

Figure 7-13 Schematic illustration of cell-drug response experiment procedure.

3D image reconstructions were conducted in time sequence, based on the 3D model developed in Chapter 6, in order to visualise the conductivity variation generated by the cell-drug response. With purpose of imaging the conductivity variation only associated with the drug effect, herein the measurement taken at 2 seconds after the cell addition, i.e. t_3+2 seconds, was employed as a reference point to perform TD imaging. To obtain high quality 3D tomographic images, the 3D image reconstruction algorithm developed in Chapter 6, namely 3D-Lap-l_1, was used. The algorithm parameters were the same with those utilised in Chapter 6. In addition to the 3D images, the time sequence of voltage response on the specific electrode pair, which was close to the position of the cell spheroid, was analysed as well.

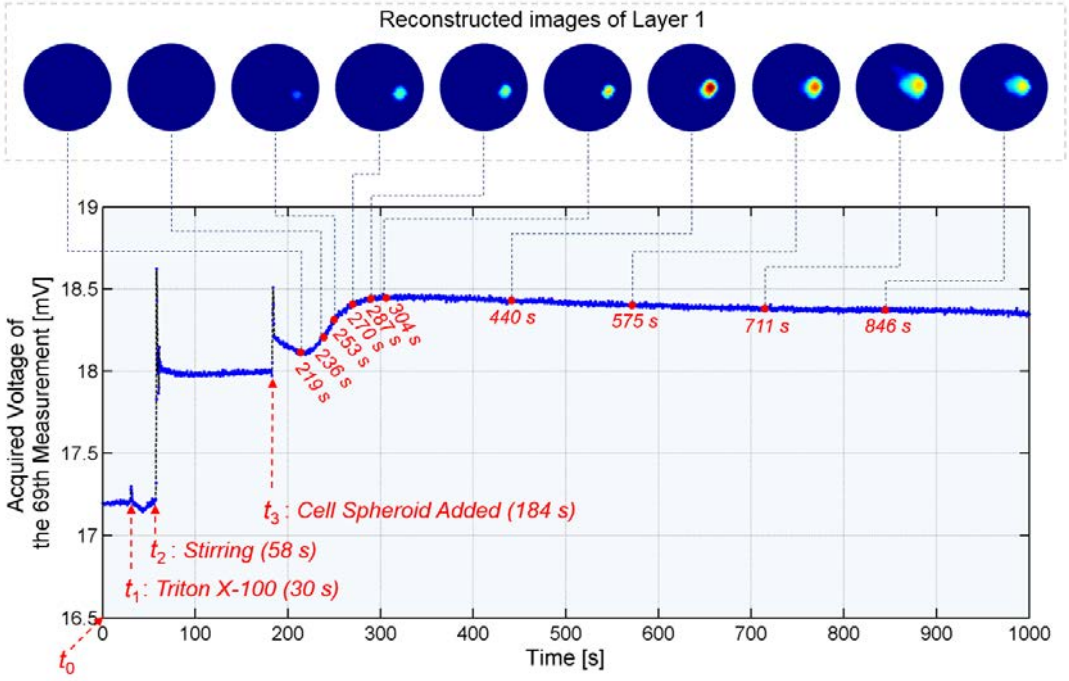

Figure 7-14 Voltage response of the 69th measurement out of 104 measurements (electrode 7, 8 act as current injection, 9, 10 act as measurement).

Figure 7-14 presents the time sequence of voltage response of the 69th measurement, in which the 7th and 8th electrodes acted as current injection while the 9th and 10th electrodes strobed as differential voltage measurements. Meanwhile, the reconstructed images of layer 1, i.e. the bottom layer, were given in chronological order. As Figure 7-14 suggests, the voltage change corresponding to each stage of the

experiment procedure can be observed explicitly, including the addition of Triton X-100 at time point t_1, the following stirring process at time point t_2, and the cell-drug response process after time point t_3. More particularly, evident voltage variation was acquired after the cell spheroid was added to the cell culture medium after time point t_3. This was associated directly with the cell-drug response process.

Figure 7-14 illustrates the 3D image reconstruction results over time in the format of sliced images by layer. It shows that, before 236 seconds, there is no apparent evidence of conductivity variation; this indicates that the cell-drug response is still inadequate. Nevertheless, from 253 seconds to 440 seconds, there appears a clear, continuous decline in conductivity within the area of the cell spheroid. This is because, after the cytomembrane is dissolved by Triton X-100, more and more cellular matrix, which is less conductive, enters the cell culture medium. However, from 440 seconds to 846 seconds, a reverse trend is observed, i.e. instead of declining, the amplitude of conductivity variation increases gradually. In the meantime, the area of conductivity variation becomes larger slowly during this period. The phenomena are due to the diffusion process of the less conductive cellular matrix over time. The results have been confirmed by numerous repeated experiments.

Time	Sliced Images
202 s	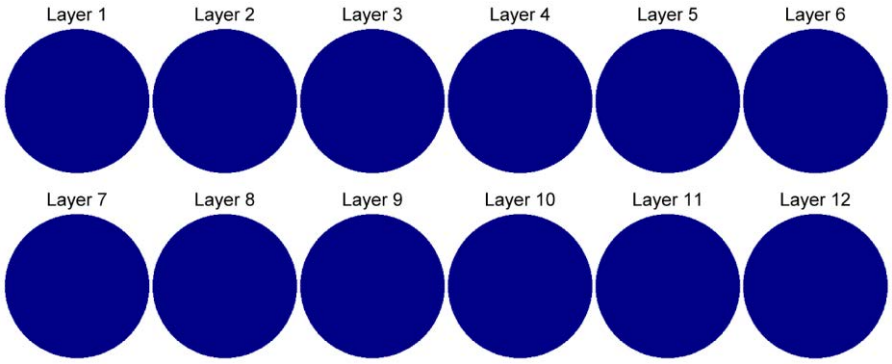

219 s	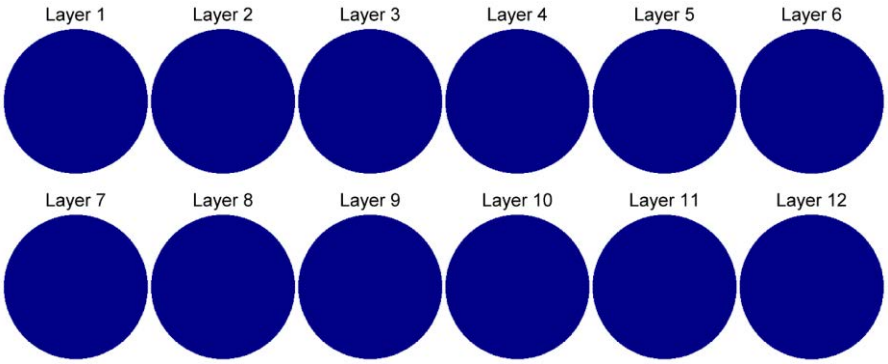
236 s	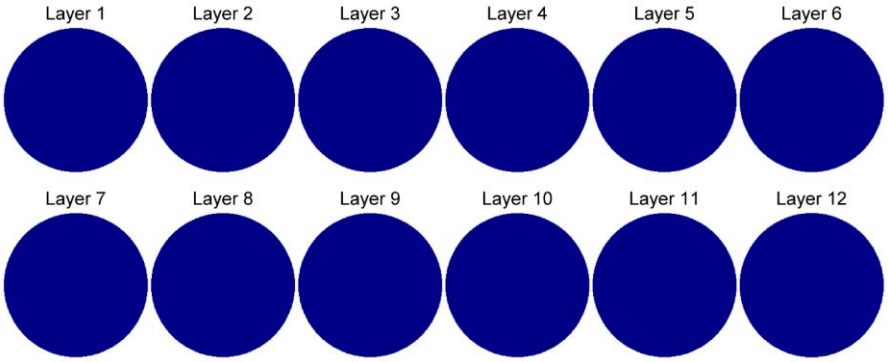
253 s	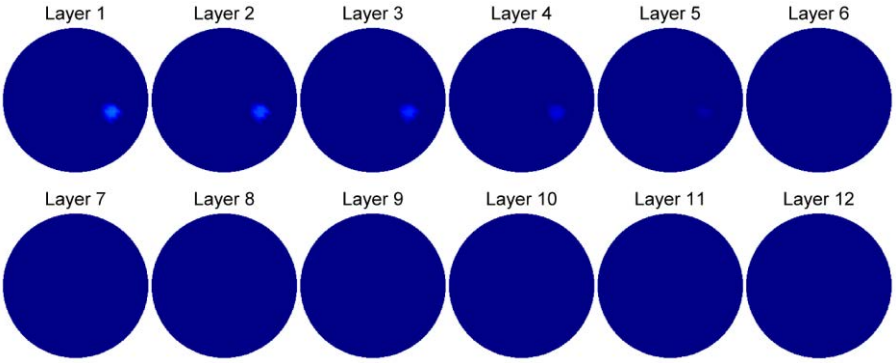
270 s	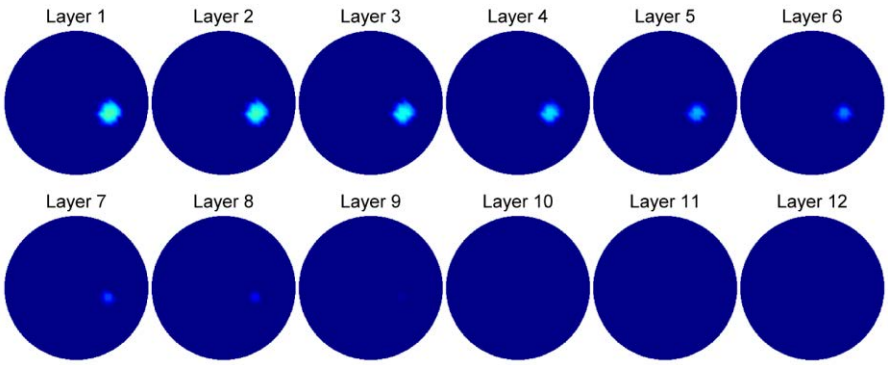

287 s	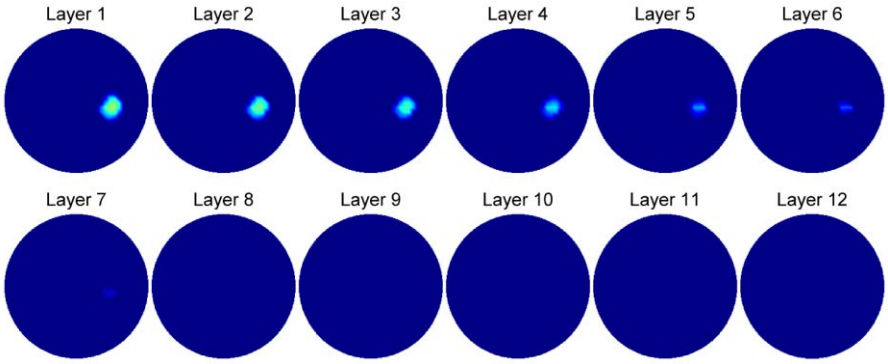
304 s	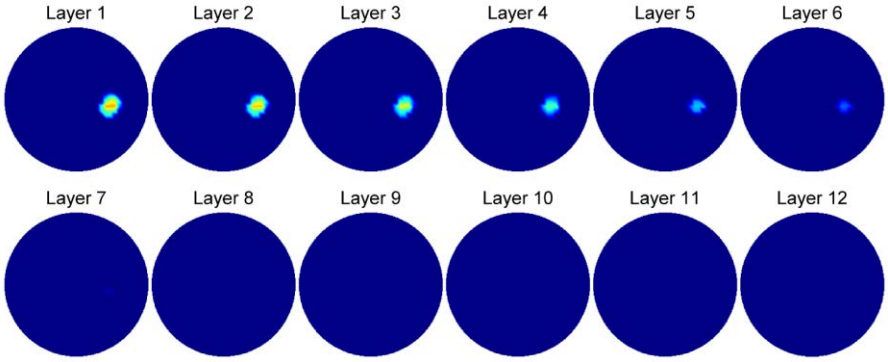
440 s	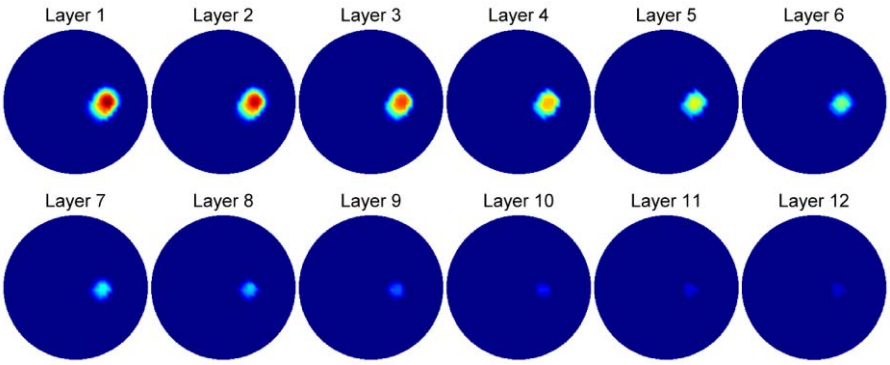
575 s	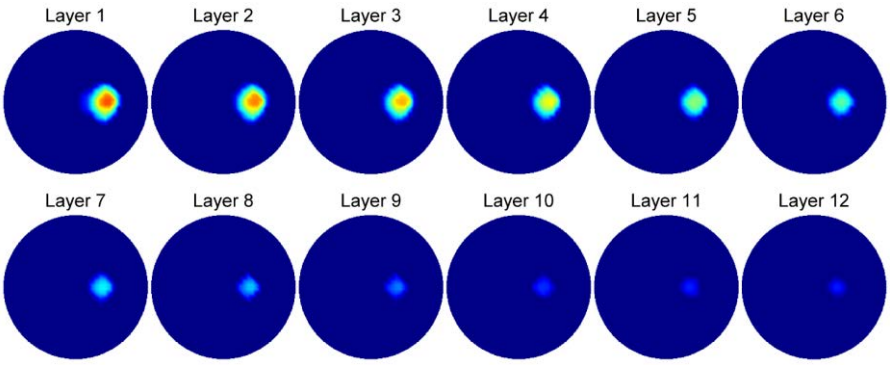

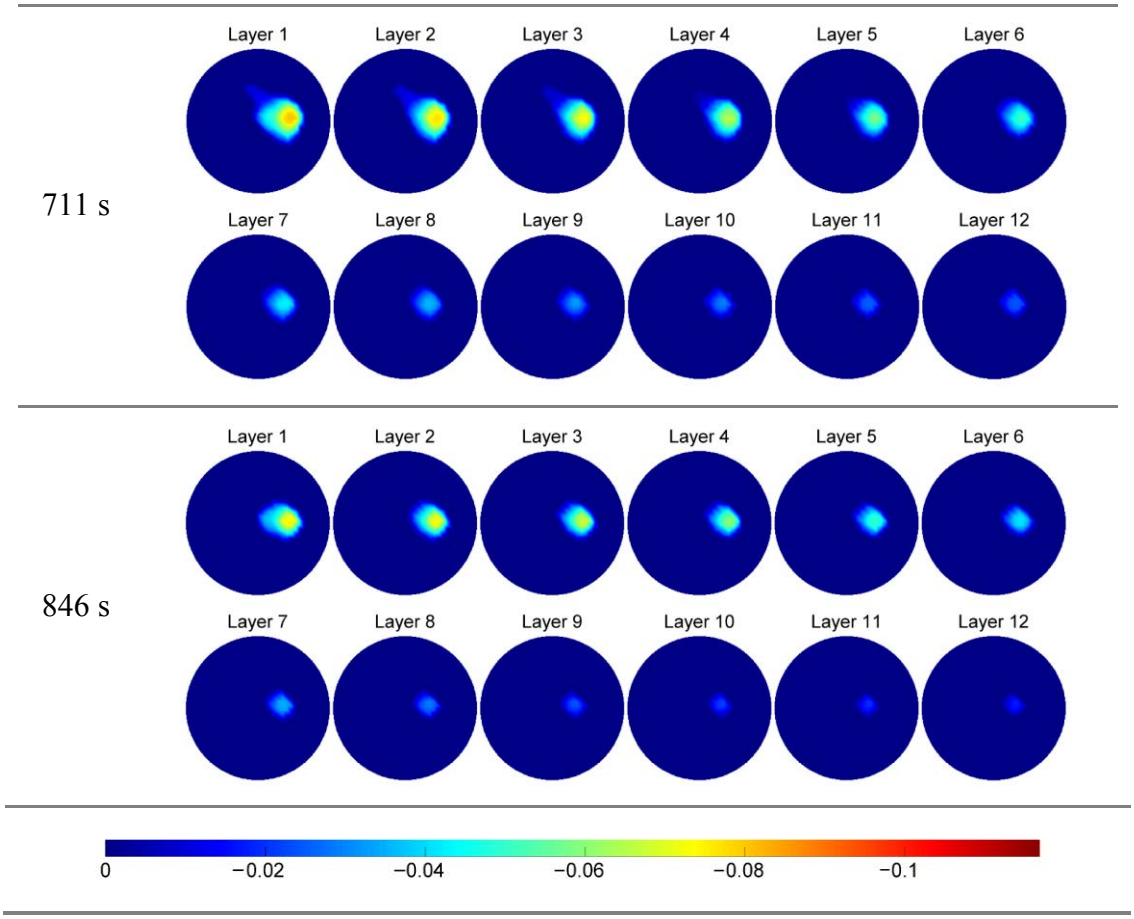

Figure 7-15 Cell-drug response imaging results by EIT.

The experiment study demonstrated that high quality 3D tomographic images of the cell-drug response process were obtained by using the miniature EIT sensor and the developed 3D image reconstruction algorithm in Chapter 6. By optimising the experiment procedure and selecting the reference point carefully, these images showed meaningful conductivity variations attributable to drug effect which could not be observed either visually or via optical methods such as a microscope.

7.5 Summary

This chapter investigated the practical applications of EIT in 3D cultured cell imaging and cell-drug response imaging on the basis of the developed mfEIT system, the proposed image reconstruction algorithms and the miniature EIT sensor in the former chapters. Promising and meaningful results were obtained from a series of cell imaging experiments. Major findings included: a) the developed mfEIT system

was verified to be stable enough for long-term monitoring on the highly conductive cell culture medium; b) the proposed AGS and EAGS-TV algorithms could perform high quality cell spheroid imaging on a 2D miniature sensor; and c) by using the developed mfEIT system and the miniature EIT sensor, conductivity variation associated with cell-drug response was observed successfully, for the first time to the best of my knowledge.

Chapter 8 Conclusions and Future Work

8.1 Conclusions

Whilst challenging, the implementation of EIT in biomedical applications is very promising. The key challenges come from several aspects such as biomedical instrumentation, spatial imaging resolution, biosensor and sensing strategy, experiment design, comparison validation and data interpretation. Proceeding from these perspectives, this thesis explored an emerging biomedical application of EIT in 3D cell culture imaging. A comprehensive study was carried out in terms of advanced biomedical EIT system development, high performance image reconstruction algorithm investigation, miniature biosensor design and 3D cell culture imaging experiments. The detailed work, contributed by this thesis, is summarised as follows.

The fundamental theory of EIT, the existing biomedical EIT systems, the cutting edge EIT image reconstruction algorithms and the emerging application of EIT in cellular imaging, were firstly reviewed. The review helped to understand in depth the recent advances of the EIT technique and the background of the innovated work demonstrated in this thesis.

The challenges in biomedical instrumentation side were then dealt with. A biomedical mfEIT system, targeted at real-time 2D and 3D impedance spectroscopic imaging, was developed and evaluated thoroughly in terms of load capacity, frame rate, SNR, 2D and 3D multi-frequency image reconstructions. The system design was presented from perspectives of system architecture and pivotal function modules. Compared with existing biomedical EIT systems, the presented mfEIT system's novel features included real-time 3D and 2D multi-frequency imaging ability, highly flexible sensing abilities, such as fully adjustable current source with real-time monitoring and emergency switch-off function, arbitrarily configurable electrode interfaces, fully software-controlled sensing parameters and image reconstruction algorithms, adjustable power supplies, etc., and high SNR and high frame rate. The system's working frequency ranged from 10 kHz to 1 MHz. The

evaluation results showed that the highest SNR of the system was 82.82 dB, and the frame rate was up to 546 fps in serial mode and 1014 fps in semi-parallel mode. The presented 3D imaging software, *Visual Tomography*, was able to support up to 120 fps time-stacked or true spatial 3D imaging in real time. In summary, the developed mfEIT system demonstrated excellent specifications, therefore could offer advanced spectral impedance imaging ability for biomedical imaging applications.

The thesis also made effort to tackle the bottleneck of low temporal resolution of EIT imaging. A high resolution image reconstruction algorithm utilising the adaptive group sparsity constraint was proposed. It was used to model the EIT image reconstruction problem with a weighted group-sparse basis pursuit model with nonnegativity constraint. It efficiently made use of the underlying group sparsity structure of conductivity as *a priori* knowledge for enhanced imaging performance. In order to facilitate fast group structure extraction, an adaptive pixel grouping method was incorporated for dynamic, self-adapting conductivity variation grouping. For validation purposes, numerical simulations and static phantom experiments on several challenging conductivity phantoms were carried out. The reconstruction results were compared thoroughly with conventional Landweber iteration, l_1 regularisation and TV regularisation methods. The contrast of results verified that the proposed AGS algorithm was able to generate superior tomographic images with higher image quality, better noise deduction performance and improved spatial resolution, in comparison with the other given algorithms.

Further, another novel image reconstruction algorithm named EAGS-TV was presented. This method employed simultaneously an enhanced adaptive group sparsity and TV constraints. Both the *a priori* knowledge of conductivity variation's regional structure features and global characteristics were considered by combining group sparsity and TV constraints. The regional structure feature was integrated by using an enhanced adaptive group sparsity constraint, and the globally presented piece-wise characteristic of conductivity variation was promoted by imposing TV constraint on the whole image. Based on Otsu's thresholding method, an enhanced adaptive pixel grouping method was proposed. In order to solve the problem with a faster convergence rate, an accelerated alternating direction method of multipliers

was applied. Numerical simulation and practical experiments validated EAGS-TV's performance where superior image quality was obtained in both cases. Compared with l_1 regularisation, TV regularisation and AGS, EAGS-TV was demonstrated to be a more effective algorithm for high resolution conductivity imaging.

Thereafter, this thesis continued with the systematic study of applying the developed mfEIT system to 3D cell culture imaging. A planar miniature EIT sensor, which was compatible with the cell culture dish, was designed, modelled, characterized and manufactured firstly. Then, a novel 3D-Laplacian and sparsity joint regularisation algorithm was proposed for high quality 3D imaging on the designed sensor. The simulation study confirmed that the planar miniature EIT sensor could measure the voltage changes induced by conductivity changes at both horizontal and vertical positions. Furthermore, the sensor and 3D image reconstruction algorithm were tested by using the mfEIT system developed in Chapter 3. A human breast cancer cell spheroid and a triangular cancer cell pellet were imaged, reconstructed and analysed. Both simulation and experiment results validated the improvement of image quality by using the proposed algorithm. This work verified the feasibility of applying the designed planar miniature EIT sensor together with the proposed 3D image reconstruction algorithm to generate stable, high quality images for 3D cellular substance imaging and monitoring. The high image quality obtained by the proposed method guaranteed reliable and accurate analysis of real-time cellular dynamics in the further study.

Finally, by using the developed system and methodologies from the former chapters, extensive experimental investigation and analysis of static cell spheroid imaging and real-time cell-drug response imaging were performed. Firstly, the developed mfEIT system was verified to be stable enough to perform long-term monitoring on the highly conductive cell culture medium, i.e. PBS with a conductivity of 2 $S \cdot m^{-1}$. Thereafter, the proposed AGS and EAGS-TV algorithms were proven to be effective in cell spheroid imaging on a 2D miniature EIT sensor. Furthermore, the drug diffusion process was captured and analysed successfully via real-time 3D imaging; this provided guidance on designing the optimal experiment procedure. Most importantly and for the first time, to the best of my knowledge, the

3D conductivity variation associated with cell-drug response was observed successfully in real time; this was achieved by using the developed mfEIT system, the designed miniature EIT sensor, and the proposed 3D image reconstruction algorithm.

In conclusion, the proof-of-concept work, demonstrated in this thesis, makes it possible to perform handily stable, high quality 2D/3D cellular substance imaging and long-term, high temporal resolution cellular dynamics monitoring, which cannot be achieved by other imaging modalities to date. The high image quality guarantees, also, reliable and accurate quantitative analysis of the cell-drug response process and other studies of cellular dynamics.

8.2 Future Work

Although this thesis made a step progress for 3D cell culture imaging with the developed EIT techniques, further investigation is still needed to promote this work from the following aspects:

a) With regard to the development of biomedical EIT systems, extension of bandwidth especially towards lower frequencies, e.g., below 1 kHz, is worthy of study; this is because the bioimpedance change, which is resulted from certain physiological activities, is more exquisite in lower frequency ranges.

b) As for image reconstruction, the presented AGS and EAGS-TV algorithm is only suitable currently for 2D image reconstruction due to the significantly increased complexity of adaptive pixel grouping for the 3D cases. In order to exert fully the predominance of these algorithms, the adaptive pixel grouping methods should be optimised and extended to the 3D cases. Furthermore, the practical application of these algorithms in real-time and long-term cell culture monitoring should be investigated as well. The extension of these algorithms for other tomographic modalities, for example, Electrical Capacitance

Tomography and Magnetic Induction Tomography, is also under consideration.

c) With respect to biosensor design, a future study should include the optimisation of sensor dimension and structure, sensor manufacture using advanced manufacture technique and integration of multi-modality biosensors for cross-validation and a more accurate sensing performance.

d) Finally, there is a need to perform extensive, repeated cross-validation 3D cell culture imaging experiments in order to evaluate the reliability and repeatability of the proposed methods. In addition, it is imperative to study multi-frequency cell culture imaging and long-term, real-time quantitative imaging of 3D cell culture systems for the assessment of cellular dynamics such as cell adhesion, proliferation, differentiation and cell-drug response.

References

ABU-ABSI, N. R., KENTY, B. M., CUELLAR, M. E., BORYS, M. C., SAKHAMURI, S., STRACHAN, D. J., HAUSLADEN, M. C. & LI, Z. J. 2011. Real Time Monitoring of Multiple Parameters in Mammalian Cell Culture Bioreactors Using an In-Line Raman Spectroscopy Probe. *Biotechnology and Bioengineering,* 108**,** 1215-1221.

ADLER, A., DAI, T. & LIONHEART, W. R. B. 2007. Temporal image reconstruction in electrical impedance tomography. *Physiological Measurement,* 28**,** S1-S11.

ADLER, A. & LIONHEART, W. R. B. 2006. Uses and abuses of EIDORS: an extensible software base for EIT. *Physiological Measurement,* 27**,** S25-S42.

ALBERTI, G. S., AMMARI, H., JIN, B. T., SEO, J. K. & ZHANG, W. L. 2016. The Linearized Inverse Problem in Multifrequency Electrical Impedance Tomography. *Siam Journal on Imaging Sciences,* 9**,** 1525-1551.

AMMARI, H., GARNIER, J., GIOVANGIGLI, L., JING, W. J. & SEO, J. K. 2016a. Spectroscopic imaging of a dilute cell suspension. *Journal De Mathematiques Pures Et Appliquees,* 105**,** 603-661.

AMMARI, H., GIOVANGIGLI, L., KWON, H., SEO, J. K. & WINTZ, T. 2016b. Spectroscopic conductivity imaging of a cell culture. *Asymptotic Analysis,* 100**,** 87-109.

AMMARI, H., WIDLAK, T. & ZHANG, W. 2017. Towards Monitoring Critical Microscopic Parameters for Electropermeabilization. *Quarterly of Applied Mathematics,* 75**,** 1-17.

ANSELMI, N., SALUCCI, M., OLIVERI, G. & MASSA, A. 2015. Wavelet-Based Compressive Imaging of Sparse Targets. *IEEE Transactions on Antennas and Propagation,* 63**,** 4889-4900.

ARISTOVICH, K. Y., PACKHAM, B. C., KOO, H., DOS SANTOS, G. S., MCEVOY, A. & HOLDER, D. S. 2016. Imaging fast electrical activity in the brain with electrical impedance tomography. *Neuroimage,* 124**,** 204-213.

BABAEIZADEH, S. & BROOKS, D. H. 2007. Electrical impedance tomography for piecewise constant domains using boundary element shape-based inverse solutions. *IEEE Transactions on Medical Imaging,* 26**,** 637-647.

BAGNANINCHI, P. O. & DRUMMOND, N. 2011. Real-time label-free monitoring of adipose-derived stem cell differentiation with electric cell-substrate impedance sensing. *Proceedings of the National Academy of Sciences of the United States of America,* 108**,** 6462-6467.

BAGSHAW, A. P., LISTON, A. D., BAYFORD, R. H., TIZZARD, A., GIBSON, A. P., TIDSWELL, A. T., SPARKES, M. K., DEHGHANI, H., BINNIE, C. D. & HOLDER, D. S. 2003. Electrical impedance tomography of human brain function using reconstruction algorithms based on the finite element method. *Neuroimage,* 20**,** 752-764.

BARANIUK, R. G. 2007. Compressive sensing. *IEEE Signal Processing Magazine,* 24**,** 118-+.

BARBER, D. C. & BROWN, B. H. 1984. Applied Potential Tomography. *Journal of Physics E-Scientific Instruments,* 17**,** 723-733.

BAYFORD, R. H. 2006. Bioimpedance tomography (Electrical impedance tomography). *Annual Review of Biomedical Engineering,* 8**,** 63-91.

BECK, A. & TEBOULLE, M. 2009. Fast Gradient-Based Algorithms for Constrained Total Variation Image Denoising and Deblurring Problems. *IEEE Transactions on Image Processing,* 18**,** 2419-2434.

BERA, T. K., NAGARAJU, J. & LUBINEAU, G. 2016. Electrical impedance spectroscopy (EIS)-based evaluation of biological tissue phantoms to study multifrequency electrical impedance tomography (Mf-EIT) systems. *Journal of Visualization,* 19**,** 691-713.

BERGER, C. R., WANG, Z. H., HUANG, J. Z. & ZHOU, S. L. 2010. Application of Compressive Sensing to Sparse Channel Estimation. *IEEE Communications Magazine,* 48**,** 164-174.

BERTERO, M. & BOCCACCI, P. 1998. *Introduction to inverse problems in imaging,* Bristol, Institute of Physics Pub.

BIOUCAS-DIAS, J. M. & FIGUEIREDO, M. A. T. 2007. A new TwIST: Two-step iterative shrinkage/thresholding algorithms for image restoration. *IEEE Transactions on Image Processing,* 16**,** 2992-3004.

BRESLIN, S. & O'DRISCOLL, L. 2013. Three-dimensional cell culture: the missing link in drug discovery. *Drug Discovery Today,* 18**,** 240-249.

BROWN, B., BARBER, D., LEATHARD, A., LU, L., WANG, W., SMALLWOOD, R. & WILSON, A. 1994. High frequency EIT data collection and parametric imaging. *Innovation et technologie en biologie et médecine,* 15**,** 1-8.

BROWN, B. & SEAGAR, A. 1987. The Sheffield data collection system. *Clinical Physics and Physiological Measurement,* 8**,** 91.

CANALI, C., HEISKANEN, A., MUHAMMAD, H. B., HOYUM, P., PETTERSEN, F. J., HEMMINGSEN, M., WOLFF, A., DUFVA, M., MARTINSEN, O. G. & EMNEUS, J. 2015. Bioimpedance monitoring of 3D cell culturing-Complementary electrode configurations for enhanced spatial sensitivity. *Biosensors & Bioelectronics,* 63**,** 72-79.

CANDES, E. & ROMBERG, J. 2007. Sparsity and incoherence in compressive sampling. *Inverse Problems,* 23**,** 969-985.

CANDES, E. J. & WAKIN, M. B. 2008. An introduction to compressive sampling. *IEEE Signal Processing Magazine,* 25**,** 21-30.

CAO, Z. & XU, L. J. 2011. Direct image reconstruction for electrical capacitance tomography by using the enclosure method. *Measurement Science and Technology,* 22.

CAO, Z., XU, L. J., FAN, W. R. & WANG, H. X. 2010. Electrical capacitance tomography with a non-circular sensor using the dbar method. *Measurement Science and Technology,* 21.

CAO, Z., XU, L. J., FANG, W. R. & WANG, H. X. 2011. 2D electrical capacitance tomography with sensors of non-circular cross sections using the factorization method. *Measurement Science and Technology,* 22.

CAO, Z., XU, L. J. & WANG, H. X. 2009. Image reconstruction technique of electrical capacitance tomography for low-contrast dielectrics using Calderon's method. *Measurement Science and Technology,* 20.

CARLETTI, C., MONTANTE, G., DE BLASIO, C. & PAGLIANTI, A. 2016. Liquid mixing dynamics in slurry stirred tanks based on electrical resistance tomography. *Chemical Engineering Science,* 152**,** 478-487.

CHENEY, M., ISAACSON, D., NEWELL, J. C., SIMSKE, S. & GOBLE, J. 1990. NOSER: An algorithm for solving the inverse conductivity problem. *International Journal of Imaging Systems and Technology,* 2**,** 66-75.

CHENG, K. S., ISAACSON, D., NEWELL, J. C. & GISSER, D. G. 1989. Electrode Models for Electric-Current Computed-Tomography. *IEEE Transactions on Biomedical Engineering,* 36**,** 918-924.

CUKIERMAN, E., PANKOV, R., STEVENS, D. R. & YAMADA, K. M. 2001. Taking cell-matrix adhesions to the third dimension. *Science,* 294**,** 1708-1712.

DAVIDSON, J., WRIGHT, P., AHSAN, S., ROBINSON, R., POMFRETT, C. & MCCANN, H. fEITER–a new EIT instrument for functional brain imaging. Journal of Physics: Conference Series, 2010. IOP Publishing, 012025.

DENG, W., YIN, W. & ZHANG, Y. 2013. Group sparse optimization by alternating direction method. *Wavelets and Sparsity Xv,* 8858.

DONOHO, D. L. 1995. De-Noising by Soft-Thresholding. *IEEE Transactions on Information Theory,* 41**,** 613-627.

ERTAS, M., YILDIRIM, I., KAMASAK, M. & AKAN, A. 2013. Digital breast tomosynthesis image reconstruction using 2D and 3D total variation minimization. *Biomedical Engineering Online,* 12.

FRERICHS, I. 2000. Electrical impedance tomography (EIT) in applications related to lung and ventilation: a review of experimental and clinical activities. *Physiological Measurement,* 21**,** R1-R21.

FRERICHS, I., HAHN, G., SCHRODER, T. & HELLIGE, G. 1998. Electrical impedance tomography in monitoring experimental lung injury. *Intensive Care Medicine,* 24**,** 829-836.

FUKUSHIMA, M. 1992. Application of the alternating direction method of multipliers to separable convex programming problems. *Computational Optimization and Applications,* 1**,** 93-111.

GEHRE, M., KLUTH, T., LIPPONEN, A., JIN, B., SEPPANEN, A., KAIPIO, J. P. & MAASS, P. 2012. Sparsity reconstruction in electrical impedance

tomography: An experimental evaluation. *Journal of Computational and Applied Mathematics,* 236**,** 2126-2136.

GOLDSTEIN, T., O'DONOGHUE, B., SETZER, S. & BARANIUK, R. 2014. Fast Alternating Direction Optimization Methods. *Siam Journal on Imaging Sciences,* 7**,** 1588-1623.

GONZALEZ, G., HUTTUNEN, J. M. J., KOLEHMAINEN, V., SEPPANEN, A. & VAUHKONEN, M. 2016. Experimental evaluation of 3D electrical impedance tomography with total variation prior. *Inverse Problems in Science and Engineering,* 24**,** 1411-1431.

GONZALEZ, G., KOLEHMAINEN, V. & SEPPANEN, A. 2017. Isotropic and anisotropic total variation regularization in electrical impedance tomography. *Computers & Mathematics with Applications,* 74**,** 564-576.

GRASMAIR, M., HALTMEIER, M. & SCHERZER, O. 2008. Sparse regularization with l(q) penalty term. *Inverse Problems,* 24.

GUEZ, J. S., CASSAR, J. P., WARTELLE, F., DHULSTER, P. & SUHR, H. 2004. Real time in situ microscopy for animal cell-concentration monitoring during high density culture in bioreactor. *Journal of Biotechnology,* 111**,** 335-343.

HALLAJI, M., SEPPANEN, A. & POUR-GHAZ, M. 2014. Electrical impedance tomography-based sensing skin for quantitative imaging of damage in concrete. *Smart Materials and Structures,* 23.

HALTER, R. J., HARTOV, A. & PAULSEN, K. D. 2008. A broadband high-frequency electrical impedance tomography system for breast Imaging. *IEEE Transactions on Biomedical Engineering,* 55**,** 650-659.

HAMILTON, S. J. & MUELLER, J. L. 2013. Direct EIT Reconstructions of Complex Admittivities on a Chest-Shaped Domain in 2-D. *IEEE Transactions on Medical Imaging,* 32**,** 757-769.

HAO, L. L. & XU, L. S. 2016. Joint L-1 and Total Variation Regularization for Magnetic Detection Electrical Impedance Tomography. *Applied Computational Electromagnetics Society Journal,* 31**,** 677-683.

HEIKKINEN, L. M., KOURUNEN, J., SAVOLAINEN, T., VAUHKONEN, P. J., KAIPIO, J. P. & VAUHKONEN, M. 2006. Real time three-dimensional electrical impedance tomography applied in multiphase flow imaging. *Measurement Science and Technology,* 17**,** 2083-2087.

HEINRICH, S., SCHIFFMANN, H., FRERICHS, A., KLOCKGETHER-RADKE, A. & FRERICHS, I. 2006. Body and head position effects on regional lung ventilation in infants: an electrical impedance tomography study. *Intensive Care Medicine,* 32**,** 1392-1398.

HICKMAN, I. 1992. Direct Digital Synthesis. *Electronics World & Wireless World***,** 630-634.

HIRAGA, T., NEBUYA, S. & UJIHIRA, M. 2013. Basic study on visualization of a cell during freezing using electrical impedance tomography. *生体医工学,* 51**,** R-253-R-253.

HOLMES, C., DAOUD, J., BAGNANINCHI, P. O. & TABRIZIAN, M. 2014. Polyelectrolyte Multilayer Coating of 3D Scaffolds Enhances Tissue Growth and Gene Delivery: Non-Invasive and Label-Free Assessment. *Advanced Healthcare Materials,* 3**,** 572-580.

HU, X. H. & YANG, W. Q. 2010. Planar capacitive sensors - designs and applications. *Sensor Review,* 30**,** 24-39.

HUANG, J. Z. & ZHANG, T. 2010. The Benefit of Group Sparsity. *Annals of Statistics,* 38**,** 1978-2004.

JAMIESON, L. E. & BYRNE, H. J. 2017. Vibrational spectroscopy as a tool for studying drug-cell interaction: Could high throughput vibrational spectroscopic screening improve drug development? *Vibrational Spectroscopy,* 91**,** 16-30.

JIN, B., KHAN, T. & MAASS, P. 2012. A reconstruction algorithm for electrical impedance tomography based on sparsity regularization. *International Journal for Numerical Methods in Engineering,* 89**,** 337-353.

K'OWINO, I. O. & SADIK, O. A. 2005. Impedance spectroscopy: A powerful tool for rapid biomolecular screening and cell culture monitoring. *Electroanalysis,* 17**,** 2101-2113.

KAIPIO, J. & SOMERSALO, E. 2006. *Statistical and computational inverse problems*, Springer Science & Business Media.

KAIPIO, J. P., KOLEHMAINEN, V., SOMERSALO, E. & VAUHKONEN, M. 2000. Statistical inversion and Monte Carlo sampling methods in electrical impedance tomography. *Inverse Problems,* 16**,** 1487-1522.

KIM, B. S., KIM, K. Y. & KIM, S. 2014. Image reconstruction using adaptive mesh refinement based on adaptive thresholding in electrical impedance tomography. *Nuclear Engineering and Design,* 270**,** 421-426.

KIM, K. Y., KIM, B. S., KIM, M. C., KIM, S., LEE, Y. J., JEON, H. J., CHOI, B. Y. & VAUHKONEN, M. 2004. Electrical impedance imaging of two-phase fields with an adaptive mesh grouping scheme. *IEEE Transactions on Magnetics,* 40**,** 1124-1127.

KOLEY, D. & BARD, A. J. 2010. Triton X-100 concentration effects on membrane permeability of a single HeLa cell by scanning electrochemical microscopy (SECM). *Proceedings of the National Academy of Sciences of the United States of America,* 107**,** 16783-16787.

LALONDE, W. & PUGH, J. 1995. Rendering 3-D Graphics in Opengl. *Journal of Object-Oriented Programming,* 8**,** 63-&.

LEE, B. A., KIM, B. S., KO, M. S., KIM, K. Y. & KIM, S. 2014. Electrical Resistance Imaging of Two-Phase Flow with a Mesh Grouping Technique Based on Particle Swarm Optimization. *Nuclear Engineering and Technology,* 46**,** 109-116.

LI, H. X., SHEN, C. H. & SHI, Q. F. 2011. Real-time Visual Tracking Using Compressive Sensing. *2011 IEEE Conference on Computer Vision and Pattern Recognition (Cvpr)*, 1305-1312.

LIONHEART, W. R. B. 2004. EIT reconstruction algorithms: pitfalls, challenges and recent developments. *Physiological Measurement,* 25, 125-142.

LIU, J. Z., LIN, L., ZHANG, W. B. & LI, G. 2013. A novel combined regularization algorithm of total variation and Tikhonov regularization for open electrical impedance tomography. *Physiological Measurement,* 34, 823-838.

LUEPSCHEN, H., MEIER, T., GROSSHERR, M., LEIBECKE, T., KARSTEN, J. & LEONHARDT, S. 2007. Protective ventilation using electrical impedance tomography. *Physiological Measurement,* 28, S247-S260.

MALONE, E., DOS SANTOS, G. S., HOLDER, D. & ARRIDGE, S. 2014. Multifrequency Electrical Impedance Tomography Using Spectral Constraints. *IEEE Transactions on Medical Imaging,* 33, 340-350.

MALONE, E., DOS SANTOS, G. S., HOLDER, D. & ARRIDGE, S. 2015. A Reconstruction-Classification Method for Multifrequency Electrical Impedance Tomography. *IEEE Transactions on Medical Imaging,* 34, 1486-1497.

MARTIN, S. & CHOI, C. T. M. 2016. Nonlinear Electrical Impedance Tomography Reconstruction Using Artificial Neural Networks and Particle Swarm Optimization. *IEEE Transactions on Magnetics,* 52.

MCEWAN, A., ROMSAUEROVA, A., YERWORTH, R., HORESH, L., BAYFORD, R. & HOLDER, D. 2006. Design and calibration of a compact multi-frequency EIT system for acute stroke imaging. *Physiological Measurement,* 27, S199-S210.

MEIR, A. & RUBINSKY, B. 2014. Electrical impedance tomographic imaging of a single cell electroporation. *Biomedical Microdevices,* 16, 427-437.

METHERALL, P., BARBER, D. C., SMALLWOOD, R. H. & BROWN, B. H. 1996. Three-dimensional electrical impedance tomography. *Nature,* 380, 509-512.

MOSEGAARD, K. & RYGAARD-HJALSTED, C. 1999. Probabilistic analysis of implicit inverse problems. *Inverse Problems,* 15, 573-583.

MOURAS, R., BAGNANINCHI, P., DOWNES, A. & ELFICK, A. 2013. Multimodal, label-free nonlinear optical imaging for applications in biology and biomedical science. *Journal of Raman Spectroscopy,* 44, 1373-1378.

MUELLER, J. L., SILTANEN, S. & ISAACSON, D. 2002. A direct reconstruction algorithm for electrical impedance tomography. *IEEE Transactions on Medical Imaging,* 21, 555-559.

MURPHY, E. K., MAHARA, A. & HALTER, R. J. 2017. Absolute Reconstructions Using Rotational Electrical Impedance Tomography for Breast Cancer Imaging. *IEEE Transactions on Medical Imaging,* 36, 892-903.

NACHMAN, A. I. 1996. Global uniqueness for a two-dimensional inverse boundary value problem. *Annals of Mathematics,* 143**,** 71-96.

OH, T. I., WI, H., KIM, D. Y., YOO, P. J. & WOO, E. J. 2011. A fully parallel multi-frequency EIT system with flexible electrode configuration: KHU Mark2. *Physiological Measurement,* 32.

OH, T. I., WOO, E. J. & HOLDER, D. 2007. Multi-frequency EIT system with radially symmetric architecture: KHU Mark1. *Physiological Measurement,* 28**,** S183-S196.

OSHER, S., BURGER, M., GOLDFARB, D., XU, J. J. & YIN, W. T. 2005. An iterative regularization method for total variation-based image restoration. *Multiscale Modeling & Simulation,* 4**,** 460-489.

OTSU, N. 1979. A threshold selection method from gray-level histograms. *IEEE transactions on systems, man, and cybernetics,* 9**,** 62-66.

PENG, L. H., MERKUS, H. & SCARLETT, B. 2000. Using regularization methods for image reconstruction of electrical capacitance tomography. *Particle & Particle Systems Characterization,* 17**,** 96-104.

PETERSON, W. D., SIMPSON, W. F. & HUKKU, B. 1979. Cell culture characterization: Monitoring for cell identification. *Methods in enzymology,* 58**,** 164-178.

POLYDORIDES, N. & LIONHEART, W. R. B. 2002. A Matlab toolkit for three-dimensional electrical impedance tomography: a contribution to the Electrical Impedance and Diffuse Optical Reconstruction Software project. *Measurement Science and Technology,* 13**,** 1871-1883.

RAFIEI-NAEINI, M. & MCCANN, H. 2008. Low-noise current excitation sub-system for medical EIT. *Physiological Measurement,* 29**,** S173-S184.

RAHMAN, A. R. A., REGISTER, J., VUPPALA, G. & BHANSALI, S. 2008. Cell culture monitoring by impedance mapping using a multielectrode scanning impedance spectroscopy system (CellMap). *Physiological Measurement,* 29**,** S227-S239.

RAVI, M., PARAMESH, V., KAVIYA, S. R., ANURADHA, E. & SOLOMON, F. D. P. 2015. 3D Cell Culture Systems: Advantages and Applications. *Journal of Cellular Physiology,* 230**,** 16-26.

REN, S. J., DONG, F., XU, Y. Y. & TAN, C. 2014. Reconstruction of the three-dimensional inclusion shapes using electrical capacitance tomography. *Measurement Science and Technology,* 25.

SAULNIER, G. J., LIU, N., TAMMA, C., XIA, H. J., KAO, T. J., NEWELL, J. C. & ISAACSON, D. 2007. An electrical impedance spectroscopy system for breast cancer detection. *2007 Annual International Conference of the IEEE Engineering in Medicine and Biology Society, Vols 1-16***,** 4154-4157.

SHA, C. S., HOU, J. & CUI, H. X. 2016. A robust 2D Otsu's thresholding method in image segmentation. *Journal of Visual Communication and Image Representation,* 41**,** 339-351.

SIDEBOTTOM, C., RUDOLPH, H., SCHMIDT, M. & EISNER, L. 2006. IEC 60601-1–the third edition. *Journal of Medical Device Regulation-May*, 9.

SILVERA-TAWIL, D., RYE, D., SOLEIMANI, M. & VELONAKI, M. 2015. Electrical Impedance Tomography for Artificial Sensitive Robotic Skin: A Review. *IEEE Sensors Journal,* 15, 2001-2016.

SOMERSALO, E., CHENEY, M. & ISAACSON, D. 1992. Existence and Uniqueness for Electrode Models for Electric-Current Computed-Tomography. *Siam Journal on Applied Mathematics,* 52, 1023-1040.

STUART, A. M. 2010. Inverse problems: A Bayesian perspective. *Acta Numerica 2010, Vol 19,* 19, 451-559.

SUN, T., TSUDA, S., ZAUNER, K. P. & MORGAN, H. 2010. On-chip electrical impedance tomography for imaging biological cells. *Biosensors & Bioelectronics,* 25, 1109-1115.

TOSSAVAINEN, O. P., VAUHKONEN, M. & KOLEHMAINEN, V. 2007. A three-dimensional shape estimation approach for tracking of phase interfaces in sedimentation processes using electrical impedance tomography. *Measurement Science and Technology,* 18, 1413-1424.

VAN DEN BERG, E. & FRIEDLANDER, M. P. 2008. Probing the Pareto Frontier for Basis Pursuit Solutions. *Siam Journal on Scientific Computing,* 31, 890-912.

VAUHKONEN, M., LIONHEART, W. R. B., HEIKKINEN, L. M., VAUHKONEN, P. J. & KAIPIO, J. P. 2001. A MATLAB package for the EIDORS project to reconstruct two-dimensional EIT images. *Physiological Measurement,* 22, 107-111.

VAUHKONEN, M., VADASZ, D., KARJALAINEN, P. A., SOMERSALO, E. & KAIPIO, J. P. 1998. Tikhonov regularization and prior information in electrical impedance tomography. *IEEE Transactions on Medical Imaging,* 17, 285-293.

VAUHKONEN, P. J., VAUHKONEN, M., SAVOLAINEN, T. & KAIPIO, J. P. 1999. Three-dimensional electrical impedance tomography based on the complete electrode model. *IEEE Transactions on Biomedical Engineering,* 46, 1150-1160.

VINCI, M., GOWAN, S., BOXALL, F., PATTERSON, L., ZIMMERMANN, M., COURT, W., LOMAS, C., MENDIOLA, M., HARDISSON, D. & ECCLES, S. A. 2012. Advances in establishment and analysis of three-dimensional tumor spheroid-based functional assays for target validation and drug evaluation. *Bmc Biology,* 10.

VOGT, B., PULLETZ, S., ELKE, G., ZHAO, Z. Q., ZABEL, P., WEILER, N. & FRERICHS, I. 2012. Spatial and temporal heterogeneity of regional lung ventilation determined by electrical impedance tomography during pulmonary function testing. *Journal of Applied Physiology,* 113, 1154-1161.

WANG, H. X., TANG, L. & CAO, Z. 2007. An image reconstruction algorithm based on total variation with adaptive mesh refinement for ECT. *Flow Measurement and Instrumentation,* 18**,** 262-267.

WANG, H. X., WANG, C. & YIN, W. L. 2004. A pre-iteration method for the inverse problem in electrical impedance tomography. *IEEE Transactions on Instrumentation and Measurement,* 53**,** 1093-1096.

WANG, M., MA, Y. X., HOLLIDAY, N., DAI, Y. F., WILLIAMS, R. A. & LUCAS, G. 2005. A high-performance EIT system. *IEEE Sensors Journal,* 5**,** 289-299.

WANG, Q., POLANSKY, J., KARKI, B., WANG, M., WEI, K., QIU, C. H., KENBAR, A. & MILLINGTON, D. 2016. Experimental tomographic methods for analysing flow dynamics of gas-oil-water flows in horizontal pipeline. *Journal of Hydrodynamics,* 28**,** 1018-1021.

WANG, Q., SUN, K. J., WANG, J. M., ZHANG, R. H. & WANG, H. X. 2015. Reconstruction of EIT Images via Patch based Sparse Representation over Learned Dictionaries. *2015 IEEE International Instrumentation and Measurement Technology Conference (I2mtc)***,** 2044-2048.

WATZENIG, D. & FOX, C. 2009. A review of statistical modelling and inference for electrical capacitance tomography. *Measurement Science and Technology,* 20.

WI, H., SOHAL, H., MCEWAN, A. L., WOO, E. J. & OH, T. I. 2014. Multi-Frequency Electrical Impedance Tomography System With Automatic Self-Calibration for Long-Term Monitoring. *IEEE Transactions on Biomedical Circuits and Systems,* 8**,** 119-128.

WILSON, A. J., MILNES, P., WATERWORTH, A. R., SMALLWOOD, R. H. & BROWN, B. H. 2001. Mk3.5: a modular, multi-frequency successor to the Mk3a EIS/EIT system. *Physiological Measurement,* 22**,** 49-54.

YANG, W. Q. & PENG, L. H. 2003. Image reconstruction algorithms for electrical capacitance tomography. *Measurement Science and Technology,* 14**,** R1-R13.

YANG, W. Q., SPINK, D. M., YORK, T. A. & MCCANN, H. 1999. An image-reconstruction algorithm based on Landweber's iteration method for electrical-capacitance tomography. *Measurement Science and Technology,* 10**,** 1065-1069.

YANG, Y., JIA, J., POLYDORIDES, N. & MCCANN, H. Effect of structured packing on EIT image reconstruction. Imaging Systems and Techniques (IST), 2014 IEEE International Conference on, 2014. IEEE, 53-58.

YANG, Y. J., JIA, J. B., SMITH, S., JAMIL, N., GAMAL, W. & BAGNANINCHI, P. O. 2017a. A Miniature Electrical Impedance Tomography Sensor and 3-D Image Reconstruction for Cell Imaging. *IEEE Sensors Journal,* 17**,** 514-523.

YANG, Y. J. & PENG, L. H. 2013. Data Pattern With ECT Sensor and Its Impact on Image Reconstruction. *IEEE Sensors Journal,* 13**,** 1582-1593.

YANG, Y. J., PENG, L. H. & JIA, J. B. 2017b. A novel multi-electrode sensing strategy for electrical capacitance tomography with ultra-low dynamic range. *Flow Measurement and Instrumentation,* 53**,** 67-79.

YAO, J., OBARA, H., SAPKOTA, A. & TAKEI, M. 2016. Development of three-dimensional integrated microchannel-electrode system to understand the particles' movement with electrokinetics. *Biomicrofluidics,* 10.

YE, J. M., WANG, H. G. & YANG, W. Q. 2015. Image Reconstruction for Electrical Capacitance Tomography Based on Sparse Representation. *IEEE Transactions on Instrumentation and Measurement,* 64**,** 89-102.

YERWORTH, R. J., BAYFORD, R. H., BROWN, B., MILNES, P., CONWAY, M. & HOLDER, D. S. 2003. Electrical impedance tomography spectroscopy (EITS) for human head imaging. *Physiological Measurement,* 24**,** 477-489.

YERWORTH, R. J., BAYFORD, R. H., CUSICK, G., CONWAY, M. & HOLDER, D. S. 2002. Design and performance of the UCLH Mark 1b 64 channel electrical impedance tomography (EIT) system, optimized for imaging brain function. *Physiological Measurement,* 23**,** 149-158.

YIN, M., LUO, Q. M. & XIA, F. H. 2001. 3-D visualization of biomedical CT images based on OpenGL and VRML techniques. *International Workshop on Photonics and Imaging in Biology and Medicine,* 4536**,** 225-233.

YUE, X. C. & MCLEOD, C. 2008. FPGA design and implementation for EIT data acquisition. *Physiological Measurement,* 29**,** 1233-1246.

ZHAO, L., FU, H. Y., ZHOU, W. C. & HU, W. S. 2015. Advances in process monitoring tools for cell culture bioprocesses. *Engineering in Life Sciences,* 15**,** 459-468.

ZHENG, X. T., YU, L., LI, P. W., DONG, H., WANG, Y. J., LIU, Y. & LI, C. M. 2013. On-chip investigation of cell-drug interactions. *Advanced Drug Delivery Reviews,* 65**,** 1556-1574.

ZHOU, Z., DOS SANTOS, G. S., DOWRICK, T., AVERY, J., SUN, Z. L., XU, H. & HOLDER, D. S. 2015. Comparison of total variation algorithms for electrical impedance tomography. *Physiological Measurement,* 36**,** 1193-1209.

ZHU, Q. S., MCLEOD, C. N., DENYER, C. W., LIDGEY, F. J. & LIONHEART, W. R. B. 1994. Development of a Real-Time Adaptive Current Tomograph. *Physiological Measurement,* 15**,** A37-A43.